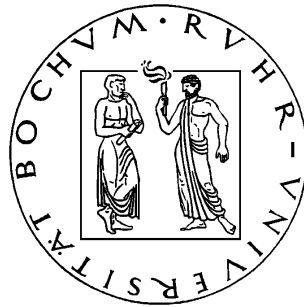


Search for Tidal Streams in Disk and Halo



Dissertation

zur

Erlangung des Grades

„Doktor der Naturwissenschaften“

in der Fakultät für Physik und Astronomie

der Ruhr – Universität Bochum

von

Olaf Schmithüsen

aus

Oberhausen

Bochum 2008

1. Gutachter: Prof. Dr. Ralf-Jürgen Dettmar
 2. Gutachter: Priv. Doz. Dr. Dominik J. Bomans
- Datum der Disputation: 19.12.2008

Contents

| | | |
|----------|---|-----------|
| 1 | Introduction | 1 |
| 2 | General Physics of Galaxy Formation | 5 |
| 2.1 | Observational Evidence for DM | 5 |
| 2.2 | Basic Cosmology | 6 |
| 2.3 | The Λ -CDM Model and the Substructure | 6 |
| 2.4 | The Missing Satellite Problem | 10 |
| 2.5 | Galaxy Evolution | 12 |
| 2.6 | The Galaxies | 14 |
| 2.6.1 | NGC 300 | 14 |
| 2.6.2 | M 83 | 15 |
| 2.6.3 | M 33 | 15 |
| 2.6.4 | NGC 7793 | 16 |
| 3 | Data Reduction | 19 |
| 3.1 | General Discussion | 19 |
| 3.2 | Overview of the Datasets | 19 |
| 3.2.1 | Telescope & Detector | 19 |
| 3.2.2 | NGC 300 Data | 20 |
| 3.2.3 | M 83 Data | 21 |
| 3.2.4 | NGC 7793 | 21 |
| 3.2.5 | M 33 | 22 |
| 3.3 | The <i>THELI</i> -Pipeline | 23 |
| 3.4 | Data Reduction in Detail | 24 |
| 3.4.1 | PRE-Reduction | 25 |
| 3.4.2 | RUN-Based-Reduction | 26 |
| 3.4.3 | Fringing in the I-Band | 26 |
| 3.4.4 | SET-Based-Reduction | 28 |

| | | |
|----------|--|------------|
| 3.4.5 | The Sky-Background Procedure | 29 |
| 4 | Photometry & Calibration | 35 |
| 4.1 | General Discussion | 35 |
| 4.2 | General Photometry Procedure and Issues | 35 |
| 4.3 | The Wide-Field-Imager Illumination Problem | 37 |
| 4.4 | Photometry and Calibration of NGC 300 Data | 41 |
| 4.5 | Photometry and Calibration of M 83 Data | 44 |
| 4.6 | Photometry and Calibration of NGC 7793 Data | 45 |
| 5 | Methods of Data Analysis | 49 |
| 5.1 | General Discussion | 49 |
| 5.2 | Color-Magnitude-Diagram | 49 |
| 5.3 | Methods | 52 |
| 5.3.1 | Preselection Using Isochrones | 52 |
| 5.3.2 | Data-Mining | 55 |
| 6 | Data Analysis | 69 |
| 6.1 | General Discussion | 69 |
| 6.2 | Analysis of The NGC 300 Data | 69 |
| 6.2.1 | The Star Count Maps | 70 |
| 6.2.2 | Data Mining Results Using a Fuzzy C-Means Clustering | 78 |
| 6.2.3 | Comparison to Other Studies | 82 |
| 6.3 | Analysis of M 83 Data | 84 |
| 6.3.1 | CMDs & Star Count Maps | 84 |
| 6.3.2 | Data Mining Results Using a Fuzzy C-Means Clustering | 88 |
| 6.3.3 | Comparison of Other Studies | 89 |
| 6.4 | Analysis of M 33 Data | 90 |
| 6.4.1 | CMDs & Star Count Maps | 90 |
| 6.4.2 | Data Mining Results Using a Fuzzy C-Means Clustering | 91 |
| 6.4.3 | Comparison to Other Studies | 93 |
| 6.5 | Analysis of NGC 7793 Data | 104 |
| 6.5.1 | CMDs & Star Count Maps | 104 |
| 6.5.2 | Data Mining Results Using a Fuzzy C-Means Clustering | 106 |
| 6.5.3 | Comparison to Other Studies | 107 |
| 7 | Results & Summary | 115 |
| 7.1 | Technical Results | 115 |
| 7.2 | Scientific Results | 118 |
| 7.3 | Final Result and Outlook | 121 |

| | |
|--|----------------|
| A List of Images Used for Co-added Frames | 125 |
| A.1 M 83 V-band images | 125 |
| A.2 M 83 R-band images | 125 |
| A.3 NGC 7793 B(new)-band images | 126 |
| A.4 NGC 7993 B-band images | 126 |
| A.5 NGC 7993 V-band images | 127 |
| List of Tables | 138 |
| List of Figures | 140 |

Chapter 1

Introduction

The formation of galaxies is an important field in modern astronomy because all the cosmological models used to describe our Universe make predictions of the formation process of dark matter halos and for (visible) galaxies. Therefore if one were able to explain the formation of galaxies some of the cosmological models could be ruled out, while others could be favored. In the past, two conflicting galaxy formation scenarios have been proposed. On the one hand the “hierarchical clustering” scenario and on the other hand the “monolithic evolution” of galaxies. While the latter seems to be ruled out as being the only important formation process by new discoveries, namely that of the substructure in the Milky Way and the Andromeda galaxy (M31), the question if all galaxies are formed by the same mechanism is still open. The hierarchical formation models predict a wealth of substructure to be present in all larger galaxies. Here mergers play a fundamental role in building up the galaxies from smaller structures up to the largest galaxies that we are able to observe. Therefore smaller galaxies may be the building blocks of larger ones. However, there are still galaxies that do not show any signs of substructure or the amount of substructure is less than predicted by theoretical models. Chapter 2 will therefore introduce in short the different galaxy formation models, their predictions, and describe the current developments in this field of astronomy.

The aim of this work is to search for possible tidal streams, satellites or asymmetries in nearby galaxies because more data is still necessary. Up to now, complete studies revealing the stellar substructure exist only for galaxies of the Local Group and of the Andromeda Group. For galaxies more distant some evidence for substructure from surface photometry exists. Like M83 these show low surface brightness arcs in the halo or as in NGC 5907 a ring like structure perpendicular to disk.

With the help of stellar photometry using deep wide field imaging data, ob-

tained with the ESO MPG 2.2m at La Silla, more galaxies were investigated. A wide field image view enables the search over the complete galaxy instead of concentrating only on smaller parts. One major advantage of this method is that this wide field imaging data obtained with the same instrument has also undergone the same calibration steps. The data should be homogenous in itself which is important in detecting large scale asymmetries in the data.

Although the calibration of multi-chip CCD cameras is not an easy task, it will be shown (chapter 3) that it can be handled with the help of a reduction pipeline called *THELI*. *THELI* is a joint development of the “Argelander Institut für Astronomie” (University of Bonn) and the “Astronomisches Institut der Ruhr-Universität Bochum”. In its original design (see i.e. Erben et al. 2005) the pipeline was developed for the automatic reduction of wide field imaging data of large surveys. Such survey data is normally made up of exposures that do seldom contain large extended objects like nearby galaxies. In such a survey context it has already been shown that this pipeline works very well. Nevertheless, Schirmer et al. (2003) showed that with some manual intervention into the automatic process it is possible to reduce data sets that contain large objects. But as the aim for that study was not the photometry of stars the question of the usability of that data still remained open. To address this question the data was examined and photometrically calibrated. This showed that the results of the reduction are in very good agreement with standard star exposures up to the point where the illumination pattern of the telescope sets in. The calibration is discussed in detail in chapter 4.2 of this work. Some of these results were also published in our description of the pipeline in Erben et al. (2005). Hence, as the pipelines data quality in the sense of photometric studies is very good, the work is continued by reducing other ESO archival data. This is described in detail in chapter 3. The data contains other large scale objects like M 83 and NGC 7793 with the purpose of searching for anomalies in the distribution of stellar populations.

During the analysis, which is described in detail for each dataset in chapter 6, it became clear that searching for anomalies is a very challenging task as the features that one hopes to find are almost always near the detection limit. While it is in principle possible to count stars which reside in different bins of a color-magnitude diagram, this method could be influenced by photometric errors and, due to the application of necessary binning intervals, blind to find finer structures. To overcome such limitations of this simple star counting method, which is still very useful to get an overview of the stellar distribution of a galaxy, a method from data mining techniques, namely the fuzzy c-means clustering, is introduced. The basic idea of using clustering methods is to group together all objects that have something in common. In this case it puts together stars of similar luminosities that are concentrated in a small spatial region. Advantages and limitations of this are discussed in detail in chapter 5.3.2. The clustering analysis itself was

then carried out using the publicly available *KNIME*-Framework developed at the Institute for Bio-Informatics at the University of Konstanz. It will be shown that this framework is also very useful for this work in different ways. It may both acknowledge results from the star count method and derive a deeper insight into finer structures.

Finally this work will show that there seems to be some type of substructure or anomalies present in all of the galaxies in question. Therefore these results favor the predictions of the hierarchical clustering formation scenarios which predict a wealth of substructures to be present in all the galaxies. But as the substructures found in this work differ in type and quality it seems that local influences must be considered carefully. They may also play a major role in the formation process. Due to this the effects that are described in “secular evolution models” cannot be completely excluded in all cases of galaxy formation.

Chapter 2

General Physics of Galaxy Formation

This chapter will discuss the motivation for this work after giving a short summary on the physics that is important for the formation and evolution of galaxies. Therefore it starts with some basic descriptions of the cosmology and moves forward to the description of the most favored model that is used to explain the process of galaxy formation so far, the Λ CDM model. A complete discussion of this model is outside the scope of this short introduction and therefore many details which are not extremely relevant to this work are skipped.

In addition to this general overview of the field of astronomy relevant to this work, the chapter will end with a very short introduction of the galaxies used in this research.

2.1 Observational Evidence for DM

Observations of many different galaxies in the past and present have shown that they are built up by stars, gas and a third, yet unknown, component called dark matter. The postulation of dark matter is the result of the observation of the rotation curves of spiral galaxies. In contrast to a declining, Keplerian rotation curve in outer parts, which one would expect if a galaxy's matter only consisted of the gas and stars bound to the galaxy, many observations have shown that it behaves differently. The observed HI curves of the majority of galaxies are either flat or rising in the outer parts as it is shown in many publications (e.g. Rubin et al. 1980; Bosma 1981). Only very few galaxies like NGC 7793 seem to have a declining profile but even this profile could not be explained without the presence of some dark matter (Puche & Carignan 1991; Dicaire et al. 2008). Therefore, if one assumes the Newtonian gravity as valid, one has to include an additional and enormous amount of mass to reproduce the dynamics of galaxies. Surely such

amount of (dark) mass will play a significant role in cosmic structure formation and must be addressed accordingly in the models dealing with the formation and evolution of the universe.

2.2 Basic Cosmology

At present the genesis of the universe is explained with the “Big Bang” theory. Such a theory must also explain the inhomogeneous structure of the universe observed today. On the one side the existence of voids and overdense regions conflict with the postulation of the “Cosmological principle” of a homogeneous and isotrop universe on small scales (< 200 Mpc) but it is still valid on larger scales. On the other side it is known through observations that the cosmic microwave background (CMB) is indeed isotrop on larger scales. But it can be shown for two observations of the CMB in two different directions that it is impossible for the CMB photons to have been interacting with each other at the time of recombination. This is based on the assumption that no signal can travel faster than light. It is the so called “Horizon problem” which cannot be solved by the standard models of cosmology alone.

The important breakthrough was made at the beginning of the 80s with the invention of the “Inflationary theory” which introduced the concept of fluctuations into the standard models. Based on the assumption that the vacuum energy density must have been much higher than today, the cosmological constant must have dominated the Hubble expansion. As a consequence the expansion must be exponential. The matter in the universe at this time is described by the quantum field theory in which quantum fluctuations are possible. Such fluctuations represent temporary changes in the amount of energy in a point-space arising due to the Heisenberg uncertainty principle.

At the end of the exponential expansion a phase transition is described in which the former introduced quantum fluctuations transverse to real density fluctuations in the matter. Support for this view comes again from the CMB background because the measurement of small temperature anisotropies made in 1992 could be related to the density perturbations which arose during the inflation.

2.3 The Λ -CDM Model and the Substructure

The cold dark matter model is the currently accepted “standard” model that is based on the cosmology outlined in the previous paragraph. To explain the observations of the rotation curves a new type of matter, the dark matter, is introduced. It interacts with other particles only by weak or gravitational forces. The

processes involving dark matter are therefore dissipation-less. Hence, the total kinetic and potential energy of a dark matter system is conserved and can only be transferred between the potential and kinetic part. From the standard model of particle physics the neutralino (Gondolo 2004) is one of the most promising candidates for the dark matter particles.

As the fraction of dark matter outweighs the fraction of matter in baryonic form by a very large extent (more than 80 per cent of the matter is currently attributed to dark matter) it must be an important driver for cosmic structure formation. On scales much larger than the galaxies the dissipative effects of the baryon interactions cannot affect the matter distribution of the universe. Therefore, the building of larger structures in the universe is caused by the mass assembling of smaller dark matter structures. This process is called the “hierarchical clustering” and was in principle described by Press & Schechter (1974) and White (1979).

White (1978) and White (1979) used numerical N-body simulations to show that smaller-scale virialized spherical systems are able to merge into more centrally condensed elliptical ones having more extended envelopes. While the final density and velocity structure of the “new” system is influenced strongly by the rotational parameters of its progenitors, the internal structure and the initial orbit of the progenitors play only a minor role.

Press & Schechter (1974) calculated the mass function using a method now known as the “Press-Schechter”-formalism in which they assume an initial (linear) density field to which a Gaussian filter function is applied. The main argument of this formalism is that for a given characteristic wavelength the probability that any given point lies in an over-dense region is synonymous with the probability that this point has ever been processed through a collapsed object. The density field is therefore smoothed at different scale lengths in order to represent different masses, and then searched for local maxima. If such a maximum is large enough a spherical collapse is expected. In case of this the complete building of the structure would be described by the top-hat collapse model. As a result, this formalism gives then the number of bound objects formed during the evolution of the universe and this number could be compared with the number of large clusters observed now. Although this method has some drawbacks (half the mass remains unaccounted for, as it was i.e. shown by Peacock & Heavens (1990)), it still produces good agreements to some numerical simulations like the ones calculated by Efstathiou & Rees (1988) or Carlberg & Couchman (1989).

Summarizing this, both theories lead to models in which a decreasing redshift z is accompanied by a decreasing number of less massive collapsed objects. Instead more massive objects are expected. This behavior is also found in many newer N-body simulations which were carried out to get a deeper understanding of these processes based on the “hierarchical clustering” scenario and the Λ CDM cosmology. The largest and most time-consuming simulation addressing the large

scale structure of our universe so far has been the Virgo Consortium's Millennium Simulation (e.g. Springel 2005; Springel et al. 2005; Neto et al. 2007). This N-body simulation follows the structure of the universe using $2,160^3$ particles to simulate the universe from $z=127$ to the present. Using additionally a semi-analytic approach for simulating the galaxies itself, the complete run allowed them to calculate the galaxy two-point correlation function $\Xi(x,y)$:

$$P = (n \cdot dV)^2 \cdot [1 + \Xi, (x, y)] \quad (2.1)$$

The above formula 2.1 represents the probability P to find one galaxy at position x and another galaxy at position y within the volume dV. As one can see the two-point correlation function is a correction term describing the deviation of the probability P. In a completely homogenous and static universe one would use $P = (n \cdot dV)^2$ to describe the probability of finding two galaxies within the same volume dV. Although the Millennium Simulation was not tuned to match the observations, it reproduced the power law for the two-point correlation function as derived from the 2-degree Field Galaxy Redshift Survey (2dFGRS) and the Sloan Digital Sky Survey (SDSS) very well. In addition to this the simulation also showed that quasars are able to form early enough (massive progenitors visible at $z \simeq 16$) and that their descendants are found in rich galaxy clusters.

But numerical simulations of the evolution of our universe have also shown another interesting feature. Because the large mass halos are built by many smaller ones, a large mass halo should contain several subhalos. These subhalos are self-bound entities which survived the gravitational collapse, although such subhalos have suffered a strong mass loss due to tidal stripping. One reason for this was already seen in the first numerical simulations carried out by White (1979). There it was shown that the strength of tidal forces can be minimized if the progenitor systems are counter-rotating.

As a result of this large mass halos are expected to have many different subhalos inside their virial radius. In general, the virial radius is the radius of a sphere in which the density is n-times higher than the critical density defined by the Hubble parameter. A common choice (i.e. Carlberg et al. 1997) for n is 200 and the virial radius is then noted as r_{200} . Assuming that such subhalos should host luminous galaxies inside there should be plenty of satellites around very massive galaxies like the MilkyWay (MW) or Andromeda (M31). However, the observations so far have only found a very limiting number of satellites around the MW and Andromeda.

The substructure in Andromeda was first detected by Ibata et al. (2001) where they reported the finding of a giant stellar stream in the south-east of M 31. The giant stellar stream is a rectangular (stream-like) overdensity of RGB stars seen in the halo. The number of sources in the stream-region is about a factor of two

higher than in the non-stream region and is therefore statistically significant. In a further analysis (Ferguson & Johnson 2001) the authors presented a more detailed view of the giant stellar stream and reported two new stellar overdensities close to the south-western major axis and near the north-eastern major axis. The current research and observations carried out by this group showed, in addition to the afore mentioned structure, a wealth of substructures and streams present in M 31 (Ibata et al. 2007): Most of these structures lie inside the inner 20 kpc of the disk. Nevertheless, the giant stream is still the most prominent and largest structure which dominates the luminosity budget of M 31's inner halo. The halo, apart from the substructure, could be characterized as a smooth metal-poor component whose profile may be modeled by a Hernquist profile. But using such a profile the calculated scale radius of 55 kpc is a factor of 4 larger than predicted by simulations. More metal-rich components seem to be more centrally concentrated. Still, even in this larger and deeper survey in the region of M 31, no substructure was observed in the companion galaxy M 33 although the authors assume that the halos of M 31 and M 33 not only touch in projection but are rather passing through each other. A schematic view of the substructure in M 31 is shown in figure 2.1.

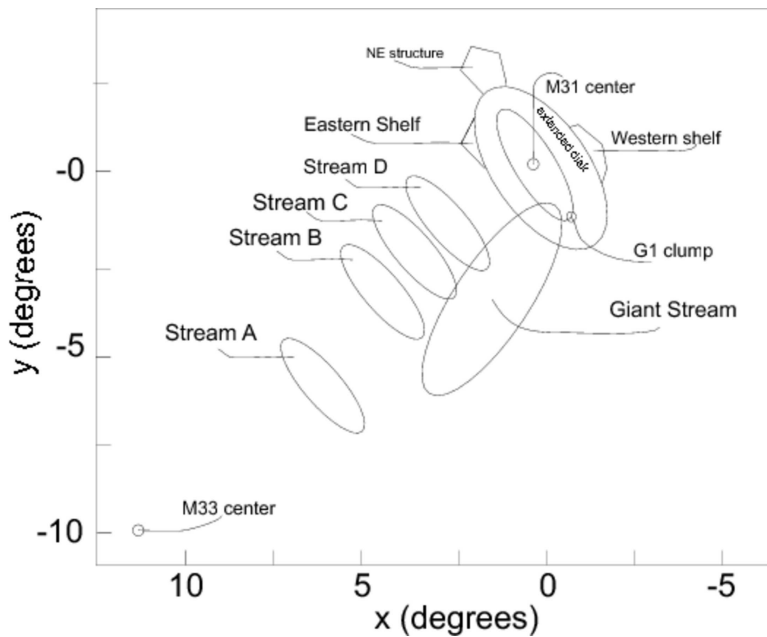


Figure 2.1: Replot of the substructure found around M 31 and M 33. The plot is based on the work and recent analysis of Ibata et al. (2007). It shows the positions of the most prominent features like the giant stellar stream, the overdensities in the East and West and the positions of the new streams nearly perpendicular to the giant stellar streams.

In the MW substructures have been reported by different groups so far. Ibata et al. (1995) increased the number of known MW satellites by finding a new satellite galaxy in the constellation of Sagittarius. The isodensity maps that were constructed in order to show the stellar distribution revealed a very elongated structure pointing to the center of the MW. Using images from the SDSS, Belokurov et al. (2006a) examined the Sagittarius streams in more detail and detected two branches which they labeled A and B. They showed that the two streams are representing material that has been torn off at different epochs. Again by the use of the SDSS Belokurov et al. (2007a) found another stream in the north Galactic cap. The discovered stellar populations are similar to that of the global clusters M 13 and M 92.

Another tidal stream was found by Newberg et al. (2006) which they called the “Virgo Stellar Stream”. The authors showed that there is another overdensity near the Sagittarius dwarf galaxies which cannot be explained by the tidal tails of Sagittarius. A ring of stars around the MW plane was reported by Yanny et al. (2003). In addition to this several detections of different smaller companions of the MW are reported by Belokurov et al. (2007b), Belokurov et al. (2006b), and Zucker et al. (2006).

2.4 The Missing Satellite Problem

As it was mentioned earlier the merging process of two dark matter structures may not be able to disrupt the inner parts of the progenitors in which an observable galaxy could be hosted. As pointed out, this behavior was already predicted by the early simulations of White (1979) but it was additionally verified by wide-field imaging observations of Natarajan et al. (1998) for a cluster of galaxies. Hence, there is the possibility of observing the substructure of dark matter halos by searching for substructure in the optical parts of a galaxy.

Comparing the number counts of observed tidal streams and satellites one could get the impression that a wealth of substructures was found and that this should be in agreement with the proposed Λ CMD scenario. But this is only true on a qualitative basis. Modern simulations have shown that the number of satellites predicted for galaxies like the MW or M 31 (Andromeda) is quite large. Moore et al. (1999) calculated the predicted number of satellites for a Milky Way halo to be about 500. These satellites should have masses larger than $10^8 M_{\odot}$ and sizes ≥ 1 kpc. Similar results are also obtained by other groups like Klypin et al. (1999). These simulations agree very well with the mass range $\geq 10^8 M_{\odot}$ and with about 300 predicted satellites this is of the same order of magnitude. Comparing it with the number of about 40 satellites in the Local Group there is a large discrepancy present between observation and theory. Several possible solutions are presented

that could account for the missing satellites:

High Velocity Clouds

Blitz et al. (1999) suggested high-velocity clouds (HVC) as an observational counterpart of low-mass DM halos. Stability arguments place the mass of HVC in the same region as predicted by the models for the observable part of the DM halo. Nevertheless, the exact number of HVCs in the MW is still unknown. An estimation of the number of all HVCs (Wakker & van Woerden 1991) would lead to a mass for the DM higher than that predicted by the simulations. But this problem could be resolved by the assumption that HVCs may be of different sizes and shapes. Hence, only the more massive ones are embedded in a larger DM halo.

Dark Satellites

Another explanation could be the existence of dark satellites. Two physical processes are able to support such a scenario: Gas ejection by supernova driven winds (Dekel & Silk 1986) which happened in the early universe could produce satellites with a high mass-to-light (M/L) ratio that could go undetected. Alternatively, the prevention of a gas collapse or the photoionization of the gas in low-mass systems, due to the strong ionizing intergalactic background, are able to create DM halos without observational counterparts in the optical. Such a scenario was suggested by Rees (1986). Bullock et al. (2000) carried out a numerical simulation including the suppression of gas accretion due to UV background in the early universe and showed that this could really explain the missing satellites. As a consequence the reionisation redshift z must be relatively low with $z \approx 12$. The only way to detect such dark halos would then be by weak gravitational lensing effects.

Incompleteness of Observation

Naturally, it is also possible that the discrepancy is due to observational incompleteness. In Mateo (1998) there is the prediction that about 20 dwarf galaxies could be undetected. In addition to this the circular velocities that are used for the mass estimation may be wrong by at least a factor of two (Pryor & Kormendy 1990). This would then translate to a wrong mass estimation of the DM system.

Summarizing this, the missing satellite problem is one of the main problems of the Λ CDM scenarios. The search for new substructure is certainly not the expected solution because it seems to be unlikely that observational incompleteness will account for all the missing satellites. The physical processes seem to be more likely for solving this problem. Nevertheless, it would not be without importance to quantify the amount of missing satellites due to incompleteness of observations

as it will influence the parameters needed to solve simulations that integrate the physical processes summarized before.

2.5 Galaxy Evolution

While it has been shown that there is a missing satellite problem in the Λ CDM scenario and the search for substructure is neither the only nor the best solution to solve this problem, it is still interesting and important to quantify the number of substructures observed.

Until now, only for the MW and M31 detailed studies exist. As such studies depend on a good spatial resolution only the closest objects can be studied in more details. Members of the Local Group and, as will be shown in this thesis, members of the Sculptor Group represent good candidates for such study. Hence the distance of a few Megaparsec should not be exceeded unless one wants to spent a very large amount of observing time. Resolving single stars is still not possible for galaxies far away. While surface photometry could in principle be used in finding substructures in the form of tidal tails or satellites, this method has other disadvantages. The biggest problem of surface photometry is the limitation due to the night sky brightness (see also chapter 5.2). Nevertheless, there are publications using surface photometric measurements to show substructures in the form of tidal tails in other galaxies, i.e. Wehner & Gallagher (2005) for NGC 3310, Bastian et al. (2005) in the case of NGC 6872 or Shang et al. (1998) for NGC 5907.

Therefore, the main reason in searching for substructures is to get an understanding of galaxy evolution. While the Λ CDM scenario is a good model to explain the substructure of the universe and the formation of the first galaxies including their mass assembling, it is still not clear how galaxies evolve during their lifetime. The scenario of the “hierarchical clustering” competes with the model of “secular evolution”. The importance of inner processes that are well described in the models of “secular evolution” has already be shown by different groups like Block et al. (2002) or Kormendy & Kennicutt (2004).

In the past there was also the so-called “monolithic model” for galaxy formation in which all the galaxies formed at a given epoch when the physical properties were favorable to initiate such huge accretion of mass. The main parameters of a galaxy were assumed to be determined by this initial accretion event while the environment has only a small influence on the evolution of the galaxy itself. In such a scenario the galaxies maintain at every z the same proportion of their morphological types but evolution in luminosity or in the spectral type is still allowed. Due to this behavior the models are also referred to as “pure luminosity evolution” (PLE) models (Bruzual A. & Kron 1980). Even in 2002 it was shown by Cimatti et al. (2002) that in revised versions of this PLE models the results (e.g. Pozzetti

et al. 1996) *are in broad agreement with the expectations of PLE models, while disagree with the predictions of current hierarchical merging models of galaxy formation [...]*

The detection of the substructure and the better understanding of the effects of baryonic physics, gas accretion, gas dissipation, star formation feedback etc. ruled out the importance of the pure PLE models. Instead of the PLE models, the models describing the “secular evolution” now play an important counterpart to the hierarchical clustering as the main driver for galaxy evolution.

“Secular evolution” describes the slow rearrangement of energy and mass inside a galaxy. This evolution is driven by bars, the spiral structure and also by triaxial dark halos around the galaxy (Kormendy & Kennicutt 2004). Destruction and reformation of the bars and the accretion of surrounding gas into the galaxy produce gravity torques which are efficient to drive matter inwards. As a result the galaxy morphological type evolves toward early-types (Block et al. 2002).

In contrast to the slowly occurring processes which are described using the “secular evolution” models the “hierarchical clustering” models explain the transformation of late type spirals to early type ellipticals by merging events. Already the first simulations (White 1979) showed a trend in the merging process to produce structures more likely resembling the structure of ellipticals. Newer simulation have shown that ellipticals can also be produced by mergers of disk-galaxies (Feldmann et al. 2008), during minor mergers (Bournaud et al. 2007) or during mergers of early type galaxies containing very little cold gas (Whitaker & van Dokkum 2008).

To summarize this, both models are able to explain the observed morphologies of galaxies and both models agree with the inversion of the hubble tuning fork diagram of galaxies. Hence, one observes a transformation from (late Hubble-type) spiral galaxies to (early Hubble-type) ellipticals. It seems also clear that both models are true, depending on the environment of a galaxy. In a rich cluster of galaxies mergers could have a larger impact on the evolution. Here the “hierarchical clustering” models are able to give a detailed description of what was/is going on. In galaxies far away from any companion the gas accretion and internal processes could be the driver of the evolution. The discussion is therefore not about the question if one should favor this or that model. Instead it is about how much of a galaxy’s evolution is attributed to merging events or to internal physical processes like gas accretion. Hence, the relative importance of each model is unknown at the moment. It is also possible that the choice of using this or that model is time dependent. While at the beginning of the universe the morphology of galaxies was more likely driven by mergers, it might now (or in some distant future) be driven only by internal processes.

Therefore, the finding of substructures in form of satellites or tidal tails is important because it is unknown if such substructure is present in all galaxies. If

this were be true, then mergers must play a significant role in galaxy evolution or they must at least have played an important role in the past. The observed morphologies are then more likely to be the product of merging events and then maybe most of the morphology transformations between spirals and ellipticals could be induced by such events. If on the other hand a significant fraction of (spiral and elliptical) galaxies do not show any signs of substructure it would prove that current morphologies may be explained by internal processes. The possibility that in such galaxies the signs of mergers might have faded out because merging occurred extremely early would still be possible. But the more galaxies without substructure are found the more unlikely this would be.

This work will try to extend the current distance-range of more detailed searches using wide-field imaging photometric data. The wide-field approach has the advantage that the galaxies in question are fully covered and as for most of these galaxies no a priori hints for substructure exist (with the exception of the M83 surface brightness stream) this seems to be the best approach to that question. Using e.g. space based instruments like the Hubble's WFPC 2 or the ACS camera would limit useable FOV to about 150×150 arcseconds and 202×202 arcseconds. This is very small in comparison to the 34×34 arcminutes of the ESO/MPG 2.2m Wide-Field Imager which is therefore much better suited for an unspecified global search. The big advantage of the higher resolution of WFPC 2 and ACS would nevertheless suit better for detailed insights in structures but for the time being a list of possible targets is needed.

2.6 The Galaxies

This paragraph will summarize and introduce in short the galaxies which were examined in this thesis. The distance to the galaxies considered does not exceed 10 Mpc, a limit set by the necessity to resolve single stars for larger parts of the galaxies. This section will express some common knowledge of these galaxies that was obtained with other observations. A deeper discussion of previous findings relevant to or affecting this work will be discussed in the associated data analysis in chapter 6

2.6.1 NGC 300

NGC 300 is a late type spiral galaxy of type SA(s)d (Tully 1988) and one of the brightest members of the Sculptor Group. Its inclination is $i \approx 42^\circ$ and its distance modulus is assumed to be $m - M_0 = 26.43 \pm 0.09$ according to Cepheid distances measured by Gieren et al. (2004). Numerous giant HII regions and evidence of ongoing star formation is seen on H α maps.

According to Blair & Long (1997) the sample of supernova remnants shows properties similar to that of M 33's SNR. Even in its mass, size and luminosity NGC 300 is similar to M 33. The only significant difference in this is the presence of the large and massive M 31 galaxy near M 33 whereas NGC 300 seems to be relatively isolated.

NGC 300 was included in this work because many wide field images were available from this galaxy (see also chapter 3.2.2). This led to a very deep co-added image of this galaxy suitable for the search for tidal streams and other kinds of substructure. The proximity of this galaxy is another important fact as it allows resolving the stellar contents in the outer parts using wide field imagers.

2.6.2 M 83

M 83 is a grand design spiral of type SAB (Tully 1988). With an inclination of $i \approx 24^\circ$ as reported by Talbot et al. (1979) this galaxy is seen nearly face on. Recently a deep study carried out by Harris et al. (2001) has found evidence of violent star formation taking place in M 83. In addition to this a low surface brightness arc was found in the halo of M 83 by Malin & Hadley (1997).

Although with the distance modulus of 28.25 magnitudes (Thim et al. 2003) M 83 is more distant than the other galaxies in this study the discovery of such an arc is very promising. Based on the presence of this arc it was included in this sample although the integrated observed time of archival images was not very high.

2.6.3 M 33

M 33 is a late type spiral of type SA(s)cd. It is the third known spiral in the Local Group beside the Milky Way and Andromeda (M 31). It should be pointed out

| Parameter | Value | Reference |
|---------------------------|--------------------|------------------------------|
| α_{2000} | $0^h54^m53^s.48$ | 2MASS TEAM (2003) |
| δ_{2000} | $-37^\circ41'03''$ | 2MASS TEAM (2003) |
| Position (Gal. Longitude) | 299.208651d | 2MASS TEAM (2003) |
| Position (Gal. Latitude) | -79.418818d | 2MASS TEAM (2003) |
| Helio Radial Velocity | 142 +/- 4 km/s | de Vaucouleurs et al. (1991) |
| Redshift | 0.00048 | Lauberts & Valentijn (1989) |
| Distance-Modulus | 26.43 magnitudes | Gieren et al. (2004) |
| Extinction E(B-V) | 0.013 | Schlegel et al. (1998) |

Table 2.1: NGC 300 parameters as derived from different studies

| Parameter | Value | Reference |
|---------------------------|--------------------|--------------------------|
| α_{2000} | $13^h37^m00^s.9$ | 2MASS TEAM (2003) |
| δ_{2000} | $-29^\circ51'56''$ | 2MASS TEAM (2003) |
| Position (Gal. Longitude) | 31.5837795d | 2MASS TEAM (2003) |
| Position (Gal. Latitude) | 31.9730496d | 2MASS TEAM (2003) |
| Helio Radial Velocity | 513 +/- 4 km/s | Koribalski et al. (2004) |
| Redshift | 0.001711 | Koribalski et al. (2004) |
| Distance-Modulus | 28.25 magnitudes | Thim et al. (2003) |
| Extinction E(B-V) | 0.066 | Schlegel et al. (1998) |

Table 2.2: M 83 parameters as derived from different studies

that M 33 lies near the Andromeda galaxy and it was stated by Ibata et al. (2007) that the halos of both galaxies are likely to overlap. A distance modulus of about 24.67 (Sarajedini et al. 2006) places this galaxy about 70 kpc beyond M 31 in line-of-sight distance.

It was included in this sample because the data at hand was deep enough for a detailed photometric study with the aim of finding some kinds of substructure even if previous studies have not found any signs for such substructure. But the studies available allow a cross-checking of the results of the new data-mining approach.

2.6.4 NGC 7793

NGC 7793 is also a member of the Sculptor Group and has an inclination $i \approx 53^\circ$. This galaxy belongs to the five brightest members of its group and in contrast to NGC 300 it does not show a clear defined spiral pattern. Therefore it is attributed to the class of “flocculent” spirals. This is also true in the infrared (Elmegreen 1981). In addition it contains a large number of HII regions and OB associa-

| Parameter | Value | Reference |
|---------------------------|-------------------|------------------------------|
| α_{2000} | $01^h33^m50^s.9$ | 2MASS TEAM (2003) |
| δ_{2000} | $30^\circ39'36''$ | 2MASS TEAM (2003) |
| Position (Gal. Longitude) | 133.610265 | 2MASS TEAM (2003) |
| Position (Gal. Latitude) | -31.330853 | 2MASS TEAM (2003) |
| Helio Radial Velocity | - 179 +/- 4 km/s | de Vaucouleurs et al. (1991) |
| Redshift | 0.000597 | de Vaucouleurs et al. (1991) |
| Distance-Modulus | 24.67 magnitudes | Sarajedini et al. (2006) |
| Extinction E(B-V) | 0.042 | Schlegel et al. (1998) |

Table 2.3: M 33 parameters as derived from different studies

tions (Pietrzyński et al. 2005). The distance to this galaxy is about 3.91 Mpc (Karachentsev et al. 2003).

NGC 7793 was included because a larger wide field photometric imaging data set was available. In addition to this, being another member of the Sculptor Group it is still in the range needed for resolving the outer stellar content.

| Parameter | Value | Reference |
|-------------------------------|--------------------|----------------------------|
| α_{2000} | $23^h57^m49^s.8$ | 2MASS TEAM (2003) |
| δ_{2000} | $-32^\circ35'28''$ | 2MASS TEAM (2003) |
| Position (Galactic Longitude) | 4.515333 | 2MASS TEAM (2003) |
| Position (Galactic Latitude) | -77.171377 | 2MASS TEAM (2003) |
| Helio Radial Velocity | 227 +/- 2 km/s | Koribalski et al. (2004) |
| Redshift | 0.000757 | Koribalski et al. (2004) |
| Distance-Modulus | 27.96 magnitudes | Karachentsev et al. (2003) |
| Extinction E(B-V) | 0.019 | Schlegel et al. (1998) |

Table 2.4: NGC 7793 parameters as derived from different studies

Data Reduction

3.1 General Discussion

This chapter will present the data reduction process. It will describe all steps necessary to reduce the raw science data in order to get a scientific valuable image. Therefore this chapter will start with a basic description of the data used for the scientific analysis which is described in chapter 6. This is followed by the description of the reduction process itself.

3.2 Overview of the Datasets

3.2.1 Telescope & Detector

Except for the data of M 33 all the data was taken with the MPG/ESO 2.2m Wide-Field Imager at La Silla in Chile. It is a focal reducer-type camera (permanently) mounted at the Cassegrain focus of the telescope. The complete field of view is about 34 arcmin x 33 arcmin with a pixel size of 0.238 arcseconds in each direction. The mosaic of the eight CCDs is arranged in a 4 x 2 style, with each CCD having 2k x 4k pixel, so that the covered area on the sky is nearly a square. In the vertical direction the gap between each of the four CCDs is about 23 arcseconds while in the horizontal direction the gap is about 14 arcseconds. A complete raw image in FITS format (containing the extensions) is about 142 Megabyte. On the average the eight CCDs have a read-out noise of 4.5 electrons per pixel and the inverse gain is about 2.0 electrons per ADU. According to ESO's web page¹ the best seeing to expect with this instrument is about 0.7 arcseconds and a very good

¹see <http://www.lis.eso.org/lasilla/sciops/2p2/E2p2M/WFI/docs/WFIimagequality.html>

seeing is about 0.9 arcseconds. Typically values of the seeing are around 1.1 arcseconds. A complete overview of the instrument and its performance is available online at <http://www.lis.eso.org/lasilla/sciops/2p2/E2p2M/WFI/>.

3.2.2 NGC 300 Data

The data of NGC 300 used was already reduced by Mischa Schirmer for a study dealing with the anatomy of galaxy clusters in the background of NGC 300 (Schirmer et al. 2003). From his study the reduced images of NGC 300 in B,V,R and $H\alpha$ were taken. The data itself was archival data observed in 34 nights between July 1999 and January 2000 and it was retrieved from the ESO Archive by Mischa Schirmer. These are the same images which were already used to construct the ESO color-composite Press-release Photo(s) 18a-h/02². The data fully covers an area of about 14 kpc around NGC 300.

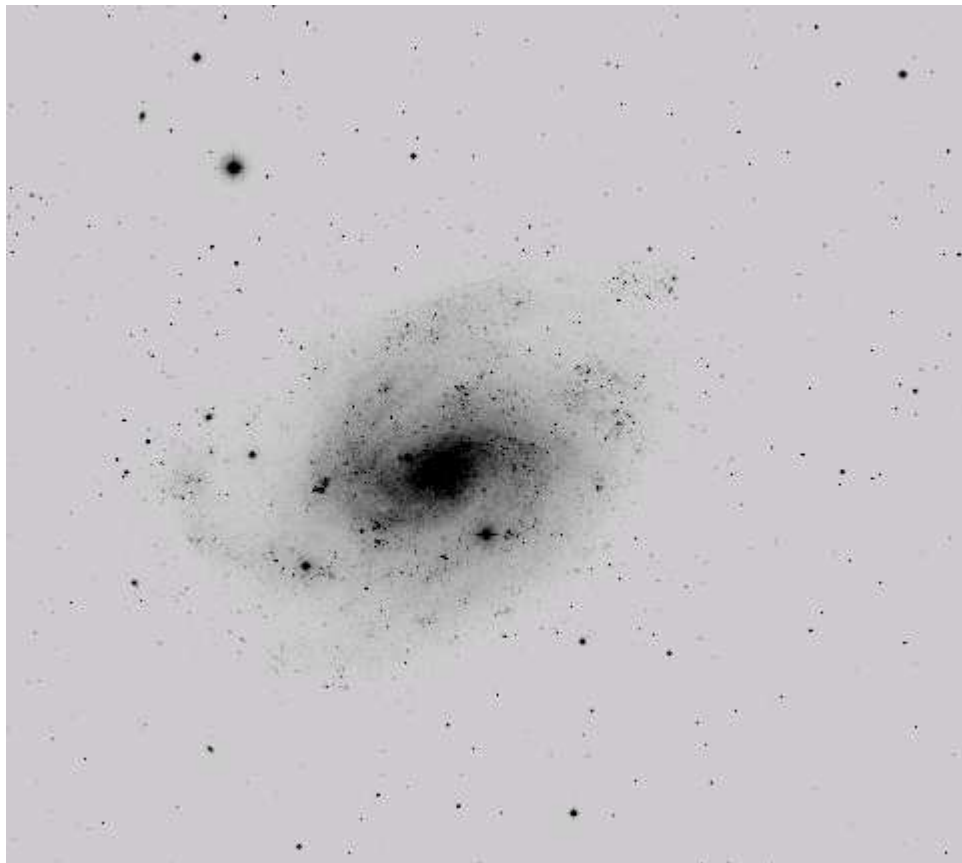


Figure 3.1: V-band image of NGC 300 reduced by Mischa Schirmer

²see <http://www.eso.org/public/outreach/press-rel/pr-2002/phot-18-02.html>

A description of the reduction steps of this dataset will not be given here as there is already an extensive discussion on this topic in his publication (Schirmer et al. 2003). Instead, table 3.1 contains important information regarding the analysis. In comparison to the other images reduced for the first time using this pipeline one should keep in mind that NGC 300 was reduced with an early version of the pipeline. At this time some of the pipeline steps were carried out manually as appropriate automatic routines were not fully implemented (e.g. sky subtraction). Additionally, since then some tasks and tools have been replaced by others. To name a few, the co-addition formally done using the IRAF *DRIZZLE* task has been replaced by *SWARP* and the astrometry is now based on *ASTROMETRIX* alone instead of using a combination of the LDAC-Tools and *ASTROMETRIX*. Here the work with this data begins at the point where stellar photometry and the transformation of the instrumental magnitudes to standard magnitudes set in.

| Filter | Exposure time | Average seeing |
|------------|---------------|-------------------|
| B | ~ 11.0 hours | ~ 1.09 arcseconds |
| V | ~ 10.4 hours | ~ 1.02 arcseconds |
| R | ~ 4.3 hours | ~ 1.02 arcseconds |
| H α | ~ 5.1 hours | ~ 1.12 arcseconds |

Table 3.1: Some important parameters of the NGC 300 data. All values refer to the final co-added image.

3.2.3 M 83 Data

The M 83 data was also retrieved from the ESO Archive. It consists of raw images taken in several nights beginning in March 2000 and ending April 2004 in B, V, R and H α filters. Some of the R-band images had a larger offset from the central position on M 83 and could not be used for the co-added image. Unfortunately, the combined exposure time for this new position is only half the exposure time of the central part and therefore not sufficient for a further analysis. The images used fully cover an area of about 22 kpc around M 83.

This data set was also the first for this thesis that had to be fully reduced using the pipeline. During its reduction the sky-subtracting step was changed to simplify automatic reduction.

3.2.4 NGC 7793

The dataset of NGC 7793 is the second dataset that was fully reduced with the pipeline. The data was retrieved from the ESO Archive and was, like the NGC 300

| Filter | Exposure time | Average seeing |
|------------|---------------|-------------------|
| B | 3455 seconds | ~ 0.95 arcseconds |
| V | 5568 seconds | ~ 0.86 arcseconds |
| R | 5299 seconds | ~ 1.12 arcseconds |
| H α | 2759 seconds | ~ 1.22 arcseconds |

Table 3.2: Some important parameters of the M 83 data. All values refer to the final co-added image.

data, originally observed for the *Araucaria*-Project developed by G. Pietrzynski and W. Gieren (Pietrzyński & Gieren 2006). This is a long term observational project based on wide field imaging data of nearby galaxies. One of its main goals is the analysis of cepheids. NGC 7793 images were observed starting in July 2002 and ending in October 2004 in the B-,V- and I-band. As it will be shown later, the fringing in the I-band data was too large to be reduced and co-added using the *THELI*-pipeline. For the B-band two different B-filter images, both with its own set of calibration data, were available namely the B-NEW and the B-123 filters. Both filters were reduced and co-added individually to select the one with the higher combined exposure time for further analysis. In addition, many standard star observations were made in nearly all observational runs. The data fully covers an area of about 18 kpc around this galaxy.

| Filter | Exposure time | Average seeing |
|--------|---------------|-------------------|
| B-NEW | 27356 seconds | ~ 1.07 arcseconds |
| B-123 | 32396 seconds | ~ 0.88 arcseconds |
| V | 58983 seconds | ~ 1.01 arcseconds |

Table 3.3: Some important parameters of the NGC 7793 data. All values refer to the final co-added image.

3.2.5 M33

This data was observed by the National Optical Astronomy Observatory (NOAO) Local Group Survey and published by Massey et al. (2006). It was taken with the Mosaic CCD camera at the prime focus of the 4m Mayall telescope. Its pixel scale is of 0.261 pixel per arcsecond and the field of view is 35 arcminutes. The eight single CCD camera chips used are also a 2048x4096 construction. The central area covered by this data set is around 4.5 kpc. While the publicly available data was reduced by Massey et al. (2006), the photometric calibration was made by

Burggraf et al. (2005) during her diploma thesis for a study of the “Environment of LBVs”.

3.3 The *THELI*-Pipeline

The *THELI*-pipeline (Erben et al. 2005) is a joint development, in which I participated during the time of this PHD project, between the “Argelander-Institut für Astronomie” (Universität Bonn) and the “Astronomisches Institut der Ruhr-Universität Bochum”. The primary goal of this pipeline is to simplify and to standardize the automatic reduction of Mosaic Wide Field Imagers (WFI). In contrast to the well-known single chip reduction techniques, the reduction of data from a multi-chip detector array faces additional difficulties that are addressed by the *THELI*-pipeline. These difficulties are the consequence of variations between each of the chips and the misalignment of the chips with respect to each other inside the instrument. Variations between the chips cannot be excluded even if adequate care is applied during the manufacturing process. Cold and hot pixels, the slight difference in the gain (sensitivity variations) or the difference in the dark current between each of the chips are good examples for this. So during the reduction of mosaic data such variations must be taken care of. The final stacking of the image can only be done after applying the necessary corrections. Another correction has to be applied for optical distortions that are the result of the position and/or misalignment of the chips inside the instrument³. Some areas of each chip may lie at the edge of the focal plane. As a result of this it is not sufficient to calculate a single order astrometric solution that takes care of the displacement of the chips alone. Instead of this the complete solution must include dealing with the distortion inside a single chip. Finally, this solution will be applied during a

³see also <http://www.ls.eso.org/lasilla/sciops/2p2/E2p2M/WFI/docs/WFInutshell.html> for a detailed description of tilt between WFI-Chips

| Filter | Exposure time | Average seeing |
|--------|----------------|-------------------|
| U | ~ 3600 seconds | ~ 0.94 arcseconds |
| B | ~ 660 seconds | ~ 0.96 arcseconds |
| V | ~ 360 seconds | ~ 0.88 arcseconds |
| R | ~ 300 seconds | ~ 0.81 arcseconds |
| I | ~ 900 seconds | ~ 0.93 arcseconds |

Table 3.4: Some important parameters of the M 33 data. The exposure times are taken from Massey et al. (2006). The estimation of the seeing is taken from the diploma thesis of B. Burggraf.

rescaling step to prepare the individual images for the co-addition process in the sense that they are placed on a homogenous and linear grid.

Our pipeline has been developed with all these problems of multi-chip cameras in mind. Instead of designing it from scratch it is a collection of scripts and publicly available programs which are specialized in single tasks. All these programs, e.g. Mario Radovich's *ASTROMETRIX*⁴, are known to work well in the reduction of astronomical data and they were grouped together by us in a way to automate the data reduction. In the next paragraphs the steps and the tasks used for the reduction of the datasets will be named and summarized. This is done because of the fact that, in comparison to the early version, some of the tasks have been replaced by others but the basic ideas and the outline of the reduction steps are still the same:

It starts with splitting up the multi-extension fits data (per observation run) on a detector basis and performing the basic reduction like bias-processing, flat fielding, bad pixel mask creation, superflating, fringing correction (if necessary and possible) and so on. After performing these basic reduction steps the images are arranged into an appropriate set which is the sum of all images of a single object observed (including also observations from different runs) in the same filter. On a set the astrometric solution will be calculated and afterwards the photometric alignment to a common photometric zero-point is performed. Just before co-adding all the images to create the final reduced mosaic, the sky background is calculated and subtracted. This brings all images to the same background level. A more detailed description of the reduction process with accentuation of some problems which arose due to the nature of this data may be found in the next section.

3.4 Data Reduction in Detail

The data reduction carried out for M 83 and NGC 7793 was done using the aforementioned *THELI*-Pipeline. The main difference between the typical data the pipeline was designed for and the data at hand is the presence of an extended object in the center of each mosaic-image. This possibility was not excluded by the initial design goal of the pipeline but main emphasis was placed on the reduction of a large number of “empty” stellar fields or deep sky surveys like the “ESO Deep Public Survey” (Hildebrandt et al. 2006) in whose reduction I also participated. As mentioned before, the data was observed with the 2.2m ESO/MPG WFI. The images were stored in a multi-extension fits file where each frame of a single CCD is stored in one of its extensions. A short outline of the

⁴see <http://www.na.astro.it/radovich/>

reduction steps and its dependence among each other is presented in figure 3.2.

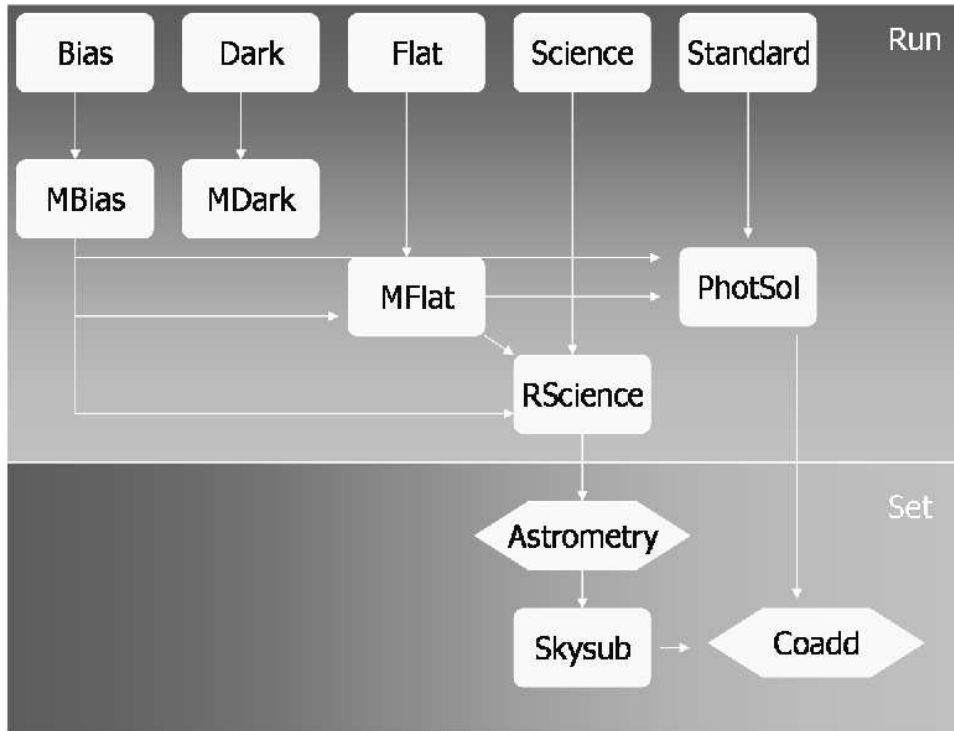


Figure 3.2: Simple outline of the reduction steps using the *THELI*-pipeline. The reduction processes are described in the text.

3.4.1 PRE-Reduction

Before the reduction begins the data must be ordered by the time of observation (this will be called a complete run). Then the images in each run will be subdivided into further classes according to their observational type: These are bias-frames, dark-frames, flat-frames, standard-star observations and science-frames. A complete list of the runs and the number of images available is given in the appendix. To speed up the sorting of the files a script called *initial_WFI_sort.sh* was created to take care of this. This script uses the ESO FITS-Header information to define the observational type and moves the images to a corresponding directory. Additionally, the script creates a text file that contains the names of all images which could not be sorted. This may be due to missing or ambiguous header keywords like 'flat' instead of 'sky-flat' or 'dome-flat'. Sorting of filters is done using the filter-wheel number and should therefore be valid during a single observation run. For different runs one has to take care that the same number applies to the

same filter. To stress this point the directories created by the script are named using a pattern like *BIAS_XX* where *XX* is the filter number instead of the filter name. The reason for this was the ambiguity with some filter name descriptions.

3.4.2 RUN-Based-Reduction

After this sorting was done, splitting of the multi-header FITS files provides standard FITS files to work on. For overscan, bias and flat-field correction the standard pipeline scripts were used to create, where necessary, the appropriate master files and to apply these to the images. Such bash-scripts itself are the pipeline front-end for the implemented eclipse and qfits tools written by Devillard (2001). After the flat-field correction of the science and standard star observations the pipeline would proceed in creating and applying a superflat to the images to extract the so called 'flat-field pattern' from the science frames. The construction of the superflat as it is implemented follows a method developed by Alcalá et al. (2002). It is created out of flat-fielded science exposures that are smoothed with a large kernel. This smoothing should be able to extract large scale variations but to work it naturally requires the absence of any other large scale variation(s) due to objects in the image. As mentioned before, all the mosaic images cover a large galaxy so that the precondition for creating a superflat are not met. On this account this step has been skipped.

The next step produces the individual WEIGHT maps. The pipeline now uses the MasterFlat rescaled to unity in order to provide a map that reflects the sensitivity of the pixels along each chip. Also in this step the MasterDark is used to mask bad pixels by setting their value to zero in a WEIGHT map. In its current state this is the only value of dark exposures used in the pipeline. Dark frames are preferred because of the fact that bad pixels stand out from the noise more clearly in a lengthy exposure. A subtraction of the dark current is yet not implemented and for the majority of CCDs used for optical imaging the cooling leads to a negligible dark current. The dark current for the WFI is of the order of 3.8 electrons per hour per pixel according to ESOs testing of the CCDs⁵. This would be a signal of about 2 ADU in an observation and is of the same order or smaller than the read-out noise which is varying in range of 4 to 8 electrons (depending on the CCD and time measured).

3.4.3 Fringing in the I-Band

For I-band images the WFI shows a strong fringing pattern visible as a wave-like structure on an observation frame. While the geometry of this additional structure

⁵see <http://www.eso.org/projects/odt/WFI/dccte.html> or the WFI Users manual

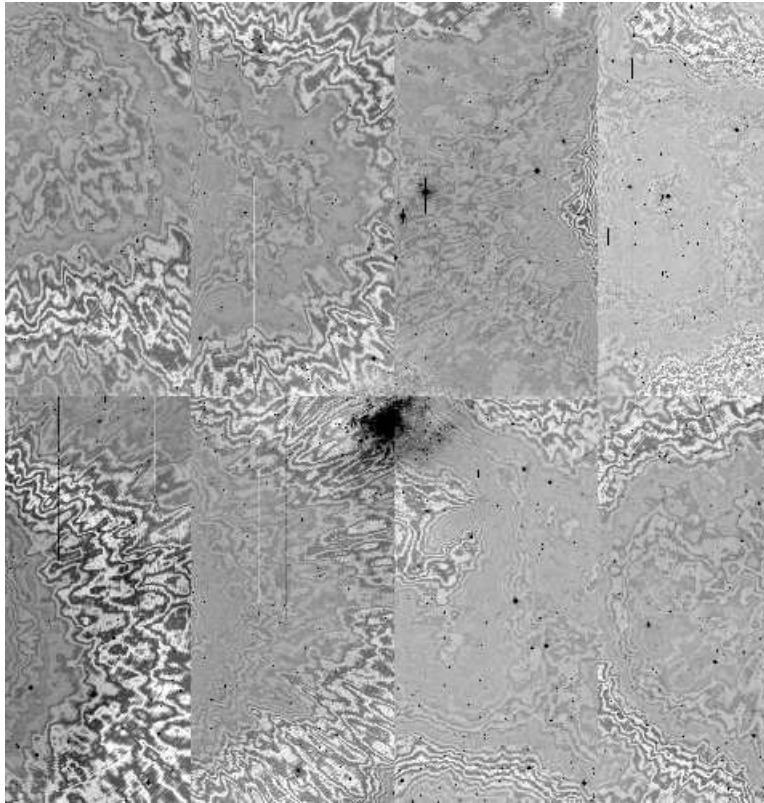


Figure 3.3: Example of an image after fringing correction was applied. The fringing pattern is still visible showing that the standard fringing correction methods did not work. The amplitudes of the fringing pattern varies from a minimum value of 4 % to a maximum of about 10 %.

does not change much with time, the amplitude indeed does. The reason for this is that fringing is an interference effect created in the substrate of the CCD and the geometry is therefore caused by the CCD itself. The amplitude however depends on the light received which means it depends strongly on the night sky conditions. The *THELI* pipeline is in principle able to correct for this pattern if the amplitudes are not too high and if a good superflat exists, but as said above this is not the case for this data. Instead of this, standard star observations were used to construct such a superflat and to create a correction map. Figure 3.3 shows the result of this try for an image of NGC 7793. It is evident that this method still did not work out well enough to reduce the I-band frames. As the fringing pattern will make the photometry unpredictable these images cannot be used for further analysis.

3.4.4 SET-Based-Reduction

After the completion of the run-based-reduction the data is organized into sets according to the targets observed. The set-based-reduction begins with computing an astrometric solution for each image. In this step the pipeline now uses the *ASTROMETRIX* program written by Radovich (2002a) to calculate a third order polynomial solution for each image. Creating the catalog of stars that will be compared to the reference catalog (either USNO-A2 or GSC2 can be chosen) is done by *SEXTRACTOR* (Bertin 2002), which extracts all high S/N objects in each image. The astrometry is a crucial step for co-adding the data as its results are important for the alignment of the images. The gaps, present between the single CCD chips in each exposure, make this step even more complicated. For good astrometry a sufficient large overlap between different exposures must exist and this has to be accounted for during the observation by using an appropriate dithering pattern. But even if all of this has been done with great care, astrometry could go wrong. Reasons for this may be a bad coverage of astrometric standard stars or that the order of the astrometric solution applied is too low (solution is bad) or too high (no solution may be found at all). In many cases the coverage of standard stars can be increased by extracting more stars from the standard catalog which will improve the calculated solution at the cost of more computing time. The same holds if one requires a higher polynomial order for the solution. Another reason for a bad astrometry solution is the possibility that wrong coordinates might be written into the image header. To reduce the computational effort in solving the astrometric problem for each image there must be a rough estimate on the position in the sky present in the header. If this header keywords (CRVAL1, CRVAL2) are missing or the values are wrong then the matching between catalog stars and observed stars might fail. In such a case no astrometric solution will be found. A possibility for a bad global astrometry is due to missing or bad astrometry of a few single frames. In figure 3.4 such a co-added frame is shown. In it three reflections are seen for the majority of stars. These reflections are the stars of all the images which could not be correctly aligned to the common astrometric zero-point. In addition to this the center of the image shows the result of a bad sky-subtraction which will be discussed in the next paragraph.

After astrometry the relative photometric zero-points are calculated for each image using the *PHOTOMETRIX* task, also written by Radovich (2002b). This is necessary to adjust all images to a common photometric zero-point during the final co-addition process. As observations in a set may have been taken under different sky conditions or may have different exposure times the images must be normalized. The last step before co-addition is then the sky subtraction in order to bring all images to the same sky-background. In the original design of the pipeline a model of the night sky was created after a *SEXTRACTOR* run to detect all large

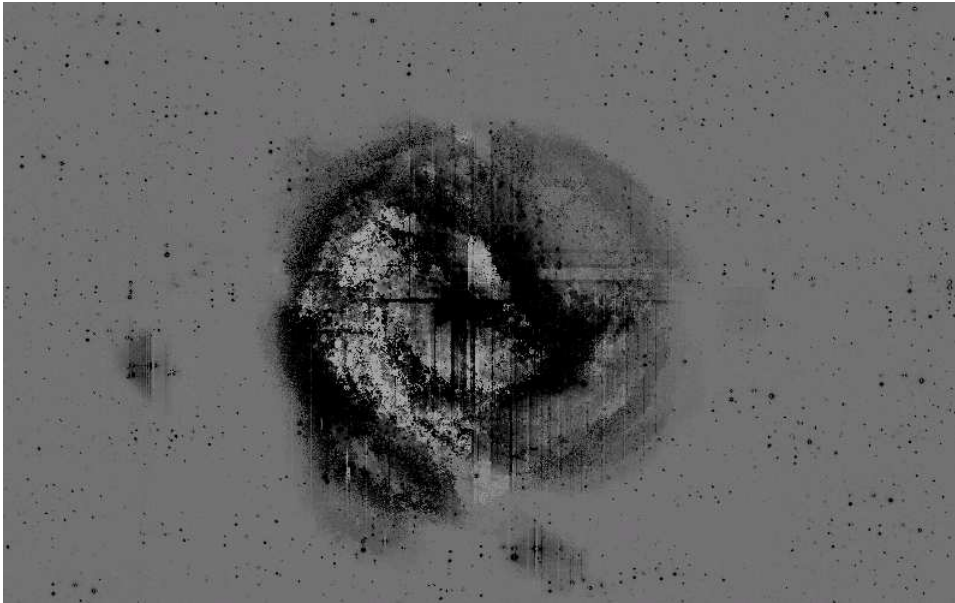


Figure 3.4: Example of an image of M83 in which the astrometry did not work out well. For the majority of stars three reflections are visible.

scale objects. Pixels that belong to such large scale objects were replaced with the image's mode value derived from the image statistics. Then a *SEXTRACTOR* background image, based on the mask-image created before, was subtracted from the original frame. This procedure works well with all kinds of empty fields and can also handle artifacts produced by a few saturated stars. Figure 3.5 shows the result of this procedure in case of the presence of a big galaxy, here M83.

3.4.5 The Sky-Background Procedure

Looking at the figure shows a melee between bright and dark areas inside the galaxy and the absence of stars caused by the smoothing kernel. The breakdown of this method lies in the assumption that in any region there will be enough real background available for local statistics. This is surely not the case in the presence of such large objects, as there is much scattered light present inside the borders of a galaxy. To account for this situation a new background subtracting script was written for the pipeline based on the assumption that the real sky background in each frame is not expected to rise to values above 3σ of its mode value. This mode value is calculated per chip from a large user-defined region where no large objects are present. The new script still uses the automatic *SEXTRACTOR* extraction of smaller objects and it still creates a background image. Only in case of a rise above the 3σ mode all such pixels will be replaced by the modes value. Another new

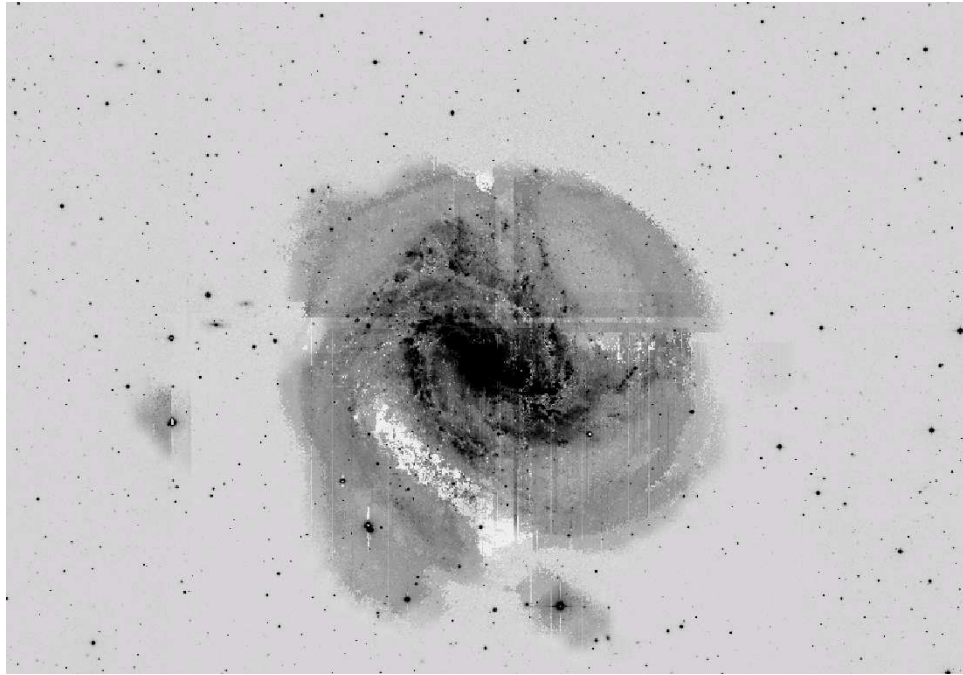


Figure 3.5: Example of an image of M 83 for which the standard sky-subtraction procedure was used. The sky around the galaxy is overestimated in some parts of the galaxy.

script is able to subtract a constant sky value that is also derived by the mode of sky values but the user has to supply an empty region for each chip. Both scripts work fine in the context of the pipeline. For the final data reduction the second script that treats each region the same way by subtracting a constant value was used. The disadvantage of this method is that it cannot correct for small gradients in the sky. But some simple photometric tests for co-added images have shown that the deviation in photometry between both methods is below the 0.02 mag level. The first method could not remove the gradient inside the borders of the galaxy, either, as there is no easy indication for the strength of the sky background compared to the intrinsic variation of surface brightness from the galaxy (e.g. presence of spiral arms). The only way to disentangle this effect would be to include models of surface brightness profiles of face-on galaxies and models for sky background variations. An iterative fitting procedure might then be able to extract the fraction of each effect.

Considering the large extent of the objects observed and the interest in stellar photometry instead of surface photometry, an equal treatment of the whole image instead of trying to reduce a gradient in the sky background outside the galaxy was preferred. Therefore the assumption of a constant sky background is viable.

This said, the last step is then the co-addition of the images. Figures 3.6 and 3.7 show the fully reduced and co-added of M 83 and NGC 7793 in the V-band. The co-addition uses a program called *SWARP* created by Bertin (2002) and it is the replacement for the IRAF *Eis/Drizzle* task formerly used. On the machine used, a 2.2 GHz Intel Xeon machine, it took about 5 to 7 hours for this last step to complete. This also includes the time for rescaling and regridding of each frame. The reduction of such a dataset like NGC 7793 produced about 600 - 750 GB of temporary data.

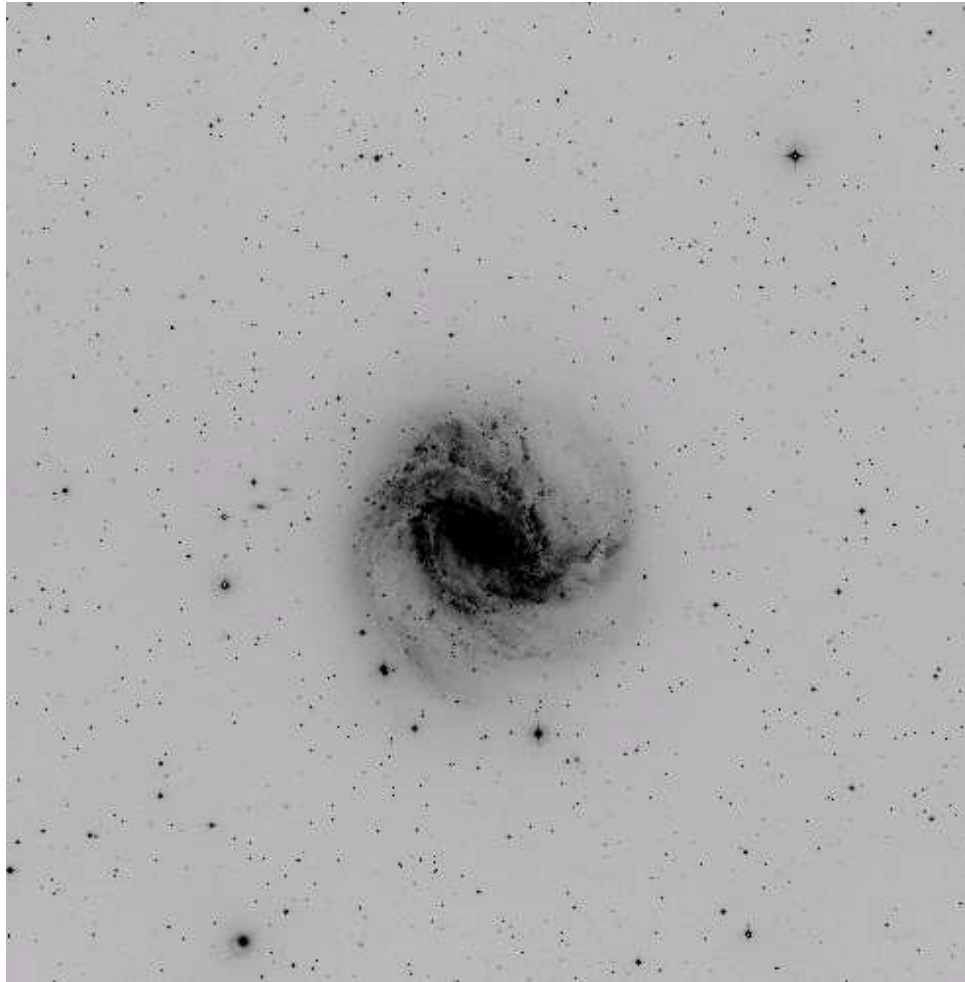


Figure 3.6: Example of a final co-added image of M 83 in the V-band. The maximum variation in the sky-background value outside the galaxy is of the order of 0.05 %.

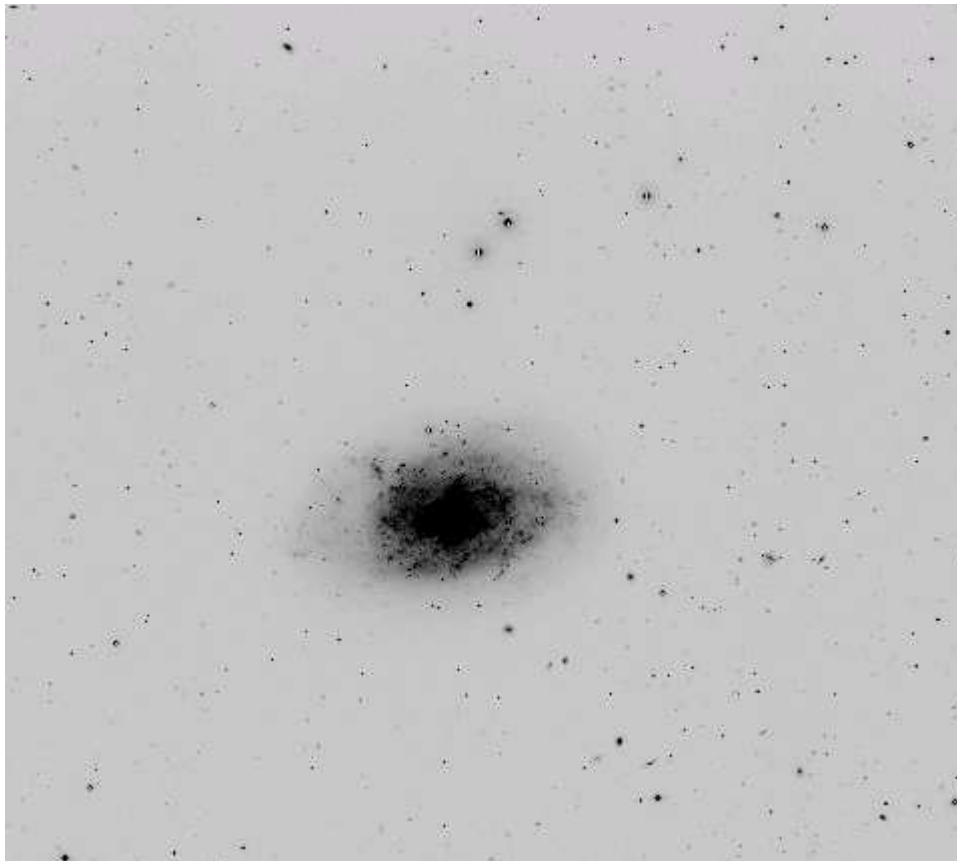


Figure 3.7: Example of a final co-added image of NGC 7793 in the V-band. The maximum variation in the sky-background value outside the galaxy is of the order of 0.06 %.

Chapter 4

Photometry & Calibration

4.1 General Discussion

This chapter will describe the photometry performed to extract stars from an image and the necessary steps to calibrate the achieved stellar brightness measurements to a standard photometric system, the Johnson-Cousins UBVRI system. The photometric calibration is a crucial part which allows one to check the quality of the reduction carried out before. In this case the calibration must deal with the fact that the ESO/MPG WFI is a multi-chip instrument and that there are reports of an illumination problem present in the literature (Koch et al. 2004) that needs to be discussed to address the question of the data quality. However, the fact that such a global transformation is possible shows that the reduction carried out proceeded without creating any large systematic error due to the merging of data from different CCD chips. Using the NGC 300 data was one of the first demonstrations that the photometric quality of the data reduced by the pipeline is excellent up to an error of 0.05 magnitudes.

All photometry was performed using the *DAOPHOT* task (Stetson 1987) implemented in *IRAF*¹ Version 2.12.2. The photometry followed the standard procedures for carrying out aperture photometry at first, followed by point-spread-function (PSF) photometry. Afterwards the transformation will be calculated. For each dataset a different method is used because of the available calibration frames.

4.2 General Photometry Procedure and Issues

Previous to the photometry *DAOFIND* was used to detect possible stellar sources. *DAOFIND* does this by searching for sources which have a higher signal than a

¹see <http://iraf.noao.edu> for more information about IRAF

pre-defined detection threshold. To get a good value for this detection threshold this parameter was varied in the range from 2.5σ to 5σ in steps increasing by 0.2. The optimum value was chosen to be that factor used before a dramatic increase in stellar counts occurs. At this point *DAOFIND* will most likely include many spurious detections in its catalog of possible stellar sources. Having a list of possible stellar sources aperture photometry will be done in order to get the instrumental magnitudes for bright stars that are used to construct the PSF. The basic idea of PSF photometry is to get a stars magnitude by scaling a stars PSF to a general PSF of well-known magnitude which was constructed in advance using well separated and bright stars. The advantages of this method in comparison to the aperture photometry is the possibility of separating overlapping stars and its robustness against single pixel defects or single cosmic ray events inside a stars' profile.

Therefore, well separated stars covering a broad magnitude range were selected. Due to saturation effects that produce broader profiles for very bright stars, these bright stars were excluded from constructing the optimal PSF-profile. The sky background was also recomputed during PSF-fitting using the idea of applying a group sky value² to each group of 60 nearest stars. This method of measuring the sky background has two advantages:

First, it works well in areas where the stellar density rises to the point where stars begin to overlap within the region normally used to calculate the sky. Even if the PSF-photometry was able to subtract the stars, small residues will remain and influence sky values. For a group of stars instead the increase of the point set of possible sky values will lead to better statistics and therefore to a better estimation of the real sky value.

Secondly, increasing the point set for calculating the sky value will also reduce the effects of small scale fluctuations while still retaining the influence of larger gradients in the background caused by the galaxy.

Another problem for WFI-photometry that was reported by Koch et al. (2004) is the illumination due to stray light inside the instrument. They claim that this effect is up to 0.08 magnitudes for stellar photometry on a single CCD chip. A problem that is not discussed by them is the question of time dependence and "baffle" dependence of this effect. Up to now ESO has changed the baffle several times, so simply applying the calibration map is not possible without the chance of introducing a new systematic error. Also not discussed is the possibility of dependence of this effect with the position of the telescope. The flexure of the whole telescope could slightly change the pattern, too. In the next section it will be shown that the effect could not be reproduced in the reported order of magnitude for the data reduced with the *THELI* pipeline. In one case an illumination map

²same sky value for a group of stars instead of individual sky values for each star

was constructed and in the case of the NGC 300 data secondary standard stars present over the whole field of view were used.

4.3 The Wide-Field-Imager Illumination Problem

As it was already mentioned in the previous section, Koch et al. (2004) reported and quantified an illumination problem of the ESO 2.2m Wide Field Imager. In this section this problem will be shortly discussed as well as the effects causing it. A rough estimation on its impact on data processed with the *THELI*-Pipeline will also be given.

It is known that the quality of an astronomical image is limited due to several factors. Naturally, one of these limiting factors are the observing conditions (cloudy sky, atmospheric humidity, seeing etc). Unfortunately, the observer's influence to reduce such problems is going towards zero. Surely, one can measure and log this conditional parameters in order to evaluate the quality of the data after observation. With this it is possible to include such data using an appropriate weighting scheme in final co-added image or simply to discard very bad images. But other limiting factors in regard to the optics and the detector of the instrument still remain.

The detector itself can be one cause for a degraded performance if small scale variations in its sensitivity exist. CCDs, for example are affected by such problems as the quantum efficiency is not constant throughout every pixel present in the detectors array. Such a problem is normally addressed in the data reduction by the use of an appropriate flatfield procedure. In addition this procedure corrects also for the absorption of light due to dust on lenses near the detector. Nevertheless, it cannot correct for effects that are varying during the night or for large scale variations. For the latter effect of large scale variations a super-flat could be used. Here one creates a flat-field image out of (all) the individual science exposures. This is only possible if the amount of science observations and their dithering during an observation run is large enough to account for the size of a star and small objects. But as it is shown by Manfroid & Selman (2001) the illumination effect inside the ESO/MPG WFI is caused mainly by stray light and reflections inside the instrument. Therefore, the science as well as the flatfield exposures are affected by the same effect. The stray light itself is mostly composed of redistributed light of objects inside the FOV and by ghost reflections.

Such reflections and ghost images are a common problem in focal reducers due to the presence of several air-glass surfaces. As it is also done in the ESO/MPG WFI the filter is located in the middle of two lens triplets. Including the dewar entrance window of the CCD and the surface of the detector itself there are nine air-glass surfaces present, enough possibilities for reflections and ghost images

to occur. To minimize these effects suitable anti-reflection coatings are used in the baffle of the instrument. This explains several changes³ to the baffle that have occurred up to now as an effort to minimize this illumination as new coatings were deployed.

To check for the success of these changes a dataset of Palomar 5 observed in August 2003 is used. It contains a faint and sparse globular cluster. This work therefore characterizes the status of the illumination during the presence of baffle no. 3 mounted at the beginning of 2003 and unmounted April 18th, 2004. It should also be pointed out that the work of Koch et al. (2004) also used Palomar 5 data, therefore the results can be compared to this work, too. But the main reason for using this globular cluster is the number of stars present and the spatial extension of it along the sky. So the complete field of view can be checked with a small number of exposures. It is also necessary to have a reference photometry available. In this case this was the photometry of this cluster made with the Sloan Digital Sky Survey.

The data was reduced by Clemens Trachternach following the usual reduction procedures of the *THELI*-pipeline which were described in chapter 3. Because of the missing dithering during the observation this dataset is an ideal test case for measuring the effect of the illumination. Normally, due to the photometric alignment of the individual images the illumination effect might be decreased if stars move along the detectors' position.

In accordance with the procedure described by Koch et al. (2004) the comparison of the photometric results were made with the Sloan Digital Sky Survey, Data-release No. 6 (Adelman-McCarthy 2007). In contrast to me, Koch et al. (2004) used the Early Data Release of Stoughton (2002). Due to the fact that the filter set from Sloan is different (a modified Thuan-Gunn system) from the one used at the ESO/MPG WFI, the Sloan magnitudes were transformed according to the transformation equations of Smith et al. (2002) to the Johnson-Cousins system:

$$B = g' + 0.47 \cdot (g' - r') + 0.17 \quad (4.1)$$

$$V = g' - 0.55 \cdot (g' - r') - 0.03 \quad (4.2)$$

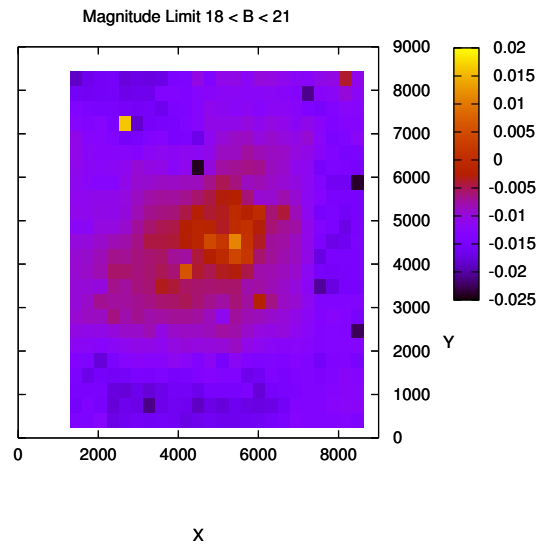
$$V - R = 0.59 \cdot (g' - r') + 0.11 \quad (4.3)$$

Here capital letters describe the Johnson-Cousins magnitude system while apostrophized, lower case letters describe the Sloans Thuan-Gunn system. In doing so a final catalog of stellar detections, their positions, and magnitudes and in the Sloan Digital Sky Survey DR6, ready to be compared to the WFI detections,

³see <http://www.lis.eso.org/lasilla/sciops/2p2/E2p2M/WFI/HistoryOfChanges2p2.html> for a list of changes to the instrument

is obtained. Solely, because the aim in this photometric study was the comparison of magnitudes no automatic starfinder was used on this final WFI image. Instead the positions for the photometry were already given by the Sloan catalog and had only to be recovered in the WFI images. This was done in the same way and with the same scripts that were used for the calibration of NGC 7793 (see also chapter 4.6 for more details). To avoid the influence of imprecise measurements stars not saturated on the WFI image and with magnitude errors below 0.06 mag in both catalogs were used to find a global transformation from the Sloan to the WFI dataset. These boundaries set the limits to stars selected roughly at $18 < m < 21$ in the B- and in the R-band filter. After computation of a global transformation, the residuals between each stars expected magnitude versus Sloan-magnitude was calculated. The final illumination map derived in this way shows the residuals of about 800 stars using a linear interpolation between each datapoint. As it is seen from figure 4.1 the effect has been decreased by more than 50 per cent using the new baffle. While the difference between center and the boundaries was of the order of 0.08 magnitudes in 2001 (baffle no.1), it is now only of the order of about 0.03 magnitudes. This places the effect roughly at the same order of magnitude as the error of standard stars used for the calibration of the data. Considering the aims of this study and the selection boundaries used in creating the star count maps this error is very small in comparison to the maximum accepted photometric error of the order of 0.1 to 0.15 magnitudes.

Illumination map ESO/WFI B-Band



Illumination map ESO/WFI R-Band

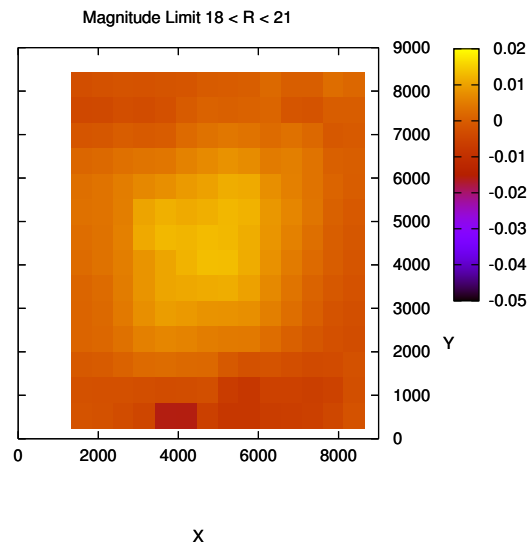


Figure 4.1: Illumination maps for the WFI instrument using baffle no 3. As expected a small gradient caused by stray light and reflections is present and brightens sources in the central area, but this effect is significantly smaller than for baffle 1. Top: B-band map. Bottom: R-band map.

4.4 Photometry and Calibration of NGC 300 Data

The photometry of NGC 300 followed the standard procedure outlined before. The necessary *DAOPHOT* input parameters to reproduce the photometry are given in table 4.1. After PSF-photometry the sources of the three filters were matched to get a complete catalog of sources detected around NGC 300. This catalog contains about 210,000 objects found in all three filters. It is important to note at this point that during the final step of applying the PSF to calculate the magnitude, many objects like galaxies were sorted out if they could not be fitted by the PSF function. This means that a very large fraction of false detections like galaxies, noise or cosmic rays were sorted out during this fitting procedure. Random detections of noise are also sorted out during the cross reference getting the complete catalog.

Although this is an efficient task to reduce the number of non-stellar sources in the final catalog some more distant background galaxies may still remain in it if their shape is star-like. An estimation of how much galaxies are expected in a considered color-magnitude region will be given in the sections describing the analysis.

The next step to transform the instrumental magnitudes to a standard magnitude system was done using secondary photometric standard stars measured by Pietrzyński et al. (2002). All these standard stars are located in NGC 300 and therefore within the area under examination. The complete catalog published contains 390 stars for which B,V and I-band measurements exist. Using the positions and finding charts they presented 107 of these standard stars were taken to calibrate the data. The rest of the stars were discarded either due to their position near to the central region or due to a neighboring star within a radius of 40 pixels. In short, only the most separated stars of the standard catalog are used. The transformation formula, neglecting any airmass dependence, is of the following form:

$$b = B + b_1 \cdot (B - V) + b_2 \quad (4.4)$$

$$v = V + v_1 \cdot (B - V) + v_2 \quad (4.5)$$

In this formula capital letters represent absolute magnitudes and single lower case letters describe instrumental magnitudes. The assumption of neglecting the airmass is valid due to the fact of observing the standards within the field under discussion. Usually, standards and science-fields are different exposures and therefore taken under different airmass conditions. Hence a correction term must be applied to correct for the difference in absorption caused by the different path length of a beam of light. Even using an instrument, like WFI, with a large field of view there is no need to include an airmass term. Over the FOV the airmass can be regarded as constant.

| Parameter | B-band | V-band | R-band |
|--------------|--------------|--------------|--------------|
| fwhm | 4.6 pixels | 4.3 pixels | 4.3 pixels |
| σ | 0.5 pixels | 0.6 pixels | 1.7 pixels |
| datamin | 300 counts | 300 counts | 300 counts |
| datamax | 60000 counts | 60000 counts | 60000 counts |
| psfrad | 12 pixels | 12 pixels | 12 pixels |
| fitrad | 5 pixels | 6 pixels | 5 pixels |
| sky annulus | 15 pixels | 15 pixels | 15 pixels |
| sky dannulus | 9 pixels | 8 pixels | 7 pixels |
| maxgrou | 60 | 60 | 60 |
| threshold | 4 σ | 3.5 σ | 4.5 σ |

Table 4.1: Important photometry parameters as used by IRAF/DAOPHOT for NGC 300

Values for b_x and v_x were retrieved using the *IRAF* routines for photometric calibration in the photcal package. These routines use a Levenberg-Marquardt algorithm to solve these equations and lead to values of $b_1 = -0.2819 \pm 0.0066$, $b_2 = 0.6950 \pm 0.0063$, $v_1 = 0.07810 \pm 0.0050$ and $v_2 = 0.8910 \pm 0.0048$ for a global solution. Global in this sense means that there is no differentiation or weighting for the stars depending on the position on different chips. The only weight applied during fitting is the photometric weight related to the photometric error as it is calculated by *DAOPHOT/ALLSTAR*. Plotting the residuals of this fit (see figure 4.2 as a function of B-band (stars) and V-band (crosses) magnitude shows no significant tendency for residuals to correlate with magnitude. For the global solution the derived standard deviation for σ was $\sigma(B) = 0.0374$ and $\sigma(V) = 0.0288$. So the global solution applied introduces an error of about 0.04 magnitudes and is therefore negligible as it is of the same order as the uncertainties for some of the secondary photometric standards.

To answer the question of the quality of the global solution in consideration of the illumination problems of the instrument the global solution was applied to each chip alone to compare a chip-per-chip σ -value. The results are given in table 4.2. There is no large scatter in the σ values giving rise to the conclusion that there is no systematic variation. If one would apply the calibration map of Koch et al. (2004) one would expect larger deviations from the global solution of chip 1, 4, 5 and 8 (outer parts far away from the center) in comparison to chips 2, 3, 6, 7 (inner central parts). In fact the standard deviation for a single chip differs from the standard deviation of the global solution only by a constant smaller than 0.006.

Finally, the transformation was checked with another study of standard stars in

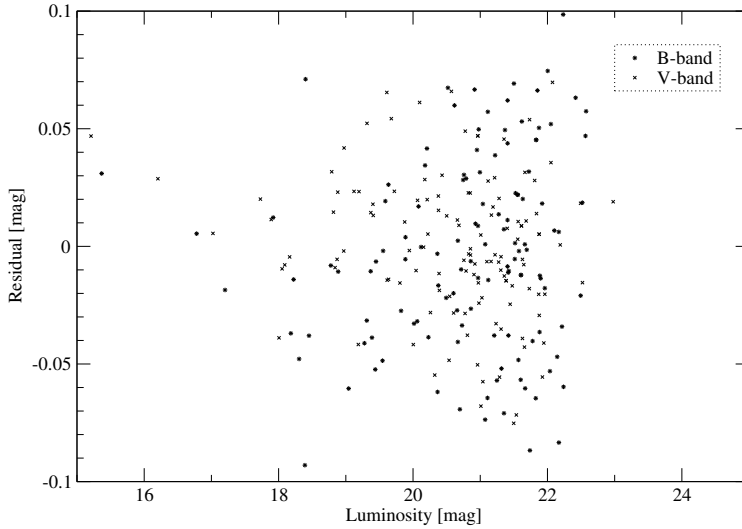


Figure 4.2: Residuals of the standards after applying the global solution for the photometric transformation. Star icons represent B-band magnitudes and cross icons represent V-band magnitudes.

NGC 300 published by Graham (1981). Most of the stars used in this photoelectric study were too bright, and therefore saturated on the CCD-frames. However, for two of them a photometric measurement was possible. The application of the global solution leads to residuals of about 0.06 magnitudes while the photometric errors for these are of the order of 0.05 magnitudes. As a result it can be pointed out that this comparison to the photoelectric study verifies the methods applied for transforming the instrumental system to the standard system.

As a last step the R band transformation has to be applied. Unfortunately, there are no such secondary photometric standards available for this band and there are no corresponding standard star observations of each night available (in contrast to the NGC 7783 case described in paragraph 4.6). Instead of this Freedman et al. (1992) have measured magnitudes of cepheids. Using these cepheids as “new” standard stars and taking for each one its mean magnitude as the standards magnitude, the following equation was solved:

$$r = R + r_1 \cdot (B - R) + r_2 \quad (4.6)$$

Once again lower case letters without indices represent the instrumental magnitudes while upper-case letters describe the standard star magnitude. In this case

| Chip No. | No. of stars | $\sigma(B)$ | $\sigma(V)$ |
|----------|--------------|-------------|-------------|
| 1 | 13 | 0.0349 | 0.0239 |
| 2 | 16 | 0.0396 | 0.0337 |
| 3 | 16 | 0.0394 | 0.0326 |
| 4 | 12 | 0.0401 | 0.0306 |
| 5 | 12 | 0.0320 | 0.0258 |
| 6 | 12 | 0.0357 | 0.0325 |
| 7 | 15 | 0.0392 | 0.0327 |
| 8 | 11 | 0.0394 | 0.0265 |
| 1-8 | 107 | 0.037 | 0.028 |

Table 4.2: Standard deviation of the global solution applied to each chip

for the R-band this is the afore mentioned average magnitude of the cepheids while for the B-band the corresponding magnitude could be calculated using the global solution. Using variables as standard candles will naturally introduce a systematic error in the transformation but due to the fact that the image used for analysis is a co-added frame of several observational runs this can be handled. The co-addition of the frames will average over the flux received from a star. Considering this, the systematical error introduced should not be larger than the standard deviation which is calculated using the measured magnitudes and its mean value. Using the cepheids in question this leads to an additional systematic error smaller than 0.3 magnitudes for the transformation applied. Further in the sight of the analysis that will be carried out, an absolute accurate value is not necessary because the photometry is used mainly to characterize a star's position in the CMD. For this a rough estimate accurate to 0.3 magnitudes is still fine and can be accounted for in the selection criteria (see also chapter 5.3.1). Finally, for r_1 this yields to 0.39 ± 0.11 and $r_2 = 0.0826369 \pm 0.04478705$ with a σ of 0.13. Taking all these errors into account the error in the R-magnitude may be of the order of 0.33 magnitudes for a star with $(B-R) = 1$.

4.5 Photometry and Calibration of M 83 Data

The photometry of M 83 followed the usual procedure. After *DAOFIND* to detect stars, *DAOPHOT* is used for aperture photometry and finally the PSF-photometry part is performed using *ALLSTAR*. The important parameters were set as described in table 4.3. The final catalog consists of about 35,000 objects found in all three filters. This low number of stars is a result of the short exposure time of the

M 83 data available. In comparison to NGC 300 this is a factor of 10 smaller (see also tables 3.1 and 3.2) and the galaxy is about a factor of two more distant than NGC 300. Therefore, it is clear at this point that this study can only detect the most luminous objects of M 83. As a result of this low number of stars the way of computing the sky value was changed. Instead of using a group sky value the sky is now calculated for each star individually. This may cause slightly larger errors in the central parts due to overlapping stars but avoids large errors in the outer parts where the stellar density is too low to form reasonable groups.

| Parameter | B-band | V-band | R-band |
|--------------|--------------|--------------|--------------|
| fwhm | 4.0 pixels | 3.6 pixels | 4.7 pixels |
| σ | 0.5 pixels | 0.45 pixels | 1.5 pixels |
| datamin | 5000 counts | 5000 counts | 3000 counts |
| datamax | 60000 counts | 60000 counts | 60000 counts |
| psfrad | 12 pixels | 14 pixels | 14 pixels |
| fitrad | 9 pixels | 7 pixels | 7 pixels |
| sky annulus | 12 pixels | 15 pixels | 15 pixels |
| sky dannulus | 4 pixels | 4 pixels | 4 pixels |
| threshold | 3.4 σ | 3.4 σ | 3.2 σ |

Table 4.3: Important photometry parameters for the M 83 data as used by IRAF/DAOPHOT

The transformation of the M 83 stars was done using a photoelectric sequence published by Zickgraf et al. (1990). This sequence includes 28 stars while for the transformation 22 of them were used. The remaining 6 stars were saturated and were therefore excluded from further calculations. As the situation for the transformation was nearly the same as for the NGC 300 data in the sense that the stars were present inside the co-added science frame, the same equations that were already given above (equations 4.5 and 4.8) were used. The results of these are given in table 4.4. The derived values transformed the instrumental magnitudes to the standard Johnson-Cousins UBVRI system. After applying this transformation it became clear that the photometry only reaches down to about 24.5 magnitudes in B with a photometric error already of 0.4 magnitudes.

4.6 Photometry and Calibration of NGC 7793 Data

The photometry of the NGC 7793 data was carried out using the same *DAOFIND*, *DAOPHOT* and *ALLSTAR* procedures than before. The input parameters were set according to the values described in table 4.5. For this data a catalog of B123/V

| Parameter | Value | error | σ_x |
|-----------|-------|-------|------------|
| b_1 | -0.21 | 0.03 | 0.04 |
| b_2 | -0.03 | 0.03 | 0.04 |
| v_1 | -0.31 | 0.06 | 0.05 |
| v_2 | 0.56 | 0.03 | 0.05 |
| r_1 | -0.03 | 0.02 | 0.03 |
| r_2 | 1.22 | 0.02 | 0.03 |

Table 4.4: Results of the M 83 transformation to the Standard

magnitudes with about 88,000 objects and a B-new catalog consisting of about 93,000 objects were created.

| Parameter | B123-band | Bnew-band | V-band |
|--------------|---------------|---------------|--------------|
| fwhm | 3.7 pixels | 4.5 pixels | 4.25 pixels |
| σ | 0.95 pixels | 1.1 pixels | 0.9 pixels |
| datamin | 3000 counts | 3000 counts | 3000 counts |
| datamax | 310000 counts | 310000 counts | 60000 counts |
| psfrad | 10 pixels | 12 pixels | 12 pixels |
| fitrad | 5 pixels | 5 pixels | 5 pixels |
| sky annulus | 12 pixels | 12 pixels | 12 pixels |
| sky dannulus | 4 pixels | 11 pixels | 5 pixels |
| threshold | 3.0σ | 2.9σ | 3.0σ |

Table 4.5: Important photometry parameters for the NGC 7793 data as used by IRAF/DAOPHOT

A big difference compared to the other datasets was made for transforming the instrumental magnitudes to the standard system. To my knowledge now sufficient photometric sequence of standard stars exist inside the field of NGC 7793 rendering the approach used until now for the calibration unfeasible. But for nearly all observational runs a sufficient number of Landolt standard stars (Landolt 1992) exposures exist. A transformation of each night to a standard system is possible. The problem that had to be solved was the automatic extraction of all these standard stars from the different exposures and to convert the extracted values to a format utilizable in the tasks in the *IRAF/PHOTCAL* package. To achieve this different bash-scripts were written that partition the necessary procedure to single, smaller steps.

In the first step the images are separated according to their position recorded in the fits header keywords. Subsequently on each set *ASTROMETRIX* is used

to astrometrically calibrate each single frame in order to get an accurate world-coordinate system. This is done because the x,y position of the Landolt standard stars is unknown and due to the large number of frames it would be a tedious task to identify them manually using appropriate finding charts. Instead of this it was decided to use the known catalog positions in Right Ascension and Declination and to transform them into x,y coordinates. This was carried out by a script that uses the *IRAF/SKYXYMATCH* task. Now each image has its own catalog of standard stars to be extracted. The photometry was then performed using the *DAOPHOT* task to derive the list of instrumental magnitudes. Given that *DAOPHOT* also includes some quality control in the sense that it detects centering errors, photometry errors and sky fitting errors, these flags are used to select only those where everything went well without errors. A self-written Fortran program works afterwards on this list to prepare it for further calculations. The program is intended to search for multiple observations of the same star and calculates an average magnitude for all multiple observations. This is done because it is possible that some exposures are bad due to changing sky conditions, e.g. the exposure was taken too late or too early so that dusk or dawn is affecting it. To minimize such effects the program will iteratively calculate the average magnitude and reject values that are 3σ below or above. Then this final list of stars will be used to solve the following transformation equations:

$$b = B + b_1 \cdot (B - V) + b_2 \cdot Am + b_3 \quad (4.7)$$

$$v = V + v_1 \cdot (B - V) + v_2 \cdot Am + v_3 \quad (4.8)$$

The nomenclature of the symbols is again of a form where lower-case letters represent the instrumental magnitudes and upper-case letters represent the standard star magnitudes. This time the standard star magnitudes are the Landolt magnitudes (Landolt 1992) and Am is the value of the airmass based on position of the telescope. For each night the final results of the coefficients are given in tables 4.6, 4.7 and 4.8.

| Date of obs. | b_1 | error b_1 | b_2 | error b_2 | b_3 | error b_3 | σ |
|--------------|-------|-------------|-------|-------------|--------|-------------|----------|
| 06/07/2002 | 0.22 | - | -0.25 | - | 0.2334 | 0.0101 | 0.0792 |
| 09/08/2002 | 0.22 | - | -0.25 | - | 0.2438 | 0.0097 | 0.0701 |
| 27/09/2002 | 0.22 | - | -0.25 | - | 0.2045 | 0.0110 | 0.0808 |

Table 4.6: Calibration results for each night in the B-band. No error given for a coefficient means that this is a default value obtained by seasonal ESO measurements.

| Date of obs. | b_1 | error b_1 | b_2 | error b_2 | b_3 | error b_3 | σ |
|--------------|-------|-------------|---------|-------------|--------|-------------|----------|
| 10/10/2002 | 0.22 | - | -0.2312 | 0.0266 | 0.2110 | 0.0219 | 0.0366 |
| 26/10/2002 | 0.22 | - | -0.25 | - | 0.2296 | 0.0930 | 0.0660 |
| 29/07/2003 | 0.21 | - | -0.26 | - | 0.1540 | 0.0088 | 0.0522 |
| 25/09/2003 | 0.19 | - | -0.2356 | 0.0178 | 0.2259 | 0.0201 | 0.0455 |

Table 4.7: Calibration results for each night in the B-band (B-new) filter. No error given for any coefficient means that this is a default value obtained by seasonal ESO measurements.

| Date of obs. | v_1 | error v_1 | v_2 | error v_2 | v_3 | error v_3 | σ |
|--------------|-------|-------------|--------|-------------|--------|-------------|----------|
| 06/07/2002 | 0.11 | - | 0.0860 | 0.0192 | 0.8381 | 0.0166 | 0.0620 |
| 09/08/2002 | 0.11 | - | 0.13 | - | 0.8395 | 0.0089 | 0.0644 |
| 27/09/2002 | 0.11 | - | 0.13 | - | 0.7709 | 0.0082 | 0.0543 |
| 10/10/2002 | - | - | - | - | - | - | - |
| 26/10/2002 | 0.11 | - | 0.13 | - | 0.8376 | 0.0088 | 0.0502 |
| 11/12/2002 | - | - | - | - | - | - | - |
| 29/07/2003 | 0.10 | - | 0.1083 | 0.0209 | 0.7692 | 0.0208 | 0.0507 |
| 02/08/2003 | - | - | - | - | - | - | - |
| 25/09/2003 | 0.19 | - | 0.1401 | 0.0289 | 0.6689 | 0.0329 | 0.0456 |
| 04/10/2003 | 0.19 | - | 0.1780 | 0.0650 | 0.7036 | 0.0556 | 0.0864 |
| 18/10/2003 | 0.19 | - | 0.13 | - | 0.6478 | 0.0140 | 0.0797 |

Table 4.8: Calibration results for each night in the V-band filter. No error given for any coefficient means that this is a default value obtained by seasonal ESO measurements.

Methods of Data Analysis

5.1 General Discussion

In this chapter the main methods of analyzing various data sets of different galaxies will be presented. Questions of why stellar counts are used and how to get corresponding stellar count maps by the help of isochrones will be addressed in detail. Additionally, the use of the *KNIME*-framework used for the data-mining part of this analysis will be described. The chapter will end with a discussion and comparison of both methods.

5.2 Color-Magnitude-Diagram

Using the results of stellar photometry to construct the color-magnitude diagrams (see 4.2 for a discussion of the photometry itself) the next step is to analyze these diagrams by searching for interesting features resembling streams or truncations. For a galaxy one should be able to see several different and interesting features like the main sequence (MS), the subgiant branch (SGB), the red giant branch (RGB), the red clump (RC), the asymptotic giant branch (AGB) etc. These structures and their shape or peculiarity are important because they characterize a galaxy and its formation history. This is due to the fact that the location of a star in a color-magnitude diagram depends mainly on its initial parameters (mass and chemical composition at its birth) and on its evolutionary state or age. Considering the distance to the galaxies investigated in this work and the types of stars visible one might make the assumption, that blue stars are mainly part of a young stellar population, namely the massive blue stars on the main sequence, while red stars, mostly giant or supergiant stars, describe the older stellar population. A population is characterized best by a set of isochrones, which show the position

of stars of the same age in a color magnitude diagram. Isochrones are based on theoretical calculations of stellar structure and evolution and might therefore provide a first rough estimate of the ages of the dominant observed stellar population. Different approaches are used to calculate the isochrones and depending on the physical models (i.e. alpha-enhancement, overshooting etc.) used to describe the stellar evolution isochrones of same age and metallicity might vary. Throughout this work the Padova-Isochrones calculated by Girardi et al. (2002) will be used. According values for the distance modulus and extinction have to be applied for each galaxy in question. An example of such an isochrone set is given in figure 5.1.

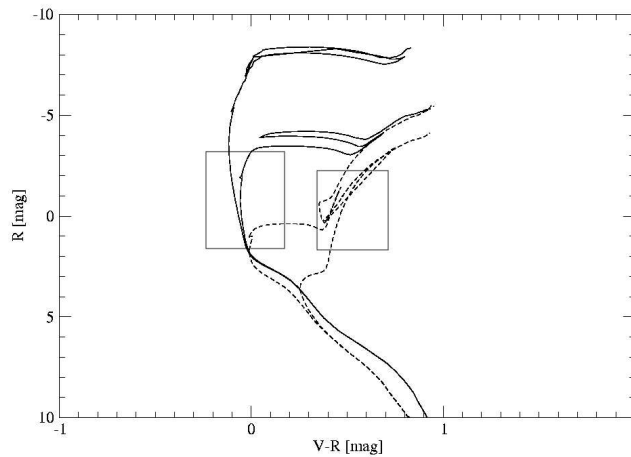


Figure 5.1: An example of four different isochrones calculated by Girardi et al. (2002). The dashed lines correspond to isochrones with a metallicity of $z=0.001$ and are of 10 and 1 Gyr in age. The continuous lines are for metallicity $z=0.008$ and ages of 10 and 100 Myr. The boxes show typical areas used for creating star count maps according to the isochrones.

Although it is also possible to derive information about the structure of galaxies from surface photometry (de Vaucouleurs & Capaccioli 1979), where the integrated light of several stars is used, in this work the method of using star counts is favored. Surface photometry is limited by the brightness of the night sky that has to be subtracted. Night sky subtraction is a difficult task especially in multi-chip, wide field image exposures where additional illumination effects have to be taken into account. In this work the data used was taken mainly with the ESO 2.2m Wide Field Imager (WFI) at La Silla in Chile. For this instrument an article was published in 2004 by Koch et al. (2004) that shows a calibration map for

the smoothly, varying large-scale gradient caused by in-falling stray light. This additional light, they claim, cannot be removed by using standard flatfield procedures. Though such a calibration map in principle exists to correct for this effect the problem with this map is that it cannot be used for this data because of several reasons:

As already discussed in chapter 3 the *THELI*-Pipeline was used to reduce and to co-add this data. In the case of NGC 300 it was tried to reproduce the findings of Koch et al. (2004) but although using several secondary photometric standards published by Pietrzyński et al. (2002) this was not able to reproduce a significant variation in stellar magnitudes. This may be a result of the fact that the photometric accuracy is of the same order as the effect of the illumination. It may as well be due to the reduction process itself. In its final stage the *THELI* pipeline uses a photometric weighting during its co-addition process that could partially smear out the effects of the illumination. Due to the dithering pattern used during observation a star's position on each frame varies between different exposures. As the aim of such dithering is to get enough data to avoid gaps between the individual CCD-chips, some stars may also change the CCD on which they are detected. This could finally result in a further reduction of the illumination effects in stellar photometry due to the statistical nature of the co-addition process.

Another point to keep in mind is that ESO has tried to reduce the illumination problem several times by changing the configuration and replacing the baffles. The last baffle number five was mounted on 16th March 2005, so since the official start of the WFI there have been five major changes and numerous minor modifications¹ to the instrument of which everyone changed the illumination pattern inside the instrument. The calibration maps provided by Koch et al. (2004) are only valid during a short period of time while the raw data reduced for this work was always taken over a period of several months or years. This statement is also supported by the findings as presented in chapter 4.3. Here it was shown that this effect has been successfully decreased after the installation of baffle no. 3. Therefore, this may also be another reason for not seeing the illumination effect in the photometric standards during calibration. A varying illumination due to baffle changes will greatly influence the statistics during the co-addition in a way that minimizes its systematic effects. Still, a correction using such maps is very difficult without having enough sufficient data available for each installation of the instrument.

In addition to the illumination problems surface photometry is in general also affected by errors in the flat field (Pohlen et al. 2002), the diffuse Galactic light and zodiacal light (Bernstein et al. 2002) which arise if one tries going down to

¹A short description of all changes made to WFI is listed at <http://www.ls.eso.org/lasilla/sciops/2p2/E2p2M/WFI/HistoryOfChanges2p2.html>

fainter magnitudes than $\mu_R \sim 27$ mag arcseconds⁻².

Considering the problems and drawbacks of the surface photometry especially under the consideration of the data at hand the conclusion is that the WFI data is not very well suited for an analysis by surface photometry in a case where the primary interest lies in the faintest structures of a galaxy. Instead of surface photometry the stellar photometry is a better suited possibility for the scientific objective at hand. Here a local varying background is still not desired but it is also not too bad, as one has the possibility to measure a star's brightness in contrast to a confined and local background. Using stellar photometry and color-magnitude diagrams it is an easy step to find structures by using the detection of faint star counts. As Pritchett & van den Bergh (1994) showed for their analysis of M31 it is possible to reach an equivalent of $\mu_V \sim 30$ mag arcseconds² by using stars near the tip of the red giant branch without dealing with the problems of surface photometry.

5.3 Methods

5.3.1 Preselection Using Isochrones

In order to search for substructure it is necessary to define what has to be expected and which region of the CMD will help to answer this question. In this work a method similar to that introduced by Ferguson & Johnson (2001) is used. The CMD will be subdivided into different regions of interest. To do so the use of isochrones like the ones shown in figure 5.1 is necessary. For the analysis an appropriate distance modulus and an extinction correction has to be applied for each galaxy. The distance is determined from the period-luminosity relation of cepheids and the extinction values are derived from the extinction maps of Schlegel et al. (1998). This also means that it was not corrected for internal extinction internal to the galaxy in question. Since this study focuses on the outskirts of the galaxy the internal extinction is negligible. In most cases such an internal extinction will introduce an error which is small compared to photometric errors of the order of 0.1 - 0.2 magnitudes in these outskirts. The face-on or near face-on view of all of the galaxies in question also reduces the impact of internal extinction. Any star, even if it is on the other side of the disk, is not seen through a very large volume of intergalactic gas and dust. This changes dramatically for an edge-on view as the height of a galactic disk is small in comparison to the size of its plane.

For further analysis two main regions encircled by corresponding isochrones are of interest. A "blue" region of young stars and a "red" region of very luminous, old stars. The main reasons for choosing these two regions is that on the one hand

the two regions should be prominent (high number of star counts) in each galaxy in order to achieve a high “signal” and on the other hand they will mostly be populated by stars belonging to the galaxy in question, therefore minimizing the influence of foreground and background stars/objects.

The stars in the “blue” region consist mainly of very young and very luminous massive stars on the main sequence (mass-luminosity relation). They are characterized by isochrones of higher metallicity (minimum $z \geq 0.008$) and an age of several hundreds of Myrs. As their lifetime on the main sequence is very short most of these stars must lie in regions of star formation (e.g. HII-regions) or very near to them. In a spiral galaxy such stars may be found in spiral arms or in interacting regions in which star formation was induced not long ago. This may either be an important sign for an ongoing or just completed merging/interaction event or for a region with high gas accretion. In short, such regions may be called active regions and they are typically visible in $H\alpha$ and UV observations.

The stars in the “red” region are mainly of older and very old but luminous stars on the red giant branch. The oldest stars started out as long lived lower-mass main sequence stars that are now in the state of a supergiant. To find them in the CMD diagram isochrones of lower metallicity ($z \leq 0.004$) and ages ranging from 1 to 10 Gyrs are used. Ideally this region should begin at the tip of the red giant branch and extend three magnitudes below it in order to get a large number of stars which are most likely members of the galaxy in question.

Any region selected must also take into account the photometric errors in the corresponding magnitude range. For these reasons the selection box will always be a bit larger (about 0.2 - 0.3 mag in each direction) than suggested by the isochrones representing the group. The star count map itself is then a representation of stellar density in a pre-defined reticule. These maps can then be searched for conspicuous overdensities in the outskirts of a galaxy.

A feature seen in every star count map, is a decrease of the number of stars in the central region of a galaxy. The reason for this is not a physical one in the sense of a decreasing number of stars towards the galactic center. Quite the contrary is true. With an increasing stellar density the photometric tools cannot separate single stars any more and as a result they discard such detections as non-stellar sources (see 4.2 for a detailed description of the photometry). In figure 5.2 two examples of different star count maps are shown for NGC 300. This time no pre-selection has been performed so that this is a representation of the distribution of all stellar sources detected. The only difference between these images is the respective binning area. Such variation in the binning size helps to sort out false detections of overdensities that are caused only by the positioning of the binning reticule.

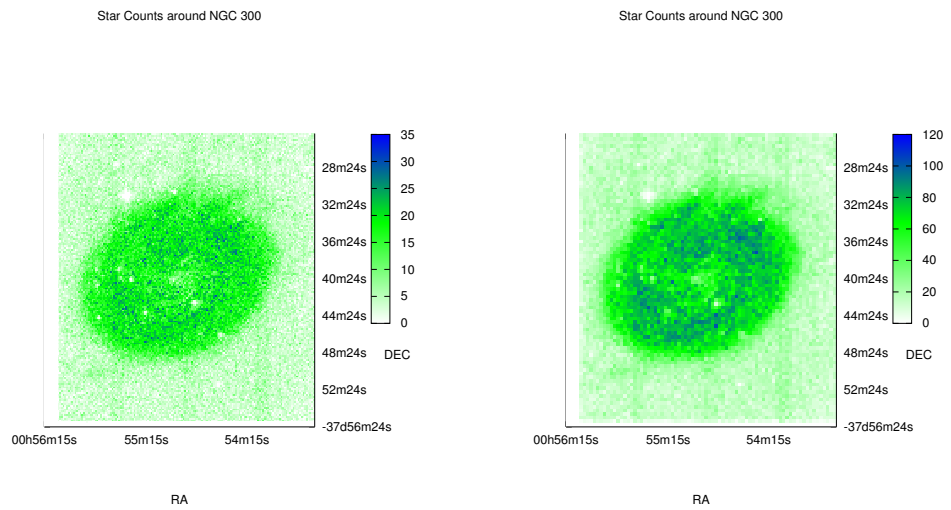


Figure 5.2: An example of two star count maps differing only in the binning area used. There was no preselection done for the stars, so they show the distribution of stars over the complete field of view. The right image uses a binning size of 11.9 arcseconds and the left one uses 23.8 arcseconds in both directions.

5.3.2 Data-Mining

Data-Mining in General

Before beginning to describe and discuss the data mining technique used to find overdensities which might resemble tidal streams it should be clarified what is meant by the term “data-mining” throughout this work. The first question might be if there is a difference between data-mining and statistics. One should keep in mind that statistics is mainly linked to the data, the counting of data and probability. Statistics try to answer questions of what patterns are seen in the data and which are the chances that a chosen pattern will occur. In today’s work statistics are used to summarize data and to predict trends. Histograms are good examples for this summarization technique. In it one sees maximum and minimum values, can estimate (by eye) or calculate mean, median or mode values and also the variance. The power of prediction in statistics is well described by regression techniques. The simplest form of this is, of course, the linear regression which yields the solution that minimizes the total distance to a set of data.

This said one now has to clarify where the data-mining sets in. As in this work the technique used is called “clustering” it will only concentrate on this topic. Other techniques like decision trees, neural networks, or bayesian methods will not be discussed here.

The main idea of clustering is to group similar data objects together. The similarity of objects must be defined by the user and in principle an n-dimensional space is used. In case of numerical attributes spanning up the vector space, the similarity may be measured by a distance value that is calculated using a pre-defined formula. This formula includes the weighting applied to the individual attributes and may also be adopted to the problem or an expected form of the clusters. But in some cases attributes may also be non numerical. Then if one or more attributes are non numerical special rules have to be applied in order to deal with the similarity measurements. For example, it could be determined that this non-numerical attribute must not change within a cluster.

When applying clustering to a dataset an important distinction has to be made in using a so-called “supervised” or “unsupervised” learning technique. For the creation of an “unsupervised” clustering it means that there is no particular reason for the selection of the model clusters. There is no a priori definition of how a cluster is to be defined. The algorithm itself groups the objects together in a sense to maximize similarity. Using a supervised method means that the modeling is performed in a pre-defined way using prototype clusters. Such clusters are organized in groups to answer a particular question. They must have something in common that could be defined by using an adapted space and a calculated distance. The membership of an object will be based on the distance to a cluster’s center. The

cluster's center however is pre-defined by a particular question or model or by the result of a previous run of an "unsupervised" learning technique. A "supervised" learning technique requires some knowledge of the data or of the result in advance. The clustering here is mostly used to verify the a priori knowledge, to fine-tune the answer or to search for something already known in a given data set.

To summarize this, clustering gives a high level view of a data-set either in the way of showing interesting patterns that stand out or of presenting a ranking of pre-defined groups. This task will be carried out using either the hierarchical or the non-hierarchical approach.

In the hierarchical approach a hierarchy of clusters is created. This may be achieved by using agglomerative clustering (bottom-up) in which similar one-point clusters are merged into a new super-cluster until the desired number of clusters is produced. Or it can be done the other way round with a divisive (top-down) approach in which one starts with a single cluster from which appropriate subclusters are split off until the desired number of clusters is reached. Instead of using a pre-defined number of clusters one can also define other stopping criteria like a number of members in each cluster or reaching a specific value for the inter-cluster variation. The problem with hierarchical clustering is that for large data-sets it can be very time-consuming to calculate which points to merge or which to split off. The non-hierarchical approaches do not try to create a hierarchy between the clusters. Instead they try to relocate cluster centers using some form of iterative optimization. The k-medoids and the k-means methods are representatives of this class. The difference between these two methods lies in the handling of the center representing the cluster. In k-medoids the cluster is represented by one of its points, while in k-means the values are represented by the average of its points. Due to its nature of calculating mean-values this method is only suitable for data sets containing numerical values but it is a simple and straightforward method to analyze the data.

Considering the problem at hand, namely the search for tidal streams, the following requirements may be formulated:

- the algorithm has to find patterns corresponding to an overdensity in stellar counts above an underlying background
- the corresponding stars should populate the same (small) region in a color-magnitude diagram and they must be located near each other
- in its center the overdensity might be described as elliptical or circular
- the dataset is large

The first two statements are in good agreement with the purpose of data mining and clustering in general, as they describe the search for a similar pattern. Further-

more it is required that such an overdensity is connected spatially and physically by the position in the color-magnitude diagram. Two spatial coordinates and two luminosities may span up a 4-dimensional vector space in which a distance can be defined. This distance will be used to measure the similarity between two stars and allows the creation of clusters. The large dimension of the dataset (large number of stars) may favor using a non hierarchical approach to the problem in order to save computing time. The only disadvantage here is that the number of resulting clusters is unknown. But this problem will be addressed after a detailed description of the algorithms and implementation used in this work.

K-Means Algorithm

To understand the basic idea of the k-means approach the algorithm itself will be introduced shortly. It is one of the oldest and simplest unsupervised learning algorithms to solve the cluster problem and was e.g. described by MacQueen (1967). The basic idea of this algorithm is to define the membership of the points by assigning each one to its nearest center. The center itself will be defined as being the arithmetic mean of all points belonging to a cluster.

In detail, first a number of k centers will be chosen randomly, where k is the pre-defined number of clusters that must be given by the user. In the next step the distance between each point x_i and the cluster centers z_i will be calculated. Using this distance value each point x_i will be assigned to the nearest center. Having now points belonging to each cluster a new center must be calculated using the following formula:

$$z_i = \sum_{l=1}^{|C_i|} \frac{1}{|C_i|} x_l^i \quad (5.1)$$

where $|C_i|$ represents the points belonging to cluster i . For each cluster C_i a cost $K(C_i)$ will be defined using a sum of squares criteria:

$$K(C_i) = \sum_{l=1}^{|C_i|} (d(z_i, x_l^i))^2 \quad (5.2)$$

where $d(z_i, x_k^i)$ represents a function to measure the distance of the x -th point to its cluster center.

Then the iteration begins with reassigning the membership of points to a cluster, calculating new centers and the costs of the clusters. The iteration might stop if there is no significant change in the costs for the $TK(C_i)$

$$TK(C) = \sum_{m=1}^k K(C_m) \quad (5.3)$$

Alternatively one can write by combining the last two equations:

$$TK(C) = \sum_{m=1}^k \sum_{l=1}^C (d(z_m, x_l^m))^2 \quad (5.4)$$

which gives the objective function that will be minimized by a k-means.

From this description some disadvantages of a simple k-means clustering immediately appear. K-means clustering assigns each point to a cluster. This means that there is no room for noise in the data. Every single point is a valuable cluster member even if the next cluster center is far away. Furthermore k-means depends on an arbitrarily chosen starting point and does not try to find a global minimum. That is to say that the algorithm might stop even if there exists another solution with a lower $TK(C)$. Consequently, different runs of k-means clustering may produce different results, but this disadvantage could be easily reduced by running the k-means several times and choosing the best clustering run where $TK(C)$ is minimal.

This does not guarantee that this is the best clustering solution possible, but the variation of $TK(C)$ shows the dependence of the clustering towards the starting point. Normally, in a large dataset this tends to be small. Due to the nature that each point is assigned to a single cluster one must not mix clusters of different runs. This would invalidate the initial assumption of k-means and all subsequent calculations. Therefore a cluster and its properties are only valid within their corresponding run.

Fuzzy C-Means Algorithm

The fuzzy c-means clustering algorithm, developed by Dunn (1973) introduces the concept of a point belonging to more than one cluster. Based on minimizing the same objective function than for the k-means algorithm an additional u_{ml}^r with r being any real number that satisfies $1 \leq r \leq \infty$ is introduced:

$$TK(C) = \sum_{m=1}^k \sum_{l=1}^C u_{ml}^r (d(z_m, x_l))^2 \quad (5.5)$$

Here u_{ml}^r describes the degree of membership of a point x_l to cluster m and is defined by the following equation:

$$u_{ml} = \frac{1}{\sum_{k=1}^C \left(\frac{d(x_m, z_l)}{d(x_m, z_k)} \right)^{\frac{2}{r-1}}} \quad (5.6)$$

For each point x_m this formula takes into account the distance d to the other cluster centers and r describes the overlap regions of the clusters also called the

“fuzziness” of the clusters. In the k-means approach this “fuzziness” would be set to 1 and this describes a situation where clusters have an abrupt ending, a well defined boundary. As a consequence higher values of r will “un-sharpen” these boundaries of the clusters and increase the overlapping region between neighboring clusters. Obviously, the calculation of a cluster center must also include the membership. This is done using:

$$z_l = \frac{\sum_{l=1}^N u_{ml}^r x_l}{\sum_{l=1}^N u_{ml}^r} \quad (5.7)$$

In analogy to the k-means k random starting points are initialized at startup. Having these points available the memberships u_{ml} are calculated. Use of these newly calculated memberships enables the algorithm to compute new centers for each cluster. The iteration will therefore be made by recalculating centers and membership values until a certain stopping criteria is reached. Such a criteria could be that the matrices follow:

$$\max_{lm} \{|u_{lm}^k - u_{lm}^{k+1}|\} \leq \Delta \quad (5.8)$$

where Δ characterizes the termination and must be between 0 and 1 as any u_{lm} cannot be larger than 1 per definition.

Clustering Assumptions And Limitations

Using clustering algorithms one must also be aware of some limitations of this method. One very obvious limitation is the number of clusters that has to be chosen in advance. Although in reality the number of clusters is generally not known a priori the clustering algorithm implies k to be a known quantity. To get the real number of clusters the simplest way to deal with this is to perform the clustering over a wide range of k . Then each clustering solution can be examined and one may validate if using a higher k is necessary. In the case at hand one might conclude that a robust measure of k is given if there is a small number of clusters comprising few data points, i.e. 9 stars. This number was chosen on calculations, i.e. made with *GALAXYCOUNT* written by Ellis & Bland-Hawthorn (2006) and using the “Besancon-Model” (Robin et al. 2003) for MW foreground stars. Because the influence of background galaxies resembling stellar profiles cannot be excluded in the data, a cluster would be worthless for this study if the possibility exists that it could solely consist of background galaxies. Therefore a calculation is carried out in order to estimate the number of such background sources that are likely to occur in a 120 sq. arcseconds field, a typical extension for such a cluster field (equivalent to a 500 pixel binning of WFI images). Considering a limiting magnitude of 26 in B this results in 2 ± 1 objects and considering also

a limiting magnitude of 26 in R this results in 4 ± 2 objects. An estimation of the number of foreground objects which would be stars of the MW can be made using the ‘‘Besancon-Model’’ of stellar population synthesis (Robin et al. 2003). Using typical values for the interesting regions used in the star count maps the number of foreground stars is negligible in the blue (smaller than 0.1 in a 500 pixel binning interval). In the region of the RGB stars instead it might be as large as 3 stars for such a 500x500 pixel binning interval. Hence to get on the safe side, as two magnitudes are used in the clustering run, real clusters in the sense of tidal streams should have at least 9 members.

Another very important limitation of clustering algorithms is that they tend to be influenced by noise. This limitation however could be addressed by the inclusion of a noise cluster as it was proposed by Dave (1991). The noise cluster is per definition a cluster which collects all points too far away from the rest of the clusters. Therefore the inclusion of a noise cluster allows one to specify a new parameter δ that represents the distance of each cluster from the noise cluster. With this the afore calculated $TK(C)$ becomes:

$$TK(C) = \sum_{m=1}^k \sum_{l=1}^C u_{ml}^r (d(z_m, x_l))^2 + \delta^2 \sum_{l=1}^C \left\{ 1 - \sum_{m=1}^k u_{ml} \right\}^r \quad (5.9)$$

These formula can be minimized under the constraint that for any data-point l the sum of the values representing the membership (u_{ml}) to each of the k clusters must be lower or equal to 1:

$$\forall \sum_{m=1}^k u_{ml} \leq 1 \quad (5.10)$$

A test run will be discussed in the next section. Finally another limitation may come from the shape of the clusters itself. In this work it is assumed that the tidal tails itself should be spherically symmetric. This is obviously not the case for the whole tail as simulations like Choi et al. (2007) have shown. Nevertheless, it is safe to assume that for the inner part of a tidal tail a spherical symmetry may exist. As these central parts are expected to have a higher stellar density and therefore are more easy to detect than the outer elongated tails this assumption can be justified. Even in case of a large number of stars in the tail it is possible that such large scale structure will be represented by a multiplicity of clusters.

The KNIME Framework for Data Mining

For applying the cluster analysis to the data the publicly available *KNIME*-framework² is used. *KNIME* is designed as a modular framework for data exploration. It allows the creation of workflows for analyzing and visualization of several different data mining techniques. The framework was developed by the Chair for Bioinformatics and Information Mining at the University of Konstanz. Therefore some of the tools included in this framework resemble this origin because they are specific to problems of human life sciences and chemistry while others are general implementations of data mining techniques like the clustering nodes which were used for this study. *KNIME* itself is written in Java and uses the Eclipse Platform for presenting its GUI to the end-user. Using the GUI the user can create the workflow adequate to the analysis desired. To demonstrate this an easy implementation for a clustering analysis is shown in figure 5.3.

Usually a workflow consists of one or more “data-structures” which represent the input data used. In this case this is the list containing stellar positions and the results of the photometry. This data is then processed by different “nodes”. A “node” represents the most general processing unit and a pipeline of “nodes” is necessary to process the whole data. “Nodes” are used for preprocessing the data, e.g. the preselection that discards incomplete datasets like stellar sources which were only detected in one filter and also for applying the final analysis step. Here this is the clustering algorithm. Finally, the data is presented using so-called “views”. “Views” are sometimes linked to “nodes” and are able to show the results like error-statistics or cluster position etc. But some of the views are visualization nodes. While such “views” do not change the data itself they allow the user to interactively explore it. Such “views” can be linked to processing “nodes” at any position in the pipeline in order to inspect partial results as well as to display the final results.

An example workflow is shown in figure 5.3. It presents a simple pipeline that could in principle be used for a cluster analysis. On the left side there is a “file reader” visible that inserts the data structure into the workflow. The “file reader” is then connected to a “column filter” which is followed by a “row filter”. Both of these “nodes” discard any datasets that do not fulfill the minimum requirements (e.g. visible in all filters etc.). At this point the pipeline is partitioned into two parts to duplicate all the columns that are used in the final analysis. This is done by the help of another “column-filter” which injects its results, the duplicates of the position and magnitude columns, back again into the pipeline data by the help of a “joiner” node. This is done because data must be normalized but for the presentation and interpretation of the results the original values are still important and can then be used without the need of a retransformation of the normalized

²the framework may be downloaded from <http://www.knime.org>

data. The “normalizer” following, is used to bring all the columns necessary for the cluster analysis to a common range of values. This being done, the cluster analysis is carried out by the “fuzzy-c” node. The results of the clustering are then committed to another “row filter” in order to sort out any data points belonging to the noise cluster. This step is done mainly for performance reasons considering the interactive tools. Using this filter more than 90 per cent of the data points are removed and plotting only the important points dramatically increases the interactive plotting performance. This data set, which now consists only of cluster members, pass through a “color manager” and a “color appender” node. Both nodes are used to append different colors to different clusters in order to allow a better visual distinction of each cluster in the last “scatter plot” view. This view shows the spatial distribution (in x- and y- coordinates of the co-added FITS image) of the clusters.

Having said this, figures 5.4 and 5.5 show some views of a test run in order to explain the algorithms. The left hand side of figure 5.4 shows the artificial dataset which contains the cluster data-points of 10 real clusters (colored) and noise (grey). The noise fraction was chosen to be 80 per cent of the data-points. For the recovery the exact number of cluster was assumed to be unknown, because the example should be carried out under the same premises as for the real data. That is to say, the number of k clusters should not be known in advance. In this example fourteen clusters were therefore assumed to be present. The left hand side of this figure shows the result without using a noise cluster in the fuzzy c-means clustering algorithm. It represents the solution of equation 5.5 and shows that every data-point is allocated to one of the fourteen clusters. Naturally, every real cluster is part of one of the discovered clusters but there are also clusters solely consisting of “noise data-points”. This is not a shortcoming of the clustering because the algorithm has still fulfilled its duty to partition the data. Even these noise clusters have something in common but this shows the problem of not finding the global minimum. For this reason the noise cluster (see also equation 5.9) is introduced and a delta is given to characterize the extension of a cluster.

Figure 5.5 shows the results of two such clustering runs. As it can be seen a single clustering run does not identify all the artificial clusters. But if one combines the results of both runs (left hand and right hand side) all clusters have been identified. This also demonstrates the afore mentioned dependence on the randomly chosen starting points. Hence using the clustering algorithm several times and combining the results is therefore absolutely necessary in case of the fuzzy c-means clustering. One should also keep in mind that the results of the clustering runs require a manual inspection afterwards as there were also spurious detections of noise that could resemble a cluster structure. But such detections can be identified by visual inspection, by numbers of members or using the within-cluster-variation (WCV). The visual inspections may be done using the plots seen

in figure 5.5. Table 5.1 and 5.2 show the within-cluster-variation. One can see there that for all recovered artificial clusters this value lies in the range from 0.3 - 0.4 while for all detections of noise as a cluster this value is higher than 0.4. This dependence is expected as the within-cluster-variation is a measurement of the mean distance between the cluster members. Hence for a real cluster it is expected to be much smaller because there should be a central overdensity that reduces this measurement.

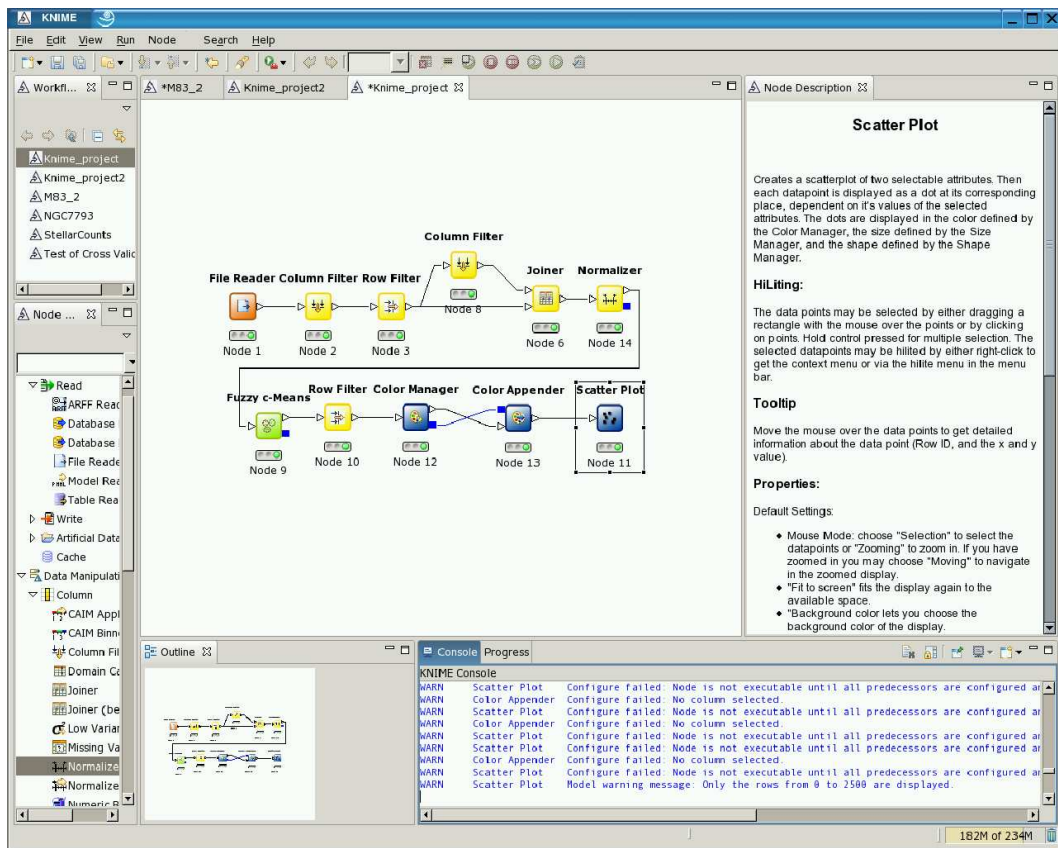


Figure 5.3: Example of a *KNIME* workflow as seen in the GUI. A complete description of this workflow is given in the text. The real workflow is seen in the square sized area in the center of the image and is organized to a degree where the first row represents pre-processing steps while the second row includes the analysis and visualization steps. The other areas covered by tools used to construct the workflow (left area and upper toolbar), to display the online-help (right area) or for diagnostic purposes (bottom area).

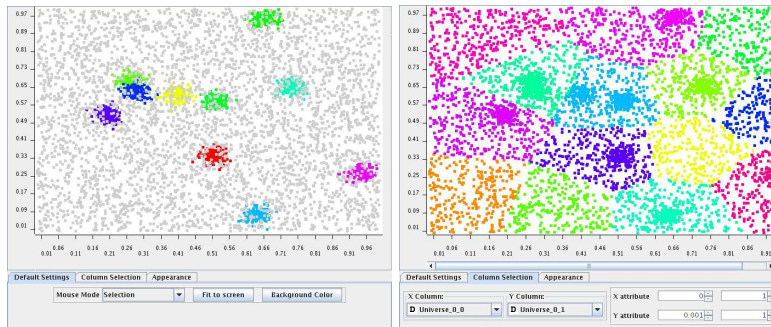


Figure 5.4: The left hand side shows the original setup with the artificial clusters inserted into a non homogenous, noisy, background (grey dots). The right hand side shows the result of a fuzzy c-means clustering without the inclusion of a noise cluster.

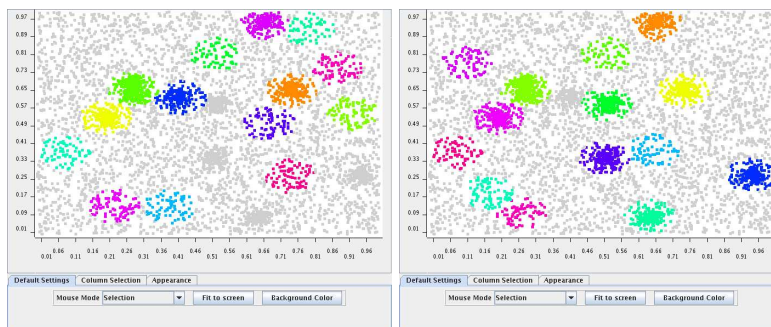


Figure 5.5: These figures represent the results of two fuzzy c-means clustering runs. The data points detected attributed to the noise cluster are marked by grey dots while all cluster detections are colored. Both runs are able to detect a number of the real clusters but they detect also false positives. As the background noise was not chosen to be completely homogenous this effect shows the dependence of the clustering algorithm on the randomly chosen starting points. Multiple clustering runs are necessary to detect all clusters.

| Cluster no. | X-Position | Y-Position |
|-------------|------------|------------|
| 0 | 0.516 | 0.337 |
| 1 | 0.663 | 0.954 |
| 2 | 0.412 | 0.274 |
| 3 | 0.274 | 0.678 |
| 4 | 0.527 | 0.584 |
| 5 | 0.741 | 0.648 |
| 6 | 0.645 | 0.073 |
| 7 | 0.290 | 0.628 |
| 8 | 0.206 | 0.524 |
| 9 | 0.947 | 0.264 |

Table 5.1: Randomly generated positions of the artificial clusters in the test data.

| Run | Cluster No. | X Position | Y Position | Within-Cluster-Variation | Detected Cluster |
|-----|-------------|------------|------------|--------------------------|------------------|
| 1 | 0 | 0.201 | 0.524 | 0.03612 | 8 |
| 1 | 1 | 0.514 | 0.340 | 0.03478 | 0 |
| 1 | 2 | 0.519 | 0.808 | 0.04895 | Noise |
| 1 | 3 | 0.518 | 0.586 | 0.03305 | 4 |
| 1 | 4 | 0.662 | 0.947 | 0.03221 | 1 |
| 1 | 5 | 0.742 | 0.646 | 0.03511 | 5 |
| 1 | 6 | 0.653 | 0.372 | 0.04947 | Noise |
| 1 | 7 | 0.082 | 0.369 | 0.04772 | Noise |
| 1 | 8 | 0.172 | 0.186 | 0.04893 | Noise |
| 1 | 9 | 0.940 | 0.262 | 0.03444 | 9 |
| 1 | 10 | 0.645 | 0.078 | 0.03336 | 6 |
| 1 | 11 | 0.273 | 0.093 | 0.04422 | Noise |
| 1 | 12 | 0.111 | 0.769 | 0.04828 | Noise |
| 1 | 13 | 0.283 | 0.653 | 0.03841 | 3 and 7 |
| 2 | 0 | 0.226 | 0.124 | 0.04958 | Noise |
| 2 | 1 | 0.676 | 0.496 | 0.05062 | Noise |
| 2 | 2 | 0.281 | 0.654 | 0.03877 | 3 and 7 |
| 2 | 3 | 0.521 | 0.808 | 0.04826 | Noise |
| 2 | 4 | 0.742 | 0.646 | 0.03512 | 5 |
| 2 | 5 | 0.201 | 0.524 | 0.03612 | 8 |
| 2 | 6 | 0.388 | 0.124 | 0.04801 | Noise |
| 2 | 7 | 0.737 | 0.260 | 0.04786 | Noise |
| 2 | 8 | 0.082 | 0.368 | 0.04811 | Noise |
| 2 | 9 | 0.419 | 0.613 | 0.03538 | 2 |
| 2 | 10 | 0.794 | 0.920 | 0.04758 | Noise |
| 2 | 11 | 0.875 | 0.747 | 0.04732 | Noise |
| 2 | 12 | 0.660 | 0.947 | 0.03129 | 1 |
| 2 | 13 | 0.918 | 0.544 | 0.04976 | Noise |

Table 5.2: Clusters recovered after 2 fuzzy c-mean runs. Every cluster was found at least one time. For all noise-cluster-detections the within-cluster-variation is significantly higher than for the recovered artificial clusters

Data Analysis

6.1 General Discussion

This section deals with the data analysis itself. In contrast to the previous chapter which was a description of the methods used, this time the results for the different scientific datasets are presented. The analysis will also contain conclusions to explain the findings but the overall picture and the final conclusion of the thesis itself will be the subject of the final chapter 7.

6.2 Analysis of The NGC 300 Data

During analysis of the NGC 300 data several CMDs and Hess diagrams were plotted (Hess 1924) before the construction of the star count maps which represent one of the the most important diagnostic tools for this study. Figures 6.1 and 6.2 show a CMD and a Hess diagram of this galaxy including all stellar-like detections. As one can see the CMD and the Hess diagram are very similar. The difference in the representation of both diagrams is based on the way a data-point is constructed and plotted:

In a CMD the magnitude and color of each star is represented by a single point. The overall representation is therefore a two-dimensional sequence of color and luminosity in a restricted spectral range. In stellar evolution theory the color-magnitude diagram is replaced by the original Hertzsprung-Russel diagram (HRD) that plots a stars temperature (or spectral class) against its (bolometric) luminosity.

A Hess diagram in contrast can be described in short as a binned CMD diagram. That is to say the points plotted in the Hess diagram do not represent a single star anymore, instead they represent the number of stars in a small re-

gion confined by color and magnitude. This diagram simplifies the analysis of the prominence of several features in color-magnitude diagrams. So it is, in principle, a three-dimensional representation of the stellar data where the third dimension is obtained at the cost of losing some fine structures in the plane of the original CMD.

6.2.1 The Star Count Maps

Figure 6.4 shows the distribution of stars mainly belonging to the RGB. The limits for this plot were derived in the way described in chapter 5.3.1. The absolute R magnitude was limited to the area of $23 < R < 25$ and the color range was limited to the interval defined by $0.4 < V - R < 0.8$. Using the isochrone selection criteria this confines the analysis to stellar objects that are most likely members of NGC 300. The limits also suppress the influence of background and foreground objects which are still present in the complete catalog. The presence of foreground objects, for example, can be visualized by using a star count map like the one shown in figure 6.3. This map shows all objects that are brighter than 20 magnitudes and lie within the color interval of $0.2 < B - V < 1.2$. It can easily be seen that these objects do not show any perceivable concentration on the map. A low number of such objects is visible all over the field of view. That is the expected behavior for background and foreground sources.

Referring back to figures 6.4 and 6.5, the plots show the star count maps created using different binning parameters. The top most plot uses a squarish binning area of about 47.6 arcseconds, in the one below this area is about 23.8 arcseconds and in the next plot it is about 11.9 arcseconds. From these plots the first important result for NGC 300 is that using the RGB star count maps neither a tidal stream nor a large scale asymmetry is eminently evident. The only over-densities seen in this plot correspond to positions of NGC 300 spiral arms. But there seems to be a boundary in the numbers of red stars present.

A further investigation of the star count map profile was carried out by counting the stars inside elliptical rings. To accomplish this the text file was converted into an IRAF image using the *IRAF/RTEXTIMAGE* task which is part of the DATAIO package. This IRAF image could then be handled using the *ELLIPSE* task of the STSDAS¹ package within the IRAF framework. *ELLIPSE* fits elliptical profiles based on surface brightness measurements to an image. But in this case the “surface brightness values” are nothing else than the number of stars. Due to the crowding effects discussed earlier, the central region had to be omitted. Therefore the first starting ellipse was placed using a semi-major axis

¹STSDAS Space Telescope Science Data Analysis System. This package and its documentation is available for download at http://www.stsci.edu/resources/software_hardware/stsdas

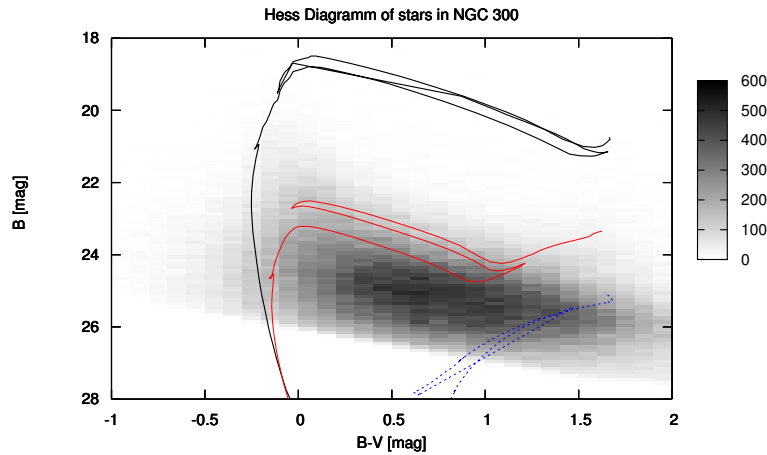


Figure 6.1: Hess Diagram of stars in the NGC 300 Field. Neither a reddening nor a correction for foreground stars has been applied. The black isochrone represents stars of metallicity $z=0.008$ and an age of 10 Myrs while the red isochrone represents stars of metallicity $z=0.004$ and an age of 100 Myrs. Finally stars of metallicity $z=0.001$ and an age of 10 Gyr are represented by the blue isochrone.

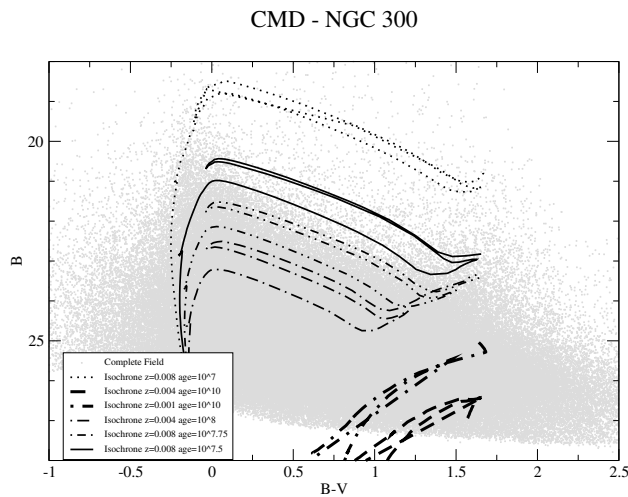


Figure 6.2: Color magnitude diagram of stars in the NGC 300 Field. Neither a reddening nor a correction for foreground stars has been applied. The isochrones, adopted to NGC 300's distance, show the positions of young and old populations in the CMD.

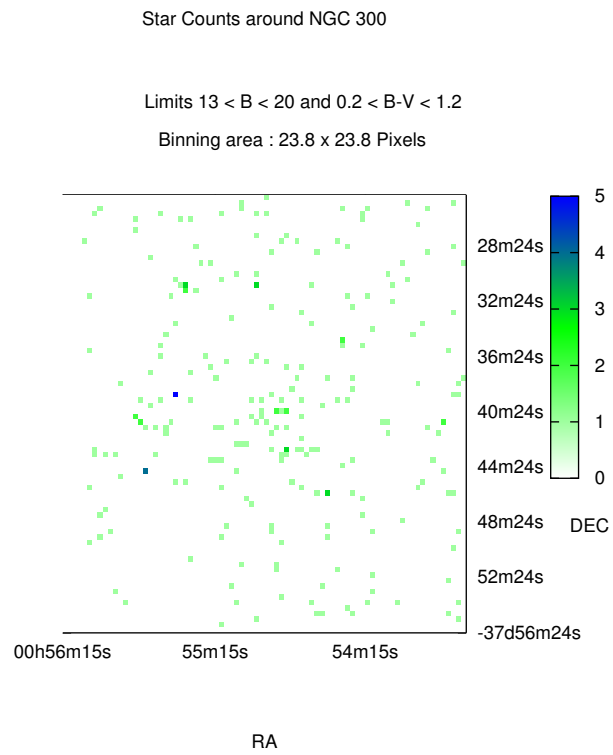


Figure 6.3: A star count map of objects brighter than 20 mag and having $0.2 < B - V < 1.2$

corresponding to a distance of about 240 arcseconds (about 3.5 kpc away from the center). Figure 6.6 shows the number of stars present in elliptical areas around NGC 300 using three different models. The models differ among each other in the starting conditions assumed and in the development of their ellipticity. Two models (marked with circles and triangles in figure 6.6) represent the assumption of a constant ellipticity and a fixed position angle of an initially calculated semi-major axis. These are hereafter called the “constant ellipse” fitting case. The third model however deals with the possibility of a variable ellipticity and a varying position angle of the semi-major axis. So any parameter beside the center of the ellipses, which is fixed in the other models, too, is free to change during subsequent fitting iterations. This model will also be referred to as the “variable ellipse” fitting case.

Calculation and comparison of the models reveal an interesting structure in the sense that in figure 6.6 four different regions of interest are visible. In the first region the number counts of the stars per area is nearly constant. This is again due to the crowding effects discussed earlier. Following this region there are three sections having a different slope of the curve in the logarithmic plot. As a result of this it was tried to fit the data according to the following simple formulae. Such formulae is also used to fit the progression of surface brightness values of disks in spiral galaxies:

$$N_{stars} = N_0 * \exp \frac{R}{h} \quad (6.1)$$

Using linear regression fitting techniques the results according to table 6.1 were obtained. Looking at the correlation coefficient the best model to fit the star count profile is represented by the $e=0.12$ “constant ellipse” fitting case. For this model the slopes of each area are plotted as lines inside figure 6.6. With regard to the other values presented in the plot it is clear that the three different models will come to the same conclusions. The differences in the values derived for each model are very small so there is no general change in the trend depending on the model used. In all cases three regions of different slopes are found. Defining the intersection point of two lines to be the breakpoint between two profiles, two breaks are detected at about 8.75 kpc and 12.2 kpc away from the center. While the first of these two breaks is also clearly visible as a sharp drop in the RGB star count maps (see figure 6.4), the second is not easily spotted there. The surface brightness of this truncation at 8.75 kpc is derived to $25.9 \pm 0.2 \mu_r / arcsec^2$ which makes it darker than expected for a classical Type-II truncation (Pohlen & Trujillo 2006).

The plot in figure 6.7 shows the stellar distribution of and near the main sequence (MS). The intervals in color and brightness were again selected by the help of isochrones, adopted for NGC 300’s distance and external reddening (as described in chapter 5.3.1). In more detailed plots, using a binning of about 23.8

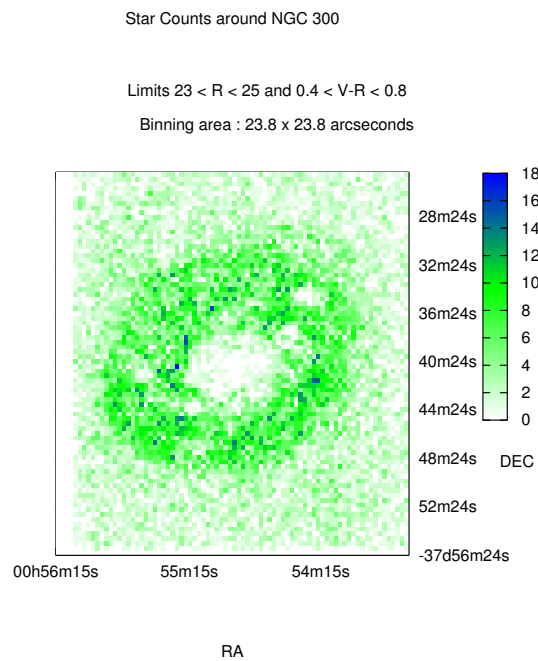
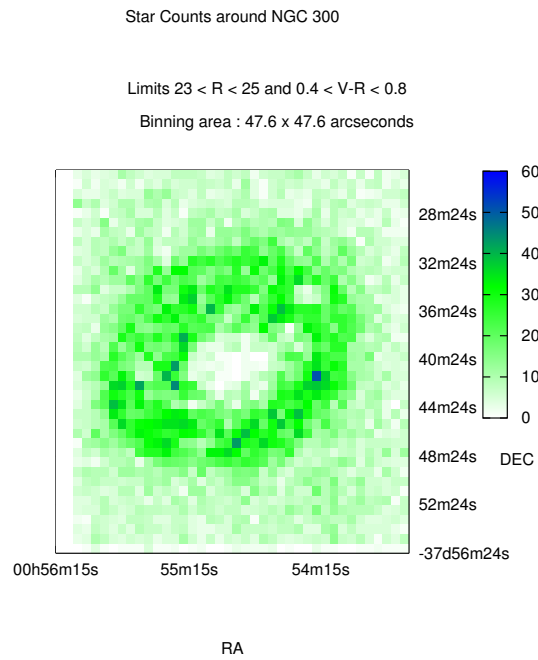


Figure 6.4: Star count distribution maps for the RGB stars of NGC 300 using different binning parameters. The binning area in the top plot is about 47 arcseconds and about 23 arcseconds in the bottom one.

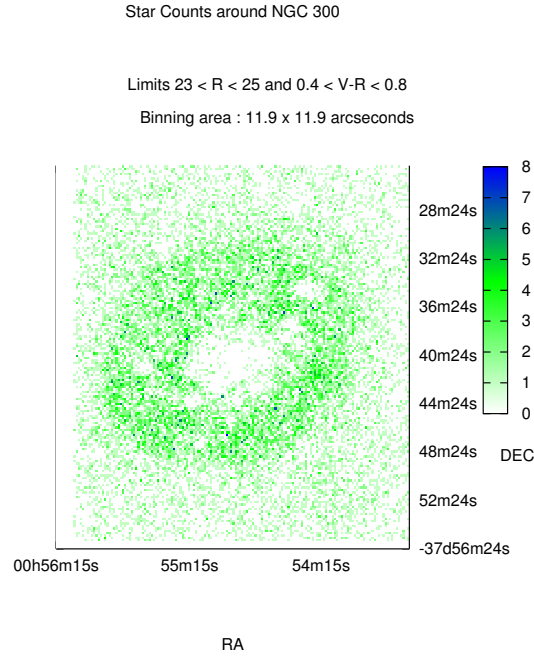


Figure 6.5: Star count distribution maps for the RGB stars of NGC 300 using different binning parameters. The binning area in this plot is about 11 *arcseconds*.

| Ellipticity e | Region | N_0 | $Err(N_0)$ | $1/h$ | $err(h)$ | Correlation |
|-----------------|--------|---------|------------|---------|----------|-------------|
| 0.2 | 1 | 86.10 | 11.97 | -0.0645 | 0.0064 | -0.968 |
| 0.2 | 2 | 806.90 | 243.69 | -0.1603 | 0.0098 | -0.989 |
| 0.2 | 3 | 19.61 | 4.17 | -0.0527 | 0.0054 | -0.965 |
| 0.12 | 1 | 108.24 | 13.54 | -0.0898 | 0.0058 | -0.984 |
| 0.12 | 2 | 375.83 | 20.51 | -0.1402 | 0.0025 | -0.999 |
| 0.12 | 3 | 35.12 | 6.98 | -0.0693 | 0.0050 | -0.982 |
| variable | 1 | 88.46 | 14.21 | -0.0739 | 0.0075 | -0.957 |
| variable | 2 | 1249.80 | 435.86 | -0.1722 | 0.0111 | -0.986 |
| variable | 3 | 73.196 | 27.89 | -0.0880 | 0.0095 | -0.962 |

Table 6.1: Fitting results of the stellar count surface-density plots as seen in figure 6.6 for different elliptical profiles. The correlation coefficients suggests the elliptical model using $e=0.12$ to be the best fit.

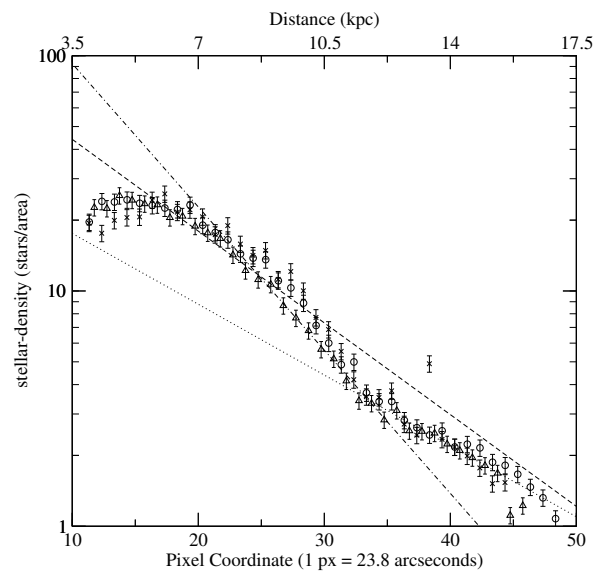


Figure 6.6: Star count surface number densities and best fitting exponential profile. Circles and triangles represent the data-points for “constant” ellipse fitting with $e=0.2$ and $e=0.12$ respectively, while X-markers are used for a “variable” ellipse fitting-case. Lines represent the best fitting profiles for the $e=0.12$ case.

x 23.8 arcseconds and lower, the spiral arms of NGC 300 stand out clearly. It is interesting to note that all high star count regions visible on these plots lie inside the disk before the first truncation of the profile occurs. Notable is also the fact that the amount of such high count regions is not symmetrically distributed all over the galaxy. Instead one sees more regions, also with a larger spatial extension, in the North-West (upper right corner). In contrast to this in the North-East or the South-East very few high count regions are present and the few detectable are of very small spatial extension. This distribution is clearly recognizable in the bottom plot of figure 6.7.

To close the discussion of the star count maps, it is also important to verify their results in the sense of discussing possible limitations and systematic errors. One of the most likely errors that could affect the results very much, would be a systematic error during the reduction and transformation to the standard system. Systematic errors that affect the final photometry are ruled out by the method of the transformation itself. As it was shown in chapter 4.4 the calibration was carried out using standards present in the field of NGC 300. As finding a global solution and applying it to each CCD chip individually did not show any large deviations a sufficient homogeneity of the data over the field of view can be assumed.

Another possibility that could affect the results are foreground and background objects. While such objects may have a non negligible effect their influence in this study is decreased due to two methods:

First, the star count maps are limited in color and absolute luminosity. These boundaries were chosen with the help of isochrones adjusted to NGC 300's parameters like distance and reddening. Hence this limitation excludes many of the foreground objects because due to their distance they will occupy other spaces in a CMD and not the RGB or MS areas. Most of the foreground sources are very luminous (in contrast to NGC 300 stars) and lie in between the areas spanned up by the MS and RGB stars. The distribution for such objects is shown in figure 6.3. As one can see the objects are distributed all over the FOV without any suspicious concentration, in particular there is no connection of these objects to the position of NGC 300. This is another typical sign of foreground objects. The majority of them seem to be equally distributed especially over a larger field of view.

Second, averaged profiles are used as an additional tool to evaluate the truncation radius. Using the method of star counts and the varying elliptical models one gets ϕ_0 , the position angle of the major axis, to be around 120 ± 6 degrees for the inner parts of NGC 300. The ratio of the semi-minor to the semi-major axis (b/a) was measured in the range from 0.76 to 0.88 with a tendency to increase in the direction of the outer parts. Comparing this to table 8 of Carignan (1985) the position angle was calculated there to be around 113 degrees on the average of the inner parts, while the ratio (b/a) lies within 0.55 to 0.81. Therefore, considering

the errors and the fact that there is a fundamental difference between the methods used, star counts on the one hand and surface photometry on the other, these values are in good agreement to each other. So for such truncation to be mocked by background or foreground objects the source for these objects must then reflect the geometry and size of NGC 300. Otherwise it would be hard to explain the similarities in the shape of the surface brightness measurements of Carignan (1985) and the star count profiles. While in principle this could be possible it is highly unlikely.

Finally, an estimation of the number of background sources was made using *GalaxyCount* published by Ellis & Bland-Hawthorn (2006). In the range used for the RGB maps 5 ± 2 background objects should be found per binning interval of 23.8 square arcseconds assuming also a completeness level of 100 per cent. Comparing this with the number of about 10 objects found per binning interval in the area in question for the truncation this could account only for half of the star counts. Further assuming that the distribution of background objects should be isotropic over the field of view it seems to be unlikely that the detected truncation could be mocked by background objects. Otherwise the same argument than before would be necessary to explain the findings. Should the truncation be the result of background sources there must be an anisotropy in its distribution that by coincidence resemble the structure of NGC 300. Considering these values the first truncation should be seen as a real detection and structure of NGC 300. According to the number of background detections the second break which occurs in a region where the number of stellar detections is very low (about 2 detections) this could be a spurious one. It is of the same order of the fluctuations expected in the background. But still as these profiles represent average values there is a good chance that this detection is real.

6.2.2 Data Mining Results Using a Fuzzy C-Means Clustering

From the results of the star count map a large scale substructure was already derived but no signs for smaller scale structures like tidal tails were found. Naturally, such large scale structure will not fit into a single cluster, as the cluster boundaries are too limited. But if such large scale structure of RGB stars is present, then it should be detected as several smaller cluster structures smoothly distributed over the area already identified in the star count maps. Figures 6.10 and 6.11 show four examples of several fuzzy c-means clustering runs. From this figures the large scale structure is immediately evident. About 90 % of the clusters detected have a red color. The mean color of all stars belonging to a detected cluster is 0.776 with a standard deviation of 0.18. This confirms that the smooth structure represented by the smaller clusters is indeed caused by red stars as it was previously derived from the star count maps.

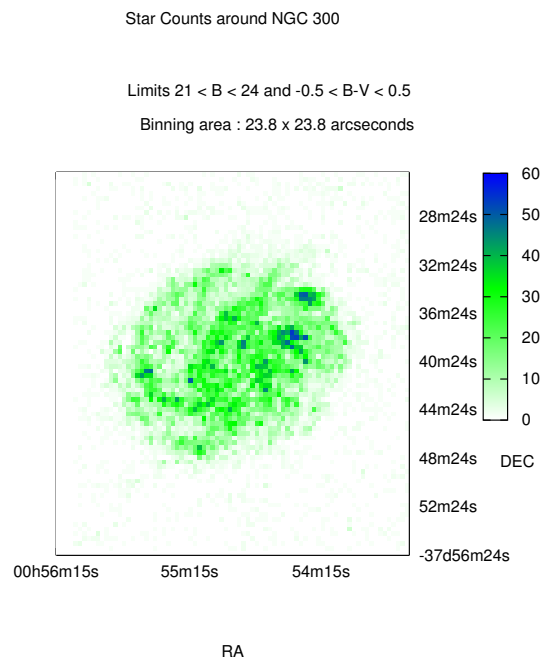
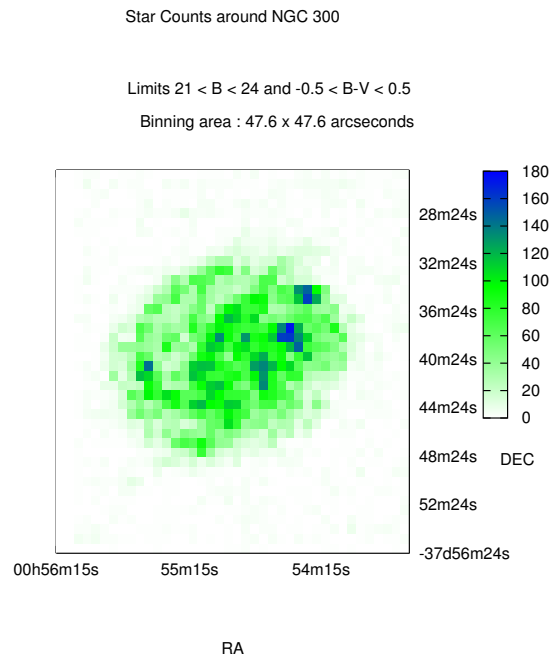


Figure 6.7: Star Count distribution maps for the MS stars of NGC 300 using different binning parameters. The binning area in the top plot is about 47 arcseconds and about 23 arcseconds in the bottom one.

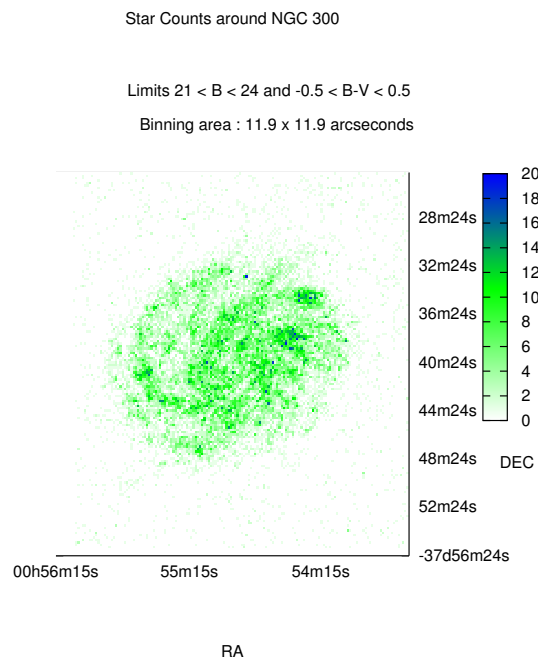


Figure 6.8: Star Count distribution maps for the MS stars of NGC 300 using different binning parameters. The binning area in the plot is about 11 arcseconds. Note the asymmetry in the high star count regions distribution.

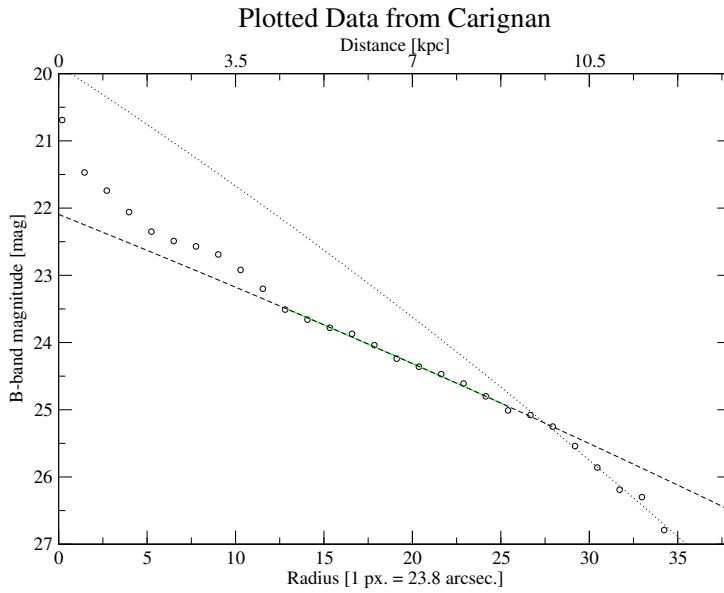


Figure 6.9: Replot of the Data published by Carignan (1985). The scaling of the x-axis has been scaled to reflect the binning parameters chosen in this work.

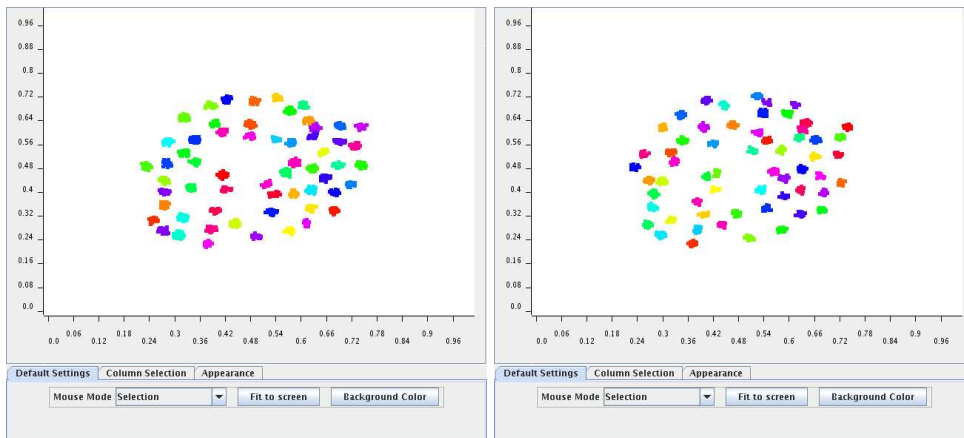


Figure 6.10: Example results of the fuzzy c-means clustering for NGC 300.

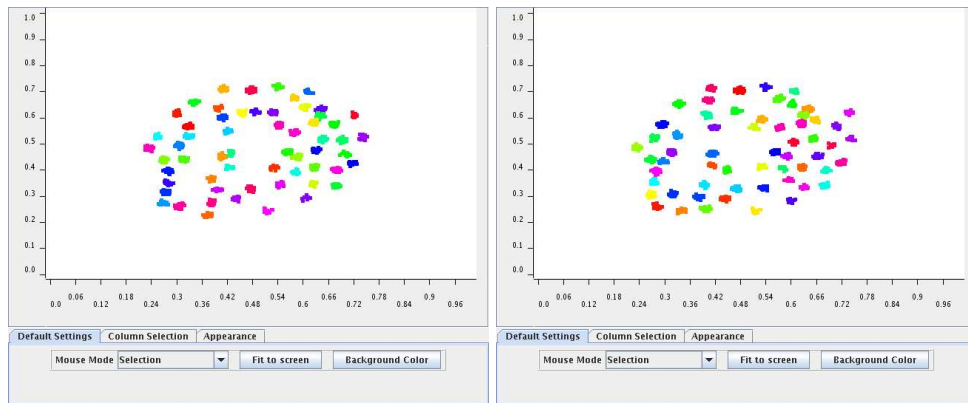


Figure 6.11: Example results of the fuzzy c-means clustering for NGC 300.

6.2.3 Comparison to Other Studies

After presenting the results, namely the truncation and that there is no large scale asymmetry, it is important to compare this to the literature and other previous work. One important study is that of Bland-Hawthorn et al. (2005) that also uses the method of star counts on two Gemini Multi-Object Spectrograph (GEMOS) pointings in the outskirts of NGC 300. In this study they claim that they were able to detect NGC 300's disk out to 10 scale lengths (corresponding to a distance of about 14.4 kpc) and that they did not find any sign for the truncation of NGC 300's disk. This study of NGC 300 also reveals an extended disk structure, because blue MS stars are visible all over the field of view up to a distance of about 14 kpc. The large extension of the disk therefore seems to be confirmed. But in contrast to Bland-Hawthorn et al. (2005) evidence for a truncation of the disk at a radius of about 8.75 kpc (~ 6 scale lengths) and another break at about 12 kpc (~ 8 scale lengths) were found. The question is therefore why such a truncation was not reported by them. To answer this question it should be pointed out that in their study the conclusion of not finding a truncation is not based on the new GEMOS data alone, it is based on summarized results of several studies, namely those of Kim et al. (2004) and Carignan (1985). Hence, the comparison must be made between this study and all these other studies. The first thing to note here is that Kim et al. (2004) and Carignan (1985) both use surface photometry to characterize the disk profile.

Especially interesting for this study is the work of Carignan (1985) from which a replot of his data is shown in figure 6.9. Looking closer at this figure reveals also a slight change in the exponential slope at a distance of about 9 kpc. This is surprisingly close to the truncation radius claimed in this analysis. Interestingly, other support for the existence of such a break comes from a study by Tikhonov

et al. (2005). There they claimed that there is a clear difference between the stellar surface density gradient of the thin and the thick disk (region with a radius 6 kpc) and the halo (region beyond a radius of 11 kpc). Their analysis is based on ACS and WFPC 2 data, but unfortunately it does not cover a continuous band of data from the inside of the galaxy to the outside regions. Instead, the data consists of several distinct pointings that do not cover the range from 8 - 10 kpc distance. Nevertheless, two well separated WFPC 2 pointings exist that allowed them to derive a surface density distribution of RGB stars for a region below 8 kpc and a region lying farther away than 10 kpc. With regard to their analysis it seems to be clear that there must be a truncation present between these two fields to reconcile the data if one assumes the disk to be still present in the outer parts.

So far it has been shown that there are some hints in the literature for the existence of such a truncation of the disk in NGC 300 and the question remains why it was undetected in the study of Kim et al. (2004). A possibility for this could be that the truncation occurs near the end of the FOV used in their study. Therefore, it could be possible that these regions were not sufficiently covered on the one hand while on the other hand the higher photometric errors in these outer regions may have smeared out the beginning of such a change in the gradient. Taking into consideration the low surface brightness of the truncation photometric errors surely could account for the non-detection.

Also in accordance with the truncation is a truncation seen in the HI-surface density. In the maps of Puche et al. (1990) and Puche et al. (1995) a sharp drop in the surface density is visible at a radius of about 9 kpc, the distance at which the warp of the HI disk of NGC 300 sets in. A direct comparison of the data with that of Bland-Hawthorn et al. (2005) at the point of the truncation is not really possible because the GEMOS fields are slightly farther out. There is only a partial overlap with the field used in this study but from this it can be derived that the better resolution of the GEMOS data leads to significant higher number of detections (at least a factor of 10 higher) in the outer parts. Considering this low number of detections in this study in these outer region, it is interesting that the second truncation at 12 kpc occurs near a radius where Bland-Hawthorn et al. (2005) also note a transition of the profile (11.4 kpc). This accordance gives further support to the idea that the non-detection of the truncation in the GEMOS data itself must be due to its position farther out.

6.3 Analysis of M 83 Data

6.3.1 CMDs & Star Count Maps

In analogy to the analysis of the NGC 300 data a color magnitude diagram and several star count maps for M 83 were compiled. This CMD is shown in figure 6.12. As one can see the photometry is not very deep. The isochrones which are also shown for this galaxy prove that the data catches only the giant stars of the youngest populations in M 83. That is to say stars of about 100 Myrs in age. Unfortunately, even these stars lie in the “high magnitude error” regime. The more interesting old populations of RGB stars with ages of roughly 10 Gyr are not visible within the data. Using the distance modulus for M 83 as it was measured by Thim et al. (2003) of 28.25 mag and considering that the tip of the red giant branch in V is normally located at an absolute magnitude of about -3 mag one would need the photometry to reach down to at least 26 magnitudes to detect the tip clearly.

Nevertheless, some star count maps to look for asymmetries in the data at hand were constructed. These maps are shown in figure 6.13 and 6.14. As seen, in all four maps M 83 is clearly visible in the center of the images but lacking any real sign for a tidal tail. The spiral arm structure is reflected very well in all four maps. This is a direct consequence of the fact and depicted by the isochrones in figure 6.12, that all four maps only visualize the presence and position of very young stars (figure 6.13) or the most luminous and very young supergiants (figure 6.14). Therefore, it is not possible to get any good hints for stellar streams or tidal tails from the star count maps. But in addition to this, not finding very young and luminous stars outside means that there are no massive star formation regions.

But instead of obtaining a very deep photometric analysis for the stars in M 83 it was possible to partially resolve two streams in surface brightness measurements that were originally observed on a photographic plate and published by Malin & Hadley (1997). On this deep image the most prominent feature is an enormous loop visible in the North-West of M 83. With the new wide field imaging data it was possible to recover this loop in the North-West in 4x4 pixel binned images. Additionally, it was possible to recover a slightly smaller stream on the other side of M 83 in the South-(East), too. For both streams the B-V color could be derived to about 1.03 ± 0.15 mag for the North-West loop and about 1.48 ± 0.17 mag for the southern stream. If one compares these results with theoretical isochrones this would imply a red giant branch population of ages in the range from 4 to 7 Gyrs if one assumes a lower metal abundance of $z=0.004$ for the outer parts of M 83. This assumption is based on observations by Gil de Paz et al. (2007) where they found that M 83s metal abundance is increasing from outside to inside. Values range from 1/10 solar metallicity in the outer halo regions to solar metallicity near

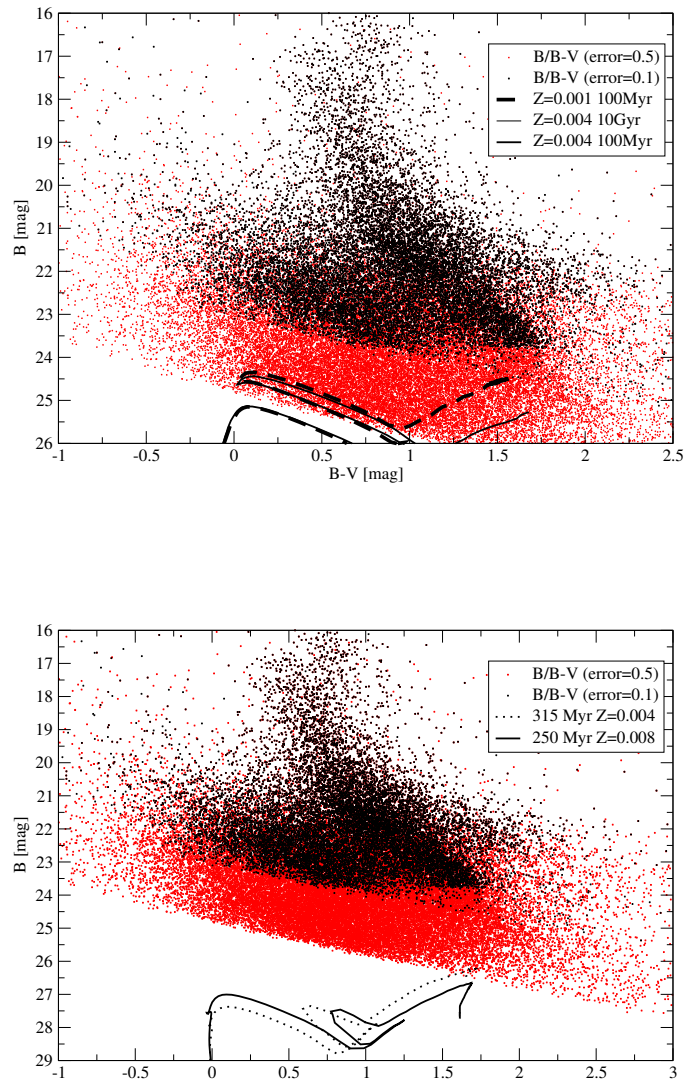


Figure 6.12: Color magnitude diagrams of M 83: The black points represent detections with magnitude errors lower than 0.1 mag while red points have a higher than 0.1 but lower than 0.5 mag error. Also shown are distinct isochrones adopted to the distance and reddening of M 83. The left hand side shows isochrones of 100 Myrs and the absence of the isochrone for 10 Gyrs and $Z=0.004$ inside the magnitude limits set by the photometry. The right hand side shows the positions of isochrones for ages around 300 Myrs in $Z=0.004$ and $Z=0.008$ that are interesting for star forming episodes in the outskirts of M 83.

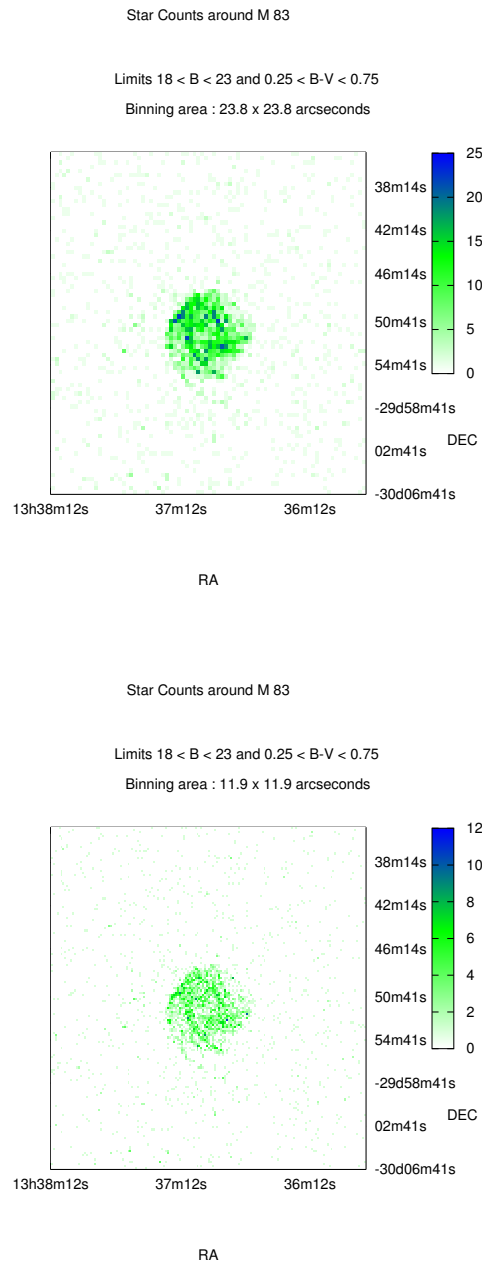


Figure 6.13: Star count map of M 83 for the blue part of the CMD

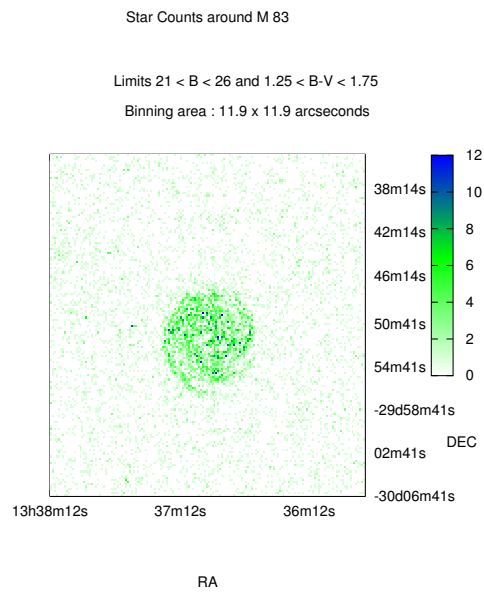
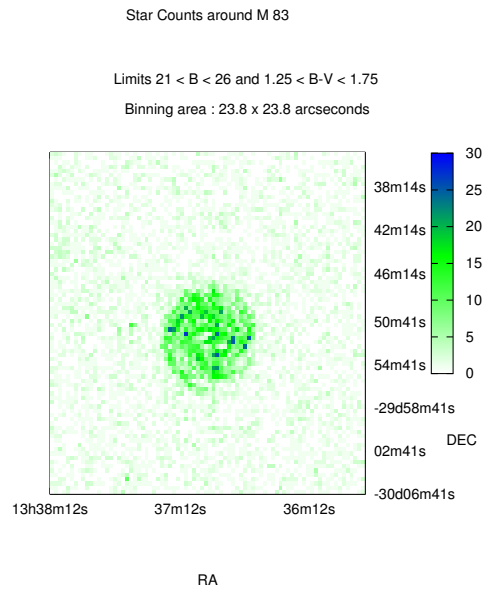


Figure 6.14: Star count map of M 83 for the red part of the CMD

the optical counterpart of the galaxy.

6.3.2 Data Mining Results Using a Fuzzy C-Means Clustering

A different approach from analyzing the star count maps is the data mining approach. In this analysis a fuzzy c-means clustering algorithm was used to look for overdensity regions without making any assumption regarding the absolute magnitude or color of the objects or the cluster (unsupervised clustering run; see also chapter 5.3.2 for the clustering discussion). The complete data from the color magnitude diagram is inserted into the clustering algorithm and for each run a visual output is computed. Some examples are shown in figure 6.15. For the clustering a number of 40 clusters was anticipated to be the optimum number of clusters per run. That this number cannot be completely wrong is acknowledged by the fact that there are only a few clusters represented by a single datapoint. But as it was already seen in the star count maps there is little evidence for interesting overdensities outside the central part. Certainly, there are three interesting clusters visible outside but they have only 3 - 8 members (left hand side of figure 6.15). As it was discussed in chapter 5.3.2 they could be explained by the presence background sources alone. In comparison to this the clusters in the center have at least 40 members. A further investigation into the cluster magnitude values yields that the largest cluster outside has $B \simeq 23.6$ with $B - V \simeq 0.78$ placing it far away even from the younger “interesting” populations represented by the isochrones in figure 6.12. All other “few-point clusters” are not detected in subsequent runs.

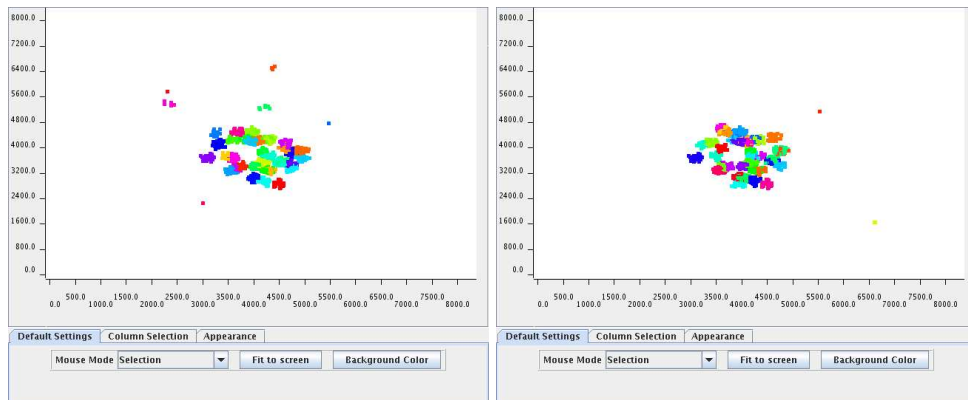


Figure 6.15: Example results of the fuzzy c-means clustering. All clusters outside the central part have only 8 members or less.

6.3.3 Comparison of Other Studies

The first thing to note about M 83 in this analysis was the observation of many young stars regardless of whether they were young MS stars or young supergiants. Such findings imply that a star forming event has been taken place not long ago or that it is still taking place in the galaxy. Hence, there should be other observations supporting this idea in the literature. Indeed several other publications exist that deal with the starforming events in M 83. A giant HII complex in the nucleus of M 83 was identified by Arsenault & Roy (1986) making M 83 one of the nearest galaxies in which a nuclear starburst is observed. Although the discovery of this nucleus starburst region was some time ago the real structure of its stellar sources is still not completely resolved. On the one hand there were hints for a second nucleus to be present, represented by a hidden mass, in the center of the galaxy (Sakamoto et al. 2004, Mast et al. 2006) or on the other hand the structure was traced back to the presence of a resonance pattern of a weak bar (Elmegreen et al. 1998, Petitpas & Wilson 1998, Gallais et al. 1991). A depth photometric study using the HST WFPC 2 made by Harris et al. (2001) showed that there is a giant star forming arc located between 3 and 7 arcseconds from the center and that the starburst has begun about 10 Myr ago. These findings are also supported by newer spectroscopic observation of Díaz et al. (2006) who also found evidence for the location of the hidden mass at the younger end of the starburst arc. They also pointed out that the optical nucleus of M 83 is out of the galactic geometric center and that it seemed to have left a stellar trail behind which is still pointing towards the geometric center. In their picture this could be caused by the passage of an interloper. Hence, the origin of the arc remains unclear and it could either be bar-funneled material or a cannibalized satellite.

For the outer parts of M 83 the study of de Jong et al. (2007b) is of importance as they have analyzed the northern-stream of M 83 using data from the HST GHOSTS survey. The color magnitude diagram provided in their work shows a prominent metal poor RGB population, a less prominent AGB, and the absence of stars leftward of the RGB. This, they argue, would indicate a 3-5 Gyr old population without star formation within the last 300 Myrs. Therefore these results, which used deeper photometric data than at hand, are in an acceptable agreement with the results of this work. Also interesting is another study of the GHOST team (de Jong et al. 2007a) in which they discuss the profile of this galaxy up to a radius of about 20 kpc and do not find any deviation of the profile from a pure exponential disk profile. This is again further support for the results presented in the previous paragraphs which were not able to see an extended stellar structure in the halo or disk, e.g. like the one detected in NGC 300 (see chapter 6.2).

Nevertheless there are also hints for star formation in the outer parts of the galaxy. Using GALEX observations Thilker et al. (2005) revealed more than 100

UV-bright star forming regions that are located preferentially at local maxima of filaments of the warped HI disk. While it is true that there are some spikes in the distribution presented in the blue star count map of figure 6.13 none of this spikes are coincident with the the GALEX FUV and NUV image presented by Thilker et al. (2005). Also with the use of the data-mining approach it was not possible to find any prominent features that match features on the GALEX map. Nevertheless, considering the photometric depth of this data this is not unexpected. Putting together the results of the GALEX Survey, the metal abundance gradient for M 83 presented by Díaz et al. (2006) and the results by de Jong et al. (2007b) the outer star forming regions must be of low metallicity (i.e. $Z=0.004$ or $Z=0.008$) and having ages of at least 300 Myr and larger and addressing this by isochrone plots one sees that the stars of such star forming regions are outside of our photometric boundaries.

6.4 Analysis of M 33 Data

6.4.1 CMDs & Star Count Maps

In figure 6.16 two color magnitude diagrams of M 33 are shown. These are based on the data by Burggraf et al. (2005). The isochrones for $Z=0.001$ and $Z=0.004$ specify interesting regions of young and older populations at the distance and reddening of M 33. Therefore, the limits for the star count maps were set to $16 < V < 20$ with $-0.5 < V - I < 0.5$ for the younger population and $20 < V < 21.5$ with $1 < V - I < 2$ for the old population. The corresponding star count maps are shown in figure 6.18.

For the blue star count map signs of the spiral structure of M 33 are noticeable. There are several areas present showing overdensities along the spiral arm structure in the North-East and also in the South-West. In addition, the central parts of M 33 do not show the strong and typical drop off in stellar number density, as it was seen for NGC 300 in the star count maps (see e.g. figure 6.7). The reason for this is the higher resolution of the M 33 data in its central parts that is surely a result of M 33's proximity. In contrast to NGC 300 which is about 2.1 Mpc (Gieren et al. 2004) away from us, M 33's distance is only about 847 kpc (Galleti et al. 2004; Sarajedini et al. 2006).

According to McConnachie et al. (2004) the tip of the red giant branch in M 33 lies at $I \sim 20.54$ magnitudes. Comparing this with the data at hand shows that the data is at least half a magnitude deeper than this tip. To extract the old populations the boundaries for the star count map were set to be $20 < I < 22$ magnitudes using a color interval of $1 < V - I < 2$. The resulting star count maps are presented in figure 6.18. High count regions with more than 5 stars per binning interval

correspond either with the central part of the galaxy or its spiral arms. Although these maps do not show strong hints for tidal tails a slight deficiency is visible in the south-west part of M 33. While in all other outer regions there are filaments of 2-3 stars present, in the South-West only a few filaments remain. In addition to this they tend to have only 1-2 stars. To clarify this finding another star count map was created using slightly changed boundaries. It is shown at the bottom of figure 6.18. In it the afore mentioned deficiency remains still the same. A comparison with the blue star count maps of figure 6.19 showed that now there is nothing special about this region any more. Instead of the deficiency seen before the southern spiral arms stand out very clear.

To further investigate this asymmetry star count maps from another data set were created. The images were again taken with the same telescope and by the same observers, namely the Mayall Telescope and the NOAO Group. This time they were not centered on the galaxy. Instead of this one position covers the north and the other one the south part of M 33. In addition to having now two frames, one for the north and one for the south, available the photometric depth of the images of this later observations seem to be slightly larger which results in more detections. According to the CMDs shown in figure 6.17 these fields seem to be about 0.2 magnitudes deeper. Figure 6.20 shows these star count maps for the northern part of M 33 and figure 6.21 for the southern part. In these images the afore mentioned asymmetry cannot be recovered any more. But it shows that higher star count regions outside of the central part are always associated with the spiral structure of the galaxy. The spiral structure seen on these images is in very good agreement with the model presented by Ivanov & Kunchev (1985) of seven spiral arms of which four spiral arms are detected in the northern part and three are detected in the southern part. This finding of Ivanov & Kunchev (1985) supports again an asymmetry between North and South in M 33 but the new maps show that along the spiral arms the number counts of the stars do not vary significantly between all secondary spiral arms.

6.4.2 Data Mining Results Using a Fuzzy C-Means Clustering

Another approach to analyze the data of M 33 was made using the *KNIME* data mining framework and the cluster analysis methods implemented in it. As it was already explained and shown (see chapter 5.3.2 ff.) the basic idea for this step was to gain independence from the preliminary assumption what color and luminosity a stream of stars will have. The expected advantage of such handling is that the search will be more robust toward photometric errors and that the cluster analysis would show significant streams even if they are overlapped by foreground or background objects.

To begin the cluster analysis for the first time it was tried to map the galaxy

itself by a larger number of different clusters. This should in principle be possible as a galaxy is normally represented by a conglomeration of stars in a CMD and confined by the position on the sky. Therefore, if the principle of such an analysis would work one should be able to map the structure of the galaxy with a large number of clusters as many stars of a galaxy should have something in common. Figure 6.22 shows the result of such large scale clustering. As one can see the clustering algorithm was able to visualize the most prominent parts of the galaxy, namely the spiral arms and the central parts (colored dots). The grey dots represent stars that were assigned to the noise cluster. Therefore, they are not members of any cluster. The position and magnitude parameters set allowed a radial extension of about 1000 Pixels (about 4.8 kpc in the plane of M 33), a V-band magnitude deviation of about 2 magnitudes and a color deviation of about 0.6 mag.

After this first check of the clustering principles for the data in hand, the real clustering runs were started. In contrast to the above clustering with the aim of remapping the whole galaxy the limits defining the extension of the cluster (namely the maximum intra-cluster distance) were set to a more restrictive value. Now a typical cluster is allowed to have an extension of about 500 pixels (about 0.5 kpc in the plane of M 33), a V-band magnitude deviation from the mean of about one magnitude and a color deviation from the mean of about 0.2 mag. The results of some exemplary runs are shown in figure 6.23 and 6.24. In table 6.2 some properties of significant clusters are presented. All clusters in this table must have at least 12 members and a dense core with at least 6 stars inside a 150 pixel radius. Comparing this limit with the binning parameters used for the star count maps the area for a cluster is now 2.25 times larger (in case of the 100 pixel binning = 27.1 arcseconds). Hence the lower bound of 12 stars is not too high if one compares this to the star count maps where high count regions contain more than 4 stars (in a 100 pixel binning). The reason for these limits that are more strict than for the other galaxies is the resolution of M 33. In contrast to the other galaxies more stars are resolved as the effects of crowding are significantly smaller due to M 33's proximity. As a consequence rising the limits avoids selecting some false candidates. This is necessary in order to speed up the manual analysis of the clusters.

One fact in table 6.2 is striking. The large majority of clusters found lie in the blue regime of the CMD. Only cluster number 13 could be described as having predominantly red members. This result is in good agreement with the star count maps presented before (see figures 6.18 and 6.19). Looking at all red star count maps one sees that there is a smooth distribution of red stars present with an extremely low number of higher count regions. This picture changes slightly for blue stars. Depending on limits of the star count map there are some differences. Moving the limits slightly from blue (figure at the top) to red (figure at the bottom) the more clumpy structure is smoothed out. This finding is also supported by the

clustering results as most identified clusters have very blue colors in the range of -0.15 magnitudes. Hence, the clustering has mostly found denser stellar regions in the spiral structure of M 33. To underline this statement column 6 of table 6.2 gives the names of the spiral arms in which the clusters were detected. The nomenclature of these spiral arms was adopted from Ivanov & Kunchev (1985) who presented a detailed model of M 33's spiral structure. Only two clusters could not be mapped to the spiral structure but these two lie inside or very near to HII regions.

6.4.3 Comparison to Other Studies

Comparing these results to other studies one has certainly to incorporate the different studies of Ibata, Ferguson and co-workers (e.g. Ibata et al. (2001); Ferguson & Johnson (2001); McConnachie et al. (2006); Mackey et al. (2007)) which also search for substructures by the method of stellar counts in the region around the Andromeda Galaxy (M31). While most of this work has already been discussed in the in chapter 2 at this point only their work dealing with M 33 is of relevance. In this context Ibata et al. (2007) present the results of a deep photometric survey of the Andromeda Galaxy that extends into the halo of M 33. They report that they did not find any significant sign of substructures in the M 33 halo even for those areas in the M 33 halo which probably pass through the M 31 halo. According to their measurements the M 33 halo might be fitted using a Hernquist model from which they deduce a scale radius of about 55 kpc. But they also mention that the actual data lacks a full panoramic study. Therefore, some substructures could still be unidentified. In another publication (Ferguson et al. 2007) a complete RGB star count map of M 33 is presented and no asymmetry or tidal tail is visible. This study had the same limiting magnitude depth of about 30 mag per square arcsecond as the M 31 analysis but in which significant evidence for substructures were found. Therefore, the authors concluded that M 33 evolved undisturbed. A first hint for a tidal stream so far comes from McConnachie et al. (2006) in which they revealed a third kinematic feature in the southern fields. The comparison of this feature to a simple disk model of the galaxy yielded that this feature did not arise from the line-of-sight viewpoint. Instead they also emphasized that the locus of these stars identified in the CMD had a relative small color dispersion as it would be expected as a result of a single stellar population.

Another hint for an asymmetry of stars, namely carbon stars (C stars) comes from Block et al. (2004). The authors found evidence for a ring of carbon stars extremely prominent in the northern part of this galaxy where its surface brightness is 20-21 mag per square arcseconds at a wavelength of $2.2 \mu m$. In the southern field the carbon stars could still be recognized but the surface brightness there is much fainter.

| Cluster No. | X-Center | Y-Center | B [mag] | B-V [mag] | WCV | Spiral arm-No. |
|-------------|----------|----------|---------|-----------|-------|----------------|
| 1 | 1941 | 4712 | 21.42 | -0.16 | 0.036 | N1 |
| 2 | 2396 | 3512 | 20.91 | 0.02 | 0.036 | S3 |
| 3 | 3321 | 3638 | 21.14 | 0.17 | 0.038 | S3 |
| 4 | 4060 | 3926 | 19.02 | -0.144 | 0.038 | N3 |
| 5 | 4389 | 4765 | 19.69 | -0.127 | 0.036 | N1 |
| 6 | 4597 | 2292 | 20.48 | -0.06 | 0.037 | S1 |
| 7 | 305 | 5706 | 21.03 | -0.11 | 0.037 | N2 |
| 8 | 5383 | 542 | 20.88 | -0.02 | 0.037 | S2 |
| 9 | 6401 | 1638 | 20.65 | -0.11 | 0.036 | S2 |
| 10 | 4331 | 4795 | 21.66 | 0.40 | 0.035 | N1 |
| 11 | 3638 | 4707 | 22.11 | 0.47 | 0.036 | S3 |
| 12 | 1714 | 5957 | 21.73 | 0.44 | 0.038 | N1 |
| 13 | 3105 | 6451 | 22.20 | 0.71 | 0.036 | N2 |
| 15 | 1354 | 3223 | 21.13 | -0.19 | 0.034 | N1 |
| 16 | 790 | 4543 | 21.27 | -0.15 | 0.034 | - |
| 17 | 7977 | 2968 | 21.05 | -0.13 | 0.036 | S2 |
| 18 | 5768 | 7105 | 21.12 | -0.17 | 0.034 | N4 |
| 20 | 2920 | 1679 | 21.34 | -0.15 | 0.039 | S3 |
| 21 | 1980 | 1324 | 21.25 | -0.20 | 0.035 | S3 |
| 22 | 3483 | 2096 | 20.28 | -0.14 | 0.038 | S1 |
| 23 | 5823 | 5598 | 21.41 | -0.11 | 0.035 | N4 |
| 24 | 6297 | 1591 | 21.17 | -0.10 | 0.036 | S2 |
| 25 | 3972 | 7954 | 21.16 | -0.17 | 0.033 | N3 |
| 26 | 6705 | 3032 | 21.06 | -0.16 | 0.034 | S1 |
| 27 | 7835 | 1834 | 21.31 | -0.10 | 0.035 | - |
| 28 | 2539 | 7807 | 20.82 | -0.15 | 0.037 | N3 |
| 29 | 3002 | 7408 | 21.49 | -0.14 | 0.037 | N3 |
| 30 | 6114 | 4949 | 20.60 | -0.13 | 0.038 | N4 |
| 31 | 5824 | 3942 | 19.53 | 0.07 | 0.037 | N4 |
| Noise | - | - | - | - | 0.423 | - |

Table 6.2: Cluster properties in the M 33 dataset. The spiral arm number given in column 6 is chosen according to the model calculated by Ivanov & Kunchev (1985). Only two clusters could not be mapped to spiral arms of this model. But instead they lie very close to HII regions. The noise cluster WCV has been given as a reference in order to show the difference in the WCV value of objects not related to each other.

A study of Barker et al. (2007a) dealing with the stellar population in the outskirts of M 33 showed the presence of a mixed stellar population whose youngest members are up to 100 Myr old and whose oldest members are several Gyrs old. Hence they concluded that the presence of such young stars is consistent with a low global star formation threshold. A complete analysis of the star formation history (SFH) of M 33 done by the same group (Barker et al. 2007b) narrowed down the ages for the majority of older stars to 6 - 8 Gyrs. But the beginning of the star formation was dated back 14 Gyrs ago. In addition to this the study showed that the star formation in M 33 was not constant over the galaxy's lifetime. While in the beginning (approx. from 5 - to 14 Gyrs in age) the star formation rate (SFR) was nearly constant in all three observed ACS fields a peak occurred during ages from 2.5 - 5 Gyrs. The metallicity using the data was calculated to be of $[\text{Fe}/\text{H}] \sim -0.7 - -0.9$ dex. This value is in good agreement with other studies of the metallicity. Cioni et al. (2007) used wide field near-infrared imaging observations and determined the $[\text{Fe}/\text{H}]$ value for the nucleus and regions around it to -1.2 dex while they were also able to trace C stars which are as metal poor as $[\text{Fe}/\text{H}] = -1.6$ dex. In the central part however they also found evidence for metal rich stars of $[\text{Fe}/\text{H}] = 0.3$ dex.

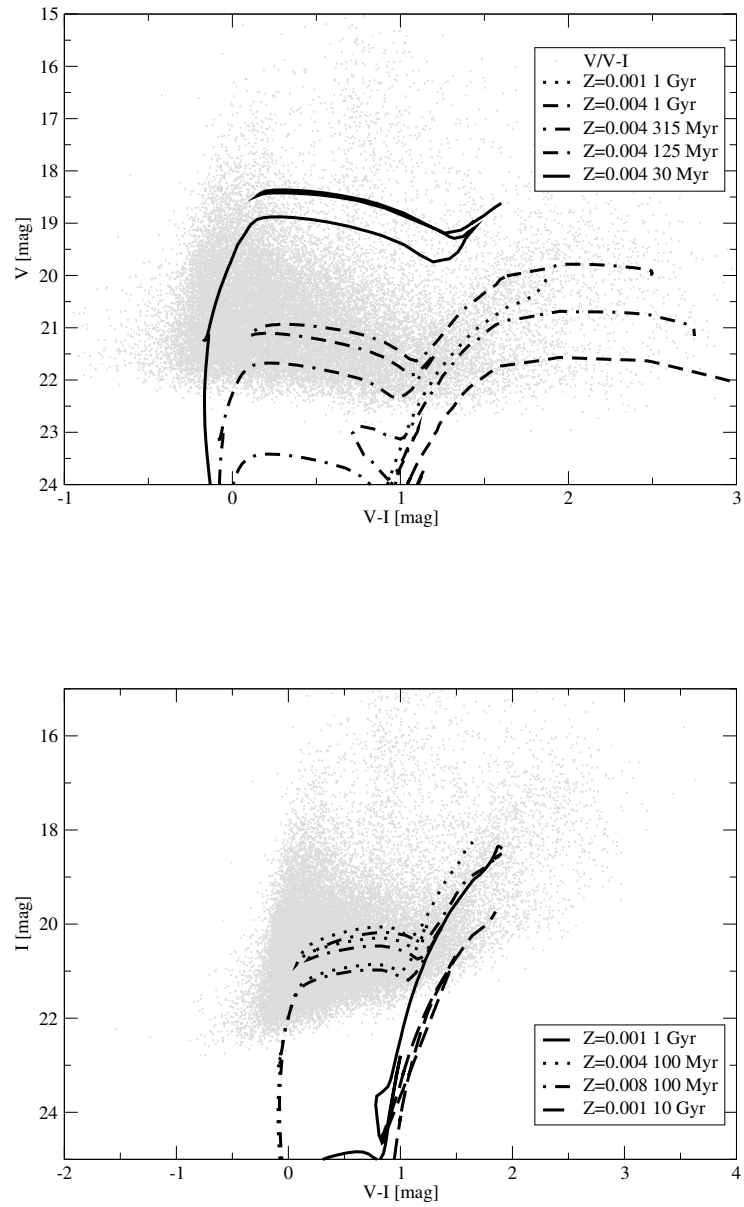


Figure 6.16: Color magnitude diagrams of M33 including some isochrones for $Z=0.001$, $Z=0.004$ and $Z=0.008$

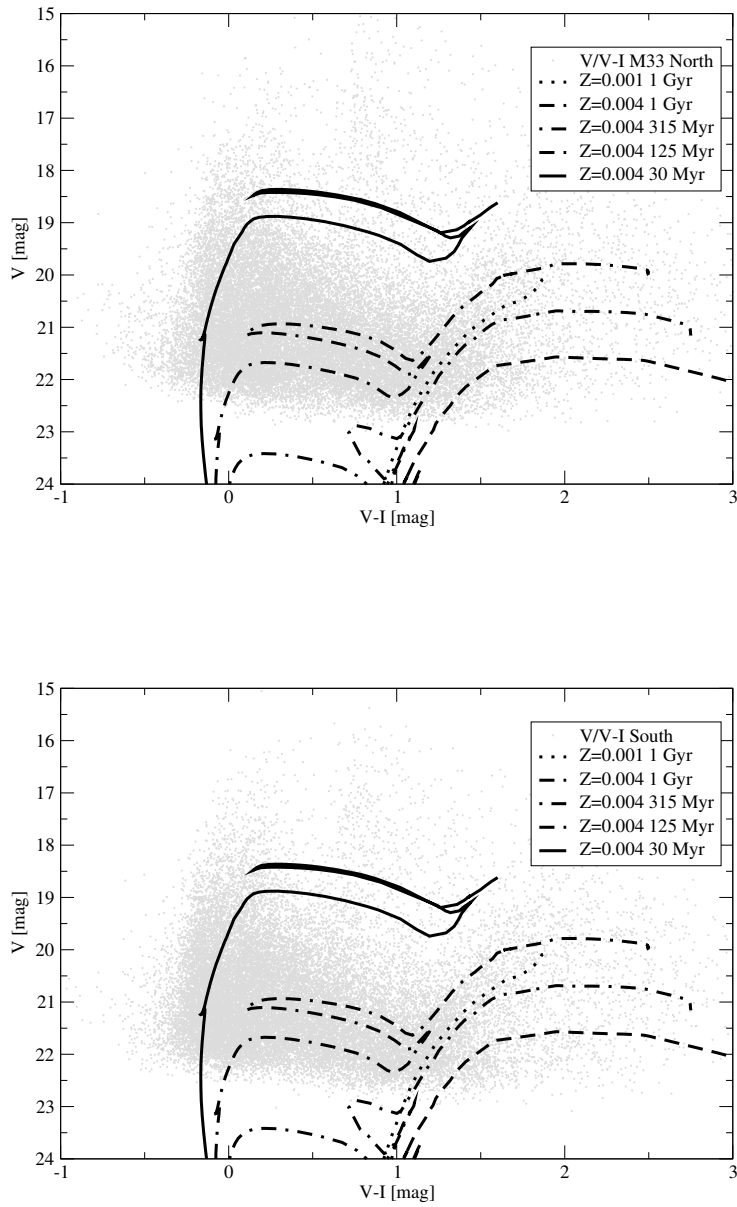


Figure 6.17: Color magnitude diagrams of M 33 including some isochrones for $Z=0.001$, $Z=0.004$ and $Z=0.008$. The top map represents the northern field while the bottom map shows the southern field.

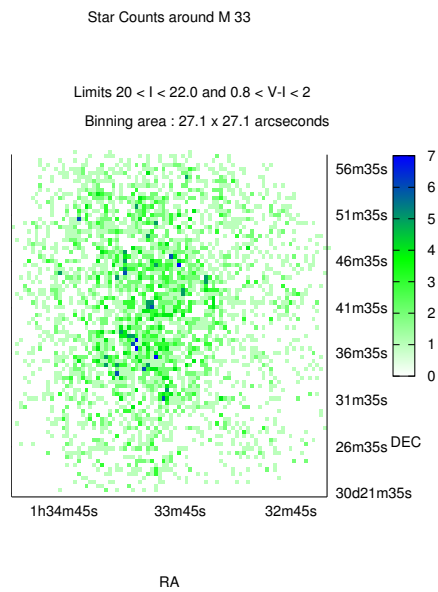
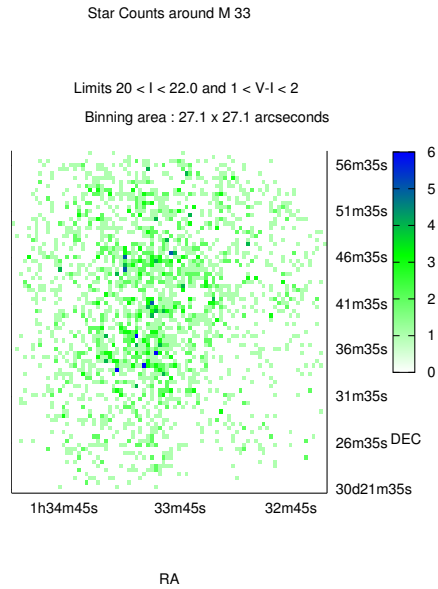


Figure 6.18: Star count maps of old populations in M 33. Both images show the positions of stars belonging predominantly to older populations (larger than a Gyr) of M 33.

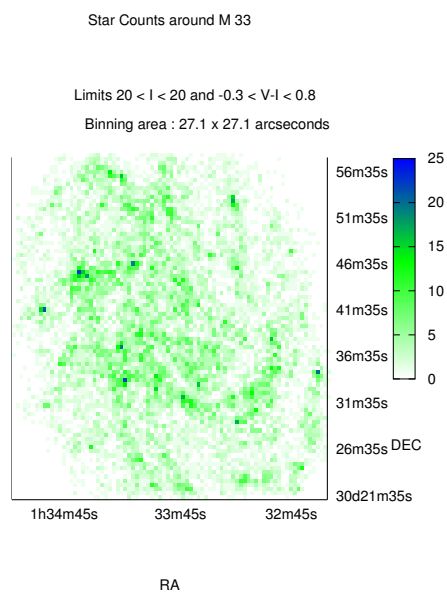
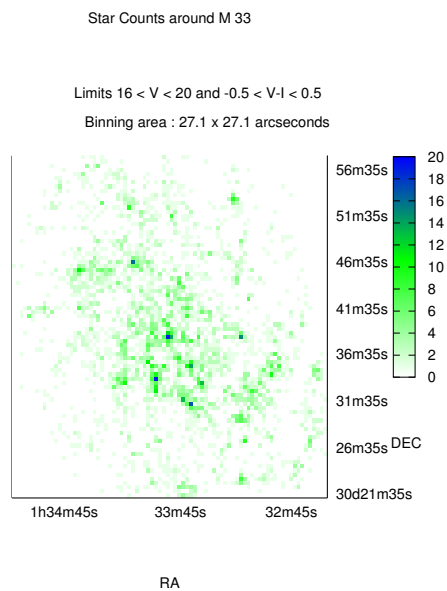


Figure 6.19: Star count maps for younger populations in M 33. Both images show the positions of stars belonging predominantly to younger populations (about several 100 Myrs) of M 33.

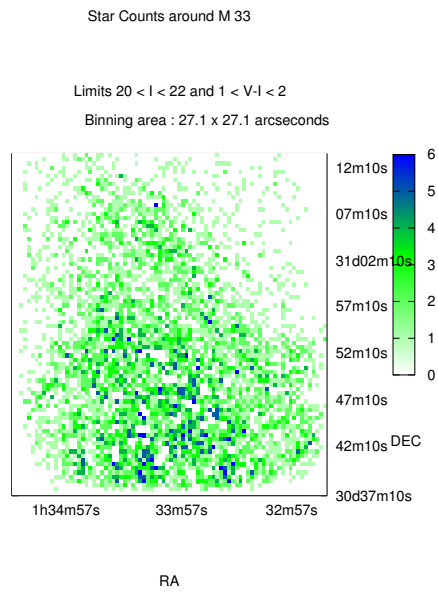
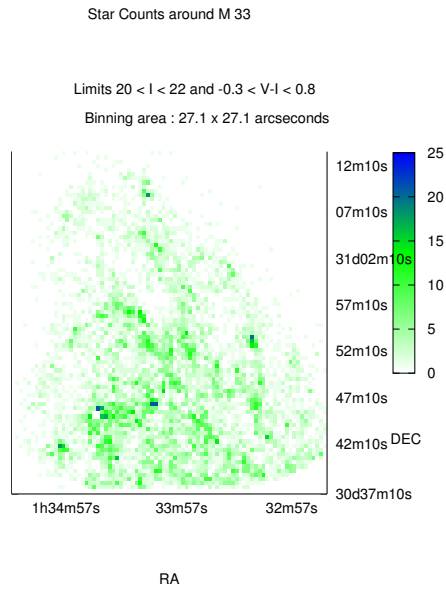


Figure 6.20: Star count maps for the north part of M 33. On the left the map for the blue stars is presented while on the right the distribution of red stars is seen. The magnitude limits are the same as used in the previous maps.

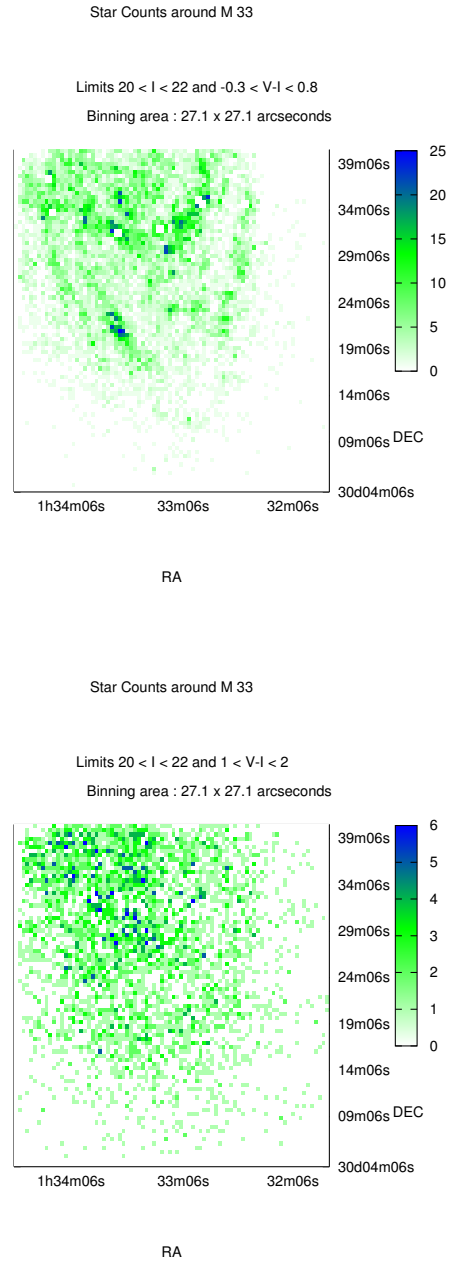


Figure 6.21: Star count maps for the south part of M 33. On the left the map for the blue stars is presented while on the right the distribution of red stars is seen. The magnitude limits are the same as used in the previous maps.

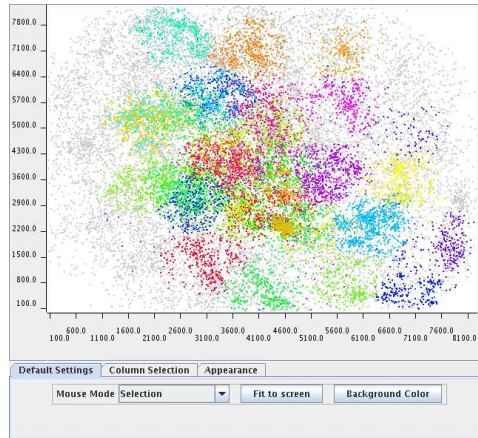


Figure 6.22: A cluster analysis done to search for the most prominent features. Grey dots represent stars attributed to the noise cluster while colored dots represent recovered clusters.

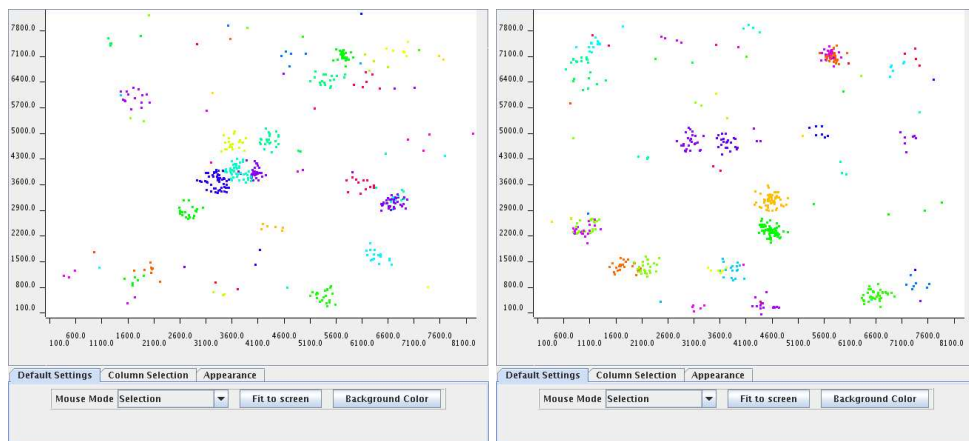


Figure 6.23: Two example clustering runs with 59 clusters for M33

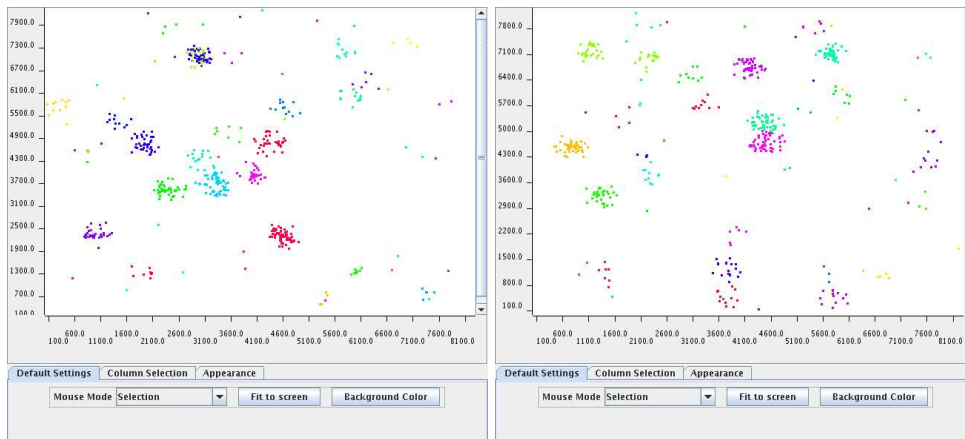


Figure 6.24: Another example of two clustering runs with 59 clusters for M 33

6.5 Analysis of NGC 7793 Data

6.5.1 CMDs & Star Count Maps

In analogy to the analysis of the other datasets, the CMDs and the star count maps are the first approach to examine the distribution of NGC 7793's stellar population. A CMD is shown in figure 6.25. One can see that the photometric depth of the data is around 24 magnitudes, if one allows a maximum magnitude error in the order of 0.3 magnitudes. In case of allowing higher photometric errors up to 0.5 magnitudes the data reaches down to 26 magnitudes. Isochrones plotted inside this figure show that the data at hand cannot reach down to the very old and low metallicity populations (stellar ages around 10 Gyrs, $z=0.001$) but it still allows the mapping of stars with ages around 1 Gyr. In order to deal with the effects of high photometric errors star count maps are produced for two different V-band absolute magnitude ranges. The $20 < V < 24$ range represents the result for the "photometric error below 0.3 magnitudes"-condition while the $20 < V < 26$ range includes nearly all detections. For both conditions the color range is set to $-0.5 < B - V < 0.5$ separating the blue (young) stars from the red (older) ones having $1.3 < B - V < 2.5$. These limits were set according to isochrones in order to distinguish primarily between very young stars that characterize recent star formation regions and middle aged stars which formation took place 1-2 Gyrs ago.

Examining the blue star count maps (figures 6.26 and 6.27) reveal a significant rise in the number of background sources between the maps which resemble different error regimes. To explain this, one should keep in mind that rising the absolute magnitude limit from 24 to 26 will significantly introduce a new number of sources which are not of stellar origin. These are mostly unresolved background galaxies. The use of the program *GalaxyCount* (Ellis & Bland-Hawthorn 2006) allowed me to quantify their influence. Unfortunately, there is no model for the V-band present but for the B-band the number of background galaxies calculated rise from 204 ± 19 (faintest magnitude 24) to 1536 ± 54 (faintest magnitude 26) considering the whole field of view. For the V-band this rise is expected to be at least identical but likely to be a bit stronger. Therefore, the sudden rise in stellar counts is not alone due to new stellar detections of NGC 7793 stars. Instead, the majority of this increase is due to background sources. This is also underlined by the characteristics of a smooth emersion of these new detections in the whole field around NGC 7793.

Apart from this general noise the deeper maps show other interesting features, that cannot be explained by the constant rise of background objects. Most of the high star count regions (blue dots in all maps) are concentrated in a very small ring around NGC 7793's center. This is surely caused by the typical behavior of

the stellar counts to rise towards the central part of the galaxy. But considering this structure as the normal behavior, there is still one larger blue tail visible in the (south) eastern part. Even in the less deep maps this structure is detectable. Although one would not consider it as a high count region in these maps any more.

Another interesting feature is a slight bump in the outer north-west part of this galaxy. While the overall structure in the star count maps could be described by a larger ellipse there is this small deviation from this form visible. A small hint for this structure can also be seen in the less deeper maps. After a drop in star counts there is a small rise visible in 2-3 intervals outside of the main part of the galaxy. To analyze this asymmetry further and in addition to limit the influence of background objects another star count map was created with a magnitude limit of $20 < V < 25$.

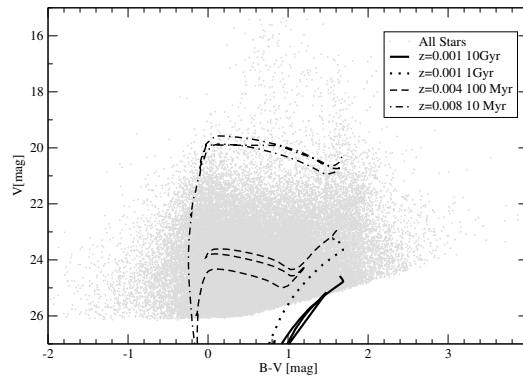


Figure 6.25: Color magnitude diagram for NGC 7793

The star count map for red stars of ages around 1 Gyr are shown in figure 6.28 and 6.29. Comparing the first two maps of figure 6.28 with the two of figure 6.29, which differ again only in the chosen absolute magnitude range, one sees that in contrast to the blue maps from figure 6.26 the rise of background objects is significantly smaller. Hence, the proportion of background objects is smaller in this CMD regime. Examining the galaxy's center one detects again the similarities to the data of NGC 300 and M 83. The central parts of the galaxy show the usual drop in stellar counts caused by crowding effects.

The overall distribution of red stars in the galactic disk seems to be very smooth as there is no significant asymmetry of high star count areas visible. Very interesting for this study is again a small overdensity in the south-east (still near the galaxy's center) and another overdensity in the south (west) that are visible in both of the deeper star count maps. These overdensities could possibly be hints

of tidal tails in NGC 7793's red star distribution. At this point it is important to note that the south east overdensity could be the red counter part of the tail seen already in the blue maps as it occurs nearly at the same position.

6.5.2 Data Mining Results Using a Fuzzy C-Means Clustering

After finding some interesting structure in the star count maps the next step was to use the fuzzy c-means clustering to see if it could recover these parts. As one could see from figure 6.30 and 6.31 the galaxy is presented by a central ellipse of many clusters (between $x:3300-4900$ and $y:3000-4500$). This is in very good agreement with the star count maps, where the central structure was also seen. But in contrast to the small anomaly in the south-east here a multitude of clusters is present in the eastern part beside the central elliptical structure.

An asymmetry between the east and western part of the galaxy is therefore clearly visible as the western side does not show any structure. Looking at different runs the similarities of the individual clusters are very striking, leading to the conclusion that this asymmetry is indeed a real feature. In all runs the structure of the central ring with an additional "arm" in the eastern part is clearly visible. In order to characterize these feature(s) in more detail, table 6.3 contains the important properties of these clusters. The table is a summary of different clustering runs where duplicate detections have been sorted out. In addition to this the ring-like cluster structure representing the central part of the galaxy has also been removed. Also clusters with less than 9 members are removed from this list because this could be spurious detections (see also chapter 5.3.2).

The main result of this table is that the structure is composed of clusters of two similar groups. On the one hand composed of blue stars which have colors around 0.2 and 0.3 mag and on the other hand of more "intermediate color" stars with colors of about 0.7 mag.

Some single clusters are found at the position of the other south (west) feature of the the star count maps.

Apart from these structures there are no larger clusters, meeting the at-least-9-members requirement, visible outside. Even the bump seen in the north-west part of the galaxy on the blue star count maps is not visible in the data mining results. This is not surprising as the bump was not an overdensity in the sense of a high count region. Instead it is the deviation of a smooth blue star distribution from the elliptical form representing the central part of this galaxy. Considering that the fuzzy c-means algorithm used for the search is limited by a maximum cluster distance δ , large scale asymmetries may not be detected as a single large cluster. Instead if there are enough members to build up several smaller clusters they could be detected as a multiple cluster feature. Nevertheless, the resultant maps of the clustering runs do not show a noticeable asymmetry in the cluster positions in the

north east part. This could be due to a deficiency in the number of possible cluster members to build up many separated clusters. In the concerning region only four to five clusters are detected but they tend to be a part of the central cluster feature. This number is also much smaller than the number of clusters detected in the east arm feature which is on the average 15 per run.

6.5.3 Comparison to Other Studies

NGC 7793 is, in contrast to the other galaxies, not a grand design spiral. Instead it is a so called “flocculent” spiral. This means it does not show the symmetry of a grand design spiral that manifests itself mostly in two characteristic, highly symmetric, spiral arms. In contrast the many spiral arms of NGC 7793 are very fragmented and patchy even in the near-infrared (Elmegreen 1981). It is argued that this appearance probably reflects the presence of many HII regions, OB complexes and super giant associations. While there exists no available publication mapping all the positions of observed HII regions in NGC 7793 there are several estimations that show that NGC 7793 indeed contains a lot of them. Chun (1983) estimated the number of HII regions to be over 300, while Pietrzyński et al. (2005) detected 148 OB associations of which 104 lie near or in HII region candidates, which were detected on $H\alpha$ images. Pietrzyński et al. (2005) also compared the number of OB associations to other galaxies and found that NGC 7793 has one of the highest number of such associations observed so far. Although, due to its distance of about 3.91 Mpc (Karachentsev et al. 2003), they argued that this is only a lower limit as they could have missed many small-scale associations. Also in agreement with the large number of OB associations in this galaxy are recent findings of Dicaire et al. (2008) who examined deep $H\alpha$ observations and discussed the origin of the HII ionizing sources. Due to the $H\alpha$ extent which is smaller than the HI extent, they came to the conclusion that the ionizing sources are probably mainly internal.

The HI disk of NGC 7793 has already been examined by Carignan & Puche (1990) and is also confirmed by the $H\alpha$ measurements of Dicaire et al. (2008) with the result that it extends the optical diameter of the galaxy by a factor of 1.5. The rotation curve derived from this study revealed a declining trend in the outer parts and could in parts be explained by the absence of dark matter halo. Nevertheless, they showed that a model containing a small dark matter halo would better reproduce the measured rotation curve. The maps also showed a warp in the HI profile and some hints of non-circular motions on the north side of the minor axis which, according to Carignan & Puche (1990), could be a hint for an interaction with another group member a long time ago. At present there exists no evidence for any interaction between the Sculptor Group members (Puche & Carignan 1991).

| Cluster No. | X-Center | Y-Center | B [mag] | B-V [mag] | WCV |
|---------------|----------|----------|---------|-----------|--------|
| 1 | 3645 | 3221 | 25.70 | 0.743 | 0.0092 |
| 2 | 2868 | 3306 | 25.54 | 0.815 | 0.0095 |
| 3 | 2760 | 3680 | 24.31 | 0.131 | 0.0093 |
| 4 | 3144 | 3525 | 24.05 | 0.432 | 0.0089 |
| 5 | 2722 | 4018 | 24.91 | 0.305 | 0.0085 |
| 6 | 2894 | 3453 | 24.81 | 0.418 | 0.0070 |
| 7 | 3290 | 3710 | 23.10 | 0.288 | 0.0086 |
| 8 | 2867 | 3497 | 25.06 | 0.684 | 0.0080 |
| 9 | 2633 | 3663 | 24.68 | 0.352 | 0.0083 |
| 10 | 2767 | 3827 | 25.38 | 0.703 | 0.0093 |
| 11 | 3233 | 3711 | 23.53 | 0.424 | 0.0080 |
| 12 | 2671 | 3843 | 24.55 | 0.271 | 0.0079 |
| 13 | 3045 | 3897 | 24.32 | 0.526 | 0.0083 |
| 14 | 2781 | 3795 | 25.47 | 0.775 | 0.0102 |
| 15 | 2720 | 3665 | 24.97 | 0.566 | 0.0100 |
| 16 | 2938 | 3445 | 24.96 | 0.161 | 0.0101 |
| 17 | 3654 | 3161 | 25.69 | 0.775 | 0.0092 |
| 18 | 4312 | 3360 | 25.30 | 0.501 | 0.0082 |
| 19 | 4131 | 3330 | 24.96 | 0.528 | 0.0083 |
| 20 | 4308 | 3306 | 25.76 | 0.690 | 0.0106 |
| Noise Cluster | - | - | - | - | 0.678 |

Table 6.3: Cluster properties in the NGC 7793 dataset. This list contains only clusters which have at least 9 members and are not part of the elliptical central region. The first part of this table shows clusters of the “eastern-arm” and the second consists of clusters in the south (west) part. The noise cluster WCV has been given as a reference in order to show the difference in the WCV value of objects not related to each other.

As shown in the previous paragraphs there were some interesting features visible in the star count maps and also in the results of the clustering runs. The most prominent feature was the asymmetry between east and west side of this galaxy. Especially the presence of the arm-like structure is a notable difference. Due to NGC 7793's nature it could either be one or even many smaller spiral arms or a tidal tail. The cause for such asymmetry may be an interaction with another group member or satellite as it was already proposed by Carignan & Puche (1990) to explain the warp and the non-circular motions. An asymmetry is also seen in the surface photometry carried out by Carignan (1985). He mentioned that there is some kind of fainter plateau seen in the isophotal maps of the eastern part of this galaxy and concluded that this must either reflect a region of higher absorption or a departure from the circular symmetry. This asymmetry between east and west part is clearly visible in the east-west comparison of the luminosity profile of the major axis. Here the west part is noticeable fainter at a distance between 150 and 250 arcseconds. Considering the distribution of OB associations as reported by Pietrzyński et al. (2005) these do not show such an east west asymmetry.

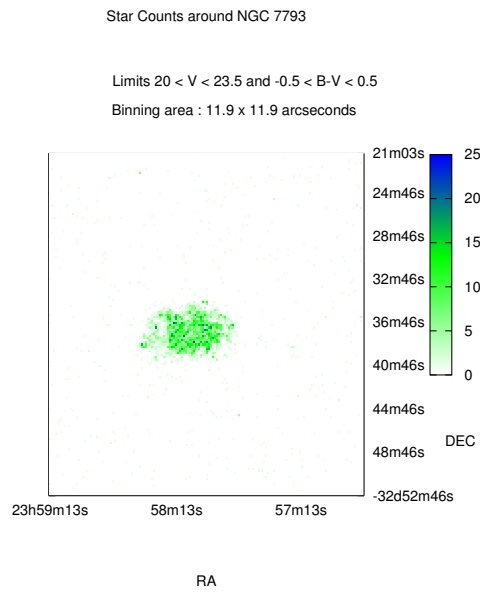
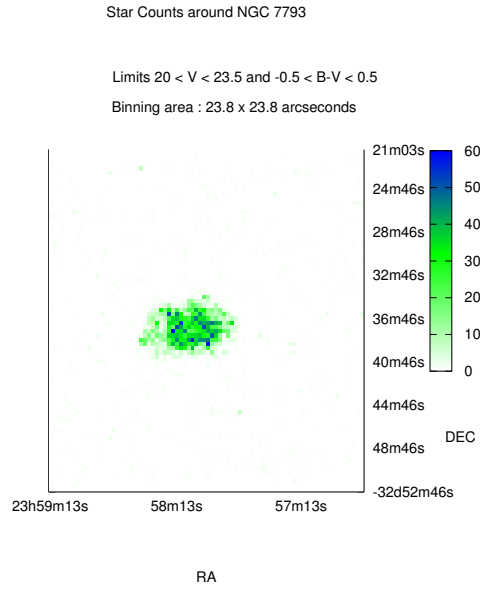


Figure 6.26: Star count maps for the blue stars in NGC 7793. The maps are drawn using detections with a magnitude error not larger than 0.3 mag. The bottom map shows the same data using a smaller binning area.

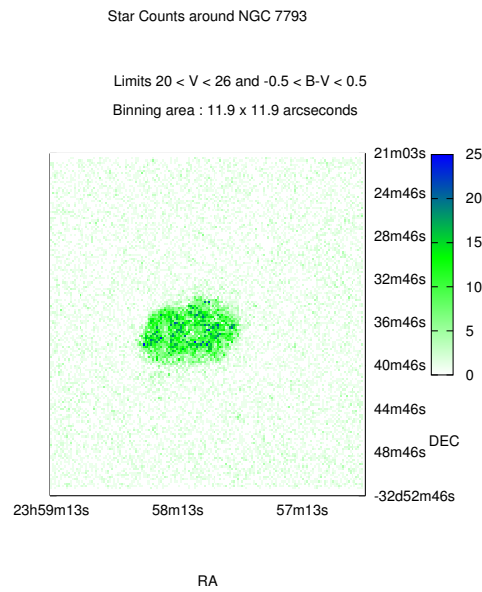
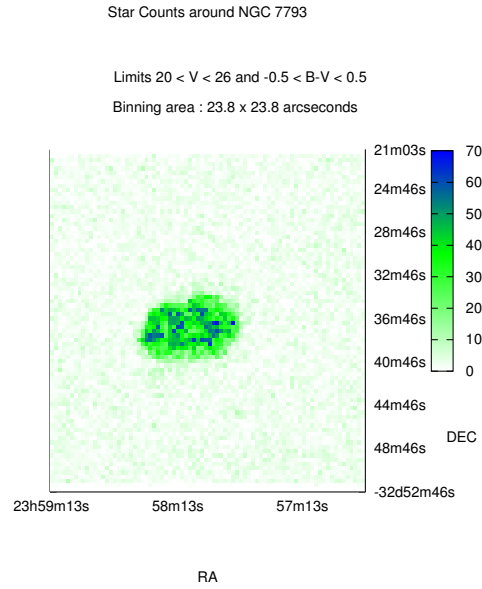


Figure 6.27: Star count maps for the blue stars in NGC 7793. The maps are drawn using detections with a magnitude error not larger than 0.5 mag. The bottom map shows the same data using a smaller binning area.

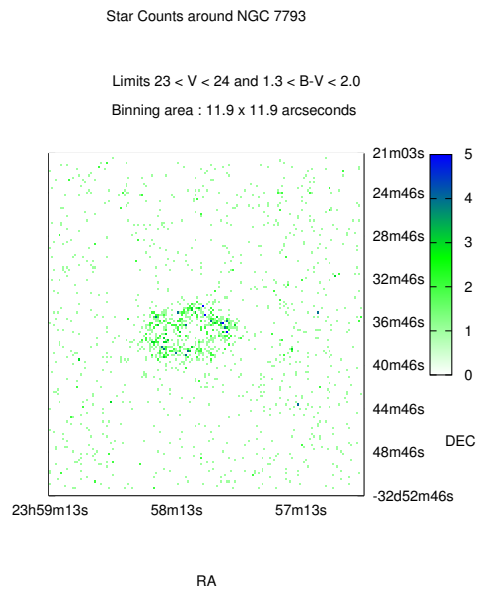
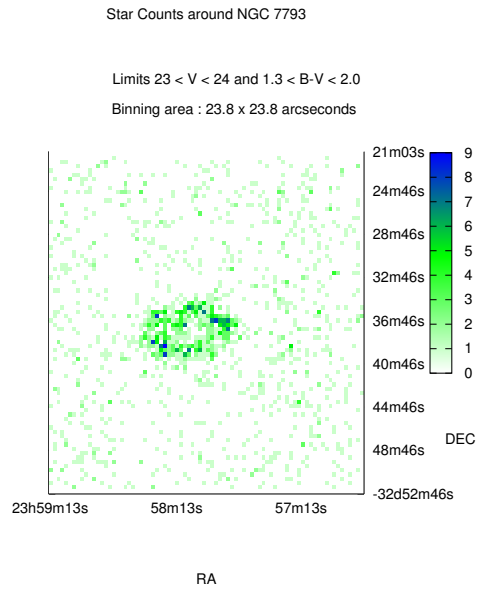


Figure 6.28: Star count maps for red stars in NGC 7793. The maps include detections with a magnitude error up to 0.3 mag. The bottom map shows a more detailed view using a smaller binning area.

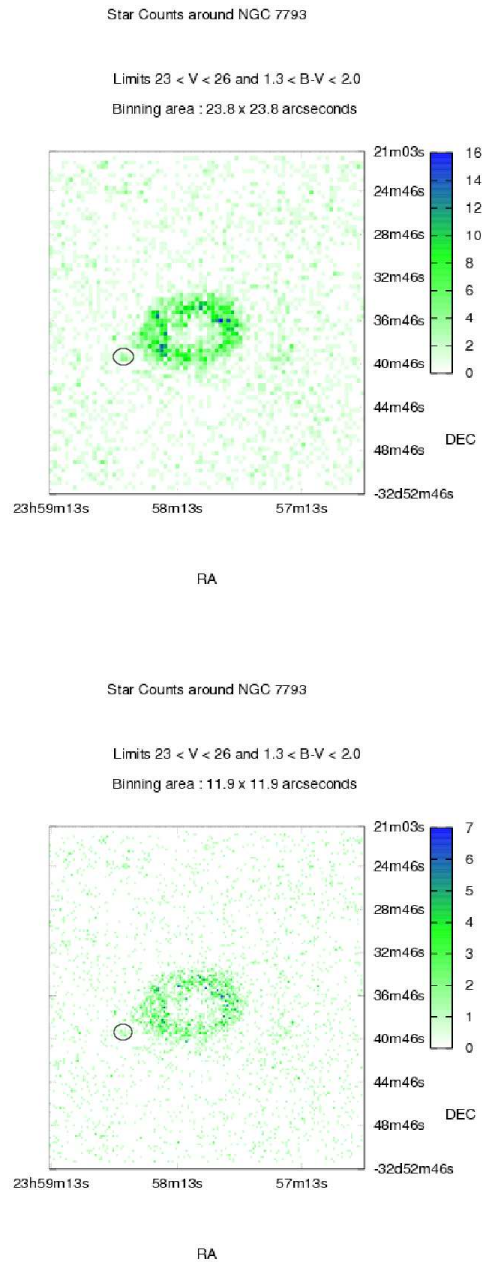


Figure 6.29: Star count maps for red stars in NGC 7793. The maps include detections with a magnitude error up to 0.5 mag. The bottom map shows a more detailed view using a smaller binning area. The interesting overdensity is marked by an ellipse in both plots.

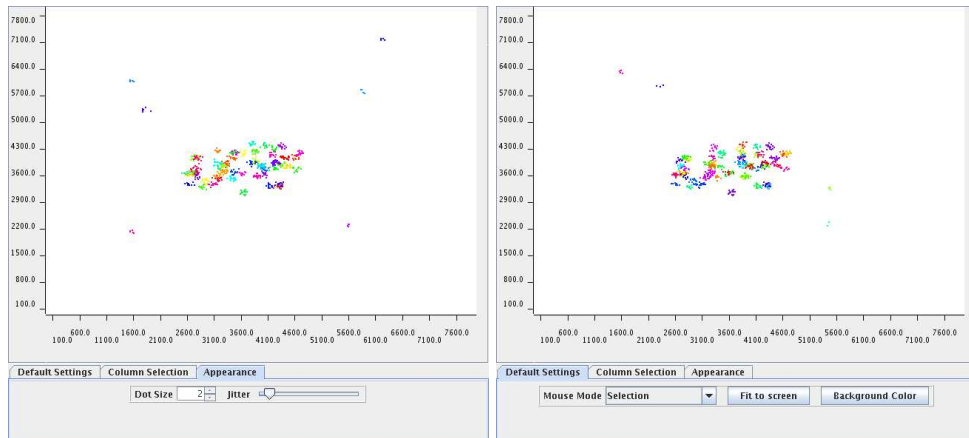


Figure 6.30: Examples of two maps from the fuzzy c-means clustering runs of the NGC 7793

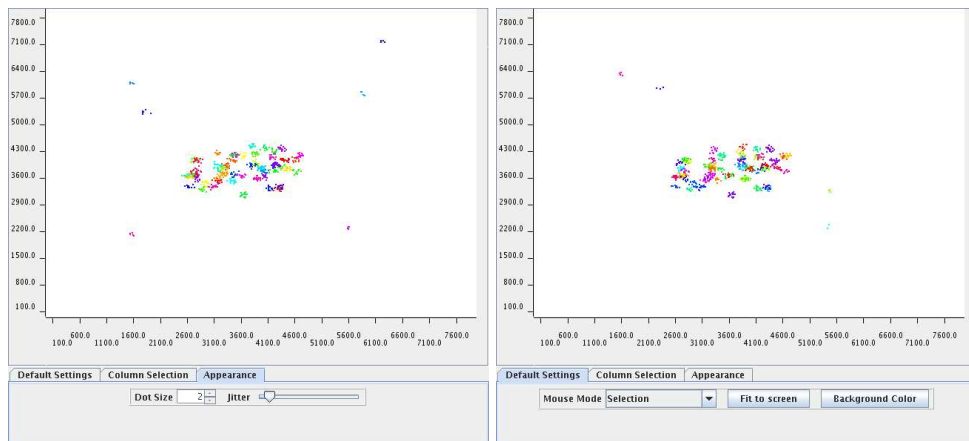


Figure 6.31: Other examples of two maps from the fuzzy c-means clustering runs of the NGC 7793

Results & Summary

This chapter will summarize the work and discuss the results derived in a broader context. It will be split up in two parts which deal on the one hand with the “technical” part which focuses on all kinds of technical aspects of this work and on the other hand with a “scientifically” part which places this work in its broader scientific background. The general scientific background was already introduced in chapter 2 and therefore this second part will focus primarily on the results and their possible implications.

7.1 Technical Results

Referring to the technical aspects of this work two fields were very important. The first challenge was the reduction of the data sets of the ESO/MPG WFI imager. Chapters 3 and 4 dealt with this problem and described in detail the procedures carried out to obtain scientific valuable images from the unprocessed raw data.

Although the reduction of wide field imaging data is not new to astronomy and has been carried out before, it is still challenging if large objects are observed. This is true even if one has a reduction pipeline like *THELI* at hand. No pipeline can be designed to cover every single application in mind. Here the automatic routines dealing with astrometry and sky-reduction have reached their limits. Most algorithms cannot distinguish between artifacts like saturated stars and very large objects like nearby galaxies. In case of the astrometry then too few or too many stars may be found. This not only increases the calculation time but it may also lead to (partially) unusable solutions like the one presented in figure 3.4. In such a case using other astrometric references or adopting the order of the astrometric solution can circumvent the problem. The sky subtraction is mostly influenced by the presence of large objects like galaxies that outshine the real background. This

problem was handled using a new script which takes into account the position of such large objects when calculating the sky background. Therefore the reduction of the raw data could be handled with an acceptable portion of manual work like inspecting the reduced frames and altering some scripts and options. This was described in detail in chapter 3.

This done, the next step was to prove that the co-added frames are of general scientific value. Especially, for the scientific work that should be carried out. To show this, chapter 4 discussed in detail the illumination problem(s) of the ESO/MPG wide field imager and the photometric quality of the *THELI*-Pipeline. It was shown that the co-added frames could be transformed to a standard magnitude system and that these transformations were acceptable up to 0.08 magnitudes (including the illumination pattern and errors of the global solution itself). There were no significant internal variations detected in the photometric quality and all photometric results were in agreement with previous published work. For example, the NGC 300 data set was compared and calibrated using the work of Pietrzyński et al. (2002) and Graham (1981) and NGC 7793 produced results (zero-points) in agreement with published ESO zero-points and transformation equations¹. In addition to this it was shown that the illumination problem of the WFI is not as big as expected in the final co-added frames. The illumination map presented in figure 4.1 and discussed in chapter 4.3 shows a possible deviation of 0.03 magnitudes much smaller than about 0.08 magnitudes reported first for the error due to the illumination problem alone. The reason for this might be a time dependence of this effect likely caused by baffle changes which have occurred since the first observations of Koch et al. (2004).

This said, it was concluded that the data reduction of WFI data was possible and can be carried out with an acceptable precision of the stellar photometry for this study. While having a pipeline like *THELI* at hand is in principle not mandatory it simplifies and accelerates the reduction of such large data sets a lot. Although some modifications had to be made and the results had to be checked it should be pointed out that the original modular design of *THELI* has shown its success.

The other technical challenge was the interpretation of the data. This includes finding a fast and efficient way to search for candidates of tidal tails or stellar streams. A detailed discussion on possible methods was presented in chapter 5. Throughout this work three forms of data representation techniques were used:

The first form of data representation was the color-magnitude diagram (CMD) and also the Hess diagram (HD). These two are long known resources in astronomy to interpret the stellar population of galaxies. While the CMD shows every single star, the HD bins the data of a CMD and shows the number of stars in the

¹<http://www.ls.eso.org/lasilla/sciops/2p2/E2p2M/WFI/zeropoints/>

bins.

The second one was the star count map. Such maps are a very good choice for representing the spatial distribution of features seen in the CMDs and help to identify streams or tails which turn out to be over-dense regions. The use of star count maps is not new to astronomy, either. It was already used by different authors e.g. Ibata et al. (2001) or Bland-Hawthorn et al. (2005).

The third and new method in finding candidate streams and tails was the use of the fuzzy *c*-means clustering. While the fuzzy *c*-means is a long known clustering technique used in data-mining, to my knowledge it was not used in the search for stellar streams or tidal tails before. It was shown that this technique is in principle very useful in finding small scale structures that can be represented by a single cluster of similar stars. In comparison to the star count method mentioned above the cluster search also visualizes the spatial distribution of similar objects. But in contrast to the star count maps it is un-supervised in the sense that no a priori assumption is made about the values of the attributes of a cluster. While each star count map is created with a pre-defined stellar population and photometric error in mind the fuzzy *c*-means only needs an estimation for the number of clusters. As it was shown in the analysis of NGC 7793 this uncovered a detailed view of a possible candidate stream or asymmetry that was not very spectacular and extensive on star count maps. In case of M 33 it was also shown that the clustering is very sensitive to (compact) star forming regions as the large majority of clusters found represent already known HII regions or parts of the spiral arm. Unfortunately, in M 83 the cluster analysis revealed only the structure of M 83 without any sign of the structure seen by Malin & Hadley (1997). Nevertheless, this is unlikely to be a limitation of the method. Even the star count maps created were not able to reveal this structure. Therefore, as it was already discussed in chapter 6.3, it is more likely that the photometric data did not reach the photometric depth necessary to reveal this structure.

To summarize this, the clustering analysis is a successful additional tool in the search for substructure in a galaxy. Subsequent clustering runs can be used to detect different small scale structures. The advantage of this method is its little dependence on the structure to reveal, while its limitation is the extension of the structure. In the standard implementation of fuzzy *c*-means algorithms it might not be possible to detect larger scale structures. Although hints for a truncation of the RGB disk as it was seen in case of NGC 300 might be identified by an equal spatial distribution of clusters. So even some large scale structures can be revealed.

7.2 Scientific Results

From the scientific point of view the interesting results of this thesis are:

- The detection of the truncation in the RGB disk of NGC 300
- The arm-like substructure in the East of NGC 7793
- The non-detection of substructure in M 83
- Wealth of clusters found in M 33 corresponding with spiral arms and HII regions
- The spiral arm asymmetry of M 33 is also seen in the stellar distribution

The truncation of the RGB disk in NGC 300 is a real surprise because in most works published so far the disk of NGC 300 was described as a true exponential one, without having any irregularities like a truncation. This analysis has shown that this view has to be changed if one looks at the RGB stars lying in the disk. In general, truncations are not an uncommon feature of disk galaxies. A systematic study on disk galaxies carried out by Pohlen & Trujillo (2006) and Erwin et al. (2008) showed that about 42 % of the spirals are of a “down-bending” type (second exponential slope is steeper than the first) like the profile found here in case of NGC 300. The remaining spirals may be of a single exponential type, of an “up-bending type” or cannot be fitted by a two exponential profile. Therefore, while truncations themselves are not new to astronomy the detection of such in NGC 300 is a new result. An important difference between the truncation found in this work and the ones described by Pohlen & Trujillo (2006) is found in the surface brightness. Although the surface brightness (for type II profiles) at the break radius in the R-band filter spans over a wide range of values from 22 - 25.5 mag/arcseconds², the feature recovered here is less luminous than this (about 25.9 mag/arcseconds²). Therefore it seems likely that this structure is not a typical truncation.

In the case of M 83 no substructures were found but this result must be handled with care. As was shown, the photometric depth of the images is only about 24.5 magnitudes. Considering the distance of M 83 this might simply be not deep enough. Especially, if one takes into consideration that with the report of a giant arc by Malin & Hadley (1997) some hints for substructures in this galaxy already exist. Unfortunately, in this analysis no sign of this arc is seen in the stellar distribution. Instead of this, binned images revealed parts of the stream in surface brightness at the expected positions. From this analysis the age of the stars in this arc is expected to be around 5 Gyr.

In M 33, however, the star count maps did not show signs for tidal tails but the cluster analysis showed many clusters throughout the field. In nearly all cases these structures could be identified to lie near HII regions and inside the spiral structure. In addition to this most of these clusters have bluish colors which is normally a sign for star forming regions which typically occur inside spiral arms.

In NGC 7793 the star count maps showed an overdensity in the east part of this galaxy. This overdensity was then verified by the clustering analysis. Additionally, this analysis revealed a complete arm-/stream-like structure in the eastern part instead of a small overdensity of elliptical shape seen on the star count maps. This asymmetry might be another hint for an interaction of NGC 7793 and hence supporting the interaction theory of this galaxy suggested by Carignan & Puche (1990).

To finally summarize this work, it can be said that in three out of four galaxies some kind of substructure was found. But these substructures are very different from each other. While in the case of NGC 300 the truncation of the RGB disk is a large scale feature, the arm-like structure of NGC 7793 is of a smaller scale and therefore of a completely different type. In comparison to this the clusters representing the HII regions in the M 33 dataset are then the smallest structures found in this work.

The findings of this work could also be related to the results of newer numerical simulations like the ones carried out by Bullock & Johnston (2005), Font et al. (2006b), Font et al. (2006a) or Fardal et al. (2007). In these simulations the authors simulated merging events of progenitor satellites with Milky Way - type galaxies. The main conclusion of these studies was that numerical simulations adopting the hierarchical stellar halo formation scenario are successful in describing the current observational situation of streams and substructure of the Milky Way and the Andromeda galaxy. For example, Font et al. (2006b) and Fardal et al. (2007) calculated more detailed models for M 31 and were able to narrow down the parameter space (in mass and orbital parameters) of the progenitor satellite that caused the giant stellar stream. The simulations carried out by Fardal et al. (2007) go even further in explaining and connecting other substructures, like the north-east shelf, to the progenitor of the giant stream by introducing the possibility of building up a shell system. Observational evidence for such a shell system in M 31 was given by the detection of a kinematically cold stellar population made by Gilbert et al. (2007).

Additionally, all these simulations agree on the fact that visible streams, like the giant stellar stream, should exist only in the outer parts of the halo while the inner halo should appear largely undisturbed. This is due to the fact that most major merging events should have taken place a long time (~ 9 Gyr) ago so that all stream like features have already been smeared out. Only the most recent merging (1-5 Gyrs ago) events may still be visible in the outer parts at a distance

| Galaxy | Type of structure found | Distance from center | estm. surface brightness |
|----------|--|----------------------|---|
| NGC 300 | truncation of disk | ~ 8.25 kpc | $\sim 25.9 \pm 0.2 \mu_r / \text{arc}2\text{sec}^2$ |
| NGC 7793 | arm or stream like structure | ~ 6 kpc | $\sim 28.9 \pm 0.3 \mu_v / \text{arcsec}^2$ |
| M 83 | arc/stream in surface photometry | ~ 23 kpc | $\sim 24.9 \pm 0.2 \mu_r / \text{arcsec}^2$ |
| M 33 | several clusters tracing HII regions and spiral arms | - | - |

Table 7.1: Summary table for the different substructure types found in this analysis

larger than 20 kpc.

This result is slightly contrary to the findings of this work. Surely, no substructure was detected in the inner-most parts (< 5 kpc, a radius given by Font et al. (2006a) for the most metal poor stars), but it must be noted that the inner-most regions (< 2 kpc) could not be resolved due to crowding effects. However, the arm-like feature in NGC 7793 is only about 6 kpc away and the truncation in NGC 300 lies at a distance of about 8.75 kpc. Therefore, these detections are made at a significantly smaller distance than predicted by the models. A possible explanation for this might either be the fact that the host galaxies are less massive (about $10^9 - 10^{10} M_\odot$; Puche & Carignan 1991) than the ones used in the simulations (about $10^{11} - 10^{12} M_\odot$) or that they have an unusual low mass dark matter halo. This would especially explain such discrepancy in case of NGC 7793 as this galaxy is already known to have a declining rotation curve according to Carignan & Puche (1990).

Another possible interpretation for the findings of this work comes from the appearance of the structures itself. The simulations especially that of Fardal et al. (2007) showed that the giant stellar stream of M 31 is a feature that arose during the first encounter of the progenitor with the host galaxy. The shell system instead is a result of successive approaches in which it is very likely that the progenitor gets finally dissolved. The building of shell system also exhibits some kind of symmetry and would therefore be a good explanation for an observable large scale structures that might still be visible for a longer time in contrast to a stream. This in mind one could interpret the large scale structure seen in NGC 300 as a sign for a merger very long ago ($\gg 5$ Gyr) while the arm like structure in NGC 7793 would then be a hint for a merging event that has taken place within the

last 5 Gyrs. While some of the blue star count maps seem to suggest a shell-like distribution the red star count maps do not. Therefore, only a more sophisticated search including better resolution in the central parts of NGC 7793 and kinematic information of the stars in question could give an answer to the question if a re-scaled or re-defined model (in comparison to that suggested by Fardal et al. 2007) is necessary.

7.3 Final Result and Outlook

It is clear that the analysis of only four galaxies cannot give a complete answer or theory to the formation of galaxies. This is especially true as the substructures found in these four galaxies greatly differ from each other. A complete theory of galaxy formation must explain on the one hand such large scale structures like the truncation of the RGB disk and on the other hand such arm-like features like the one found in NGC 7793 or the arc in M 83. Finally, the absence of substructure like streams or tails in M 33 must also be explained. Therefore, even in this small sample of only four galaxies, it seems to be unlikely that the use of either mergers or gas accretion including secular processes alone will be sufficient to explain all these findings. In contrast to the presentation of chapter 2 not a single model is the ultimate answer to galaxy formation and evolution.

As a matter of fact far more studies will have to be done to get a good understanding of galaxy evolution on smaller scales. While the theories so far are able to reproduce the large scale structure of the universe and to explain the existence and basic evolution of galaxies, they cannot predict all structural features within a single galaxy. Surely, the inclusion of mergers and near companions may help to explain findings of tidal tails (White 1978; White 1979; Choi et al. 2007) but there is the relatively undisturbed M 33 which lies near to a very massive galaxy (M 31) and apart from its spiral structure it has a relatively smooth halo of RGB stars. This is surprising because it is assumed that the halos of both galaxies are likely to overlap (Ibata et al. 2007). If companions or satellite galaxies are assumed to be the major cause of tidal tails it still stays unclear why no sign of such a tidal tail or substructure is seen in M 33's halo. While one might argue that the non-detection is caused by the small coverage (only 5 kpc) of this study it should be pointed out that a larger survey carried out by Ibata et al. (2007) did not find signs for a stream of stars in the M 33 halo, either.

To explain disk truncations like the one seen in NGC 300 two different types of models were proposed so far. On the one hand models that deal with angular momentum conservation in the proto-galactic cloud (van der Kruit 1987) or angular momentum cut-off in the cooling gas (van den Bosch 2001). And on the other hand models that use thresholds in the star formation process(es) to explain these

findings (Kennicutt 1989; Elmegreen & Hunter 2006). Both views are supported by numerical models e.g. Debattista et al. (2006) or Roškar et al. (2008) which have one important ingredient in common. They both must use secular processes to explain the break in the disk profiles. But as pointed out earlier the expected surface brightness value of such truncations at the break radius is normally smaller than what was found in NGC 300 in this study.

It is also interesting that in the case of NGC 300 the truncation was seen at a radius at which the warp of the HI gas sets in. Until now the physics of warps is not completely understood (Binney 1992) and several models are able to explain the existence of such warps. Some models describe the warps as being the result of forces exerted by the halo (potential) on the disk of spiral galaxies (Sparke & Casertano 1988; New et al. 1998) while hydrodynamical models are able to explain warps by the cooling of the gas (Katz & Rix 1992) or interactions of gas clouds among each other (Quinn in Casertano et al. 1991). In addition to the causes described by these models warps may also be explained using in-falling gas (Toomre 1983; Toth & Ostriker 1992) or due to the tidal fields of companions or intruders (Hunter & Toomre 1969). Additionally, including also the ideas of Fardal et al. (2007), namely the building of a shell system during successive encounters of the progenitor with the host galaxy, the possibility remains that such truncation might also be caused by the (former) presence of a companion or dark halo around NGC 300. This would lead to a situation in which "merging" and/or accretion plays an important role in order to explain the truncation. This in mind, it seems to be that in two out of four galaxies (M 83 and NGC 7793) mergers played an important role in creating the substructure while in case of one galaxy (NGC 300) secular evolution would still be an option even if there are possibilities to attribute the structure to a merging scenario.

Therefore, mergers or secular processes alone do not give a full description of galaxy formation. Until now, both models should be considered as important for galaxy formation and it is likely that a combination of both models is necessary to describe the formation and evolution of galaxies. In such "unified" model mergers are likely responsible for the formation of galaxies in the past but secular effects are important for describing the evolution of the same galaxies afterwards. Models dealing with both processes (merging and secular evolution) have already been simulated by Tissera et al. (2006). In cases where galaxies are not isolated, like in larger galaxy groups, merging events are likely to interrupt the evolution described by the secular models. Therefore, to answer all these still open questions and to quantify how often merging events are important for the later evolution of a galaxy, more detailed studies will be necessary.

In this work it was shown that the use of wide field photometric imaging data is a good tool to get an overall picture of a galaxy. The only problem in using such data is that for galaxies at larger distances the resolution sets limits to the

structures that can be recovered. The photometric depth of the images is still another problem. As shown, for some structures like in NGC 300 and NGC 7793 the photometry of the RGB tip requires images of a large photometric depth. To archive this photometric depth in optical images a large amount of observation time is needed. But with the building and availability of CCD detectors in the infrared larger photometric studies or surveys will become possible in the J- and Z-band. In case of solar metallicity the RGB tip for M 83 in the Z- and J-band would be at 23.49 mag and 23.31 respectively. To study the RGB tip images with a photometric depth of only 24.5 mag needed instead of about 25 mag in the I-band (or 26 mag needed in the V-band).

Additionally, the amount of data (number of detections) requires some automatic finding procedures. The creation of star count maps surely is one basic tool to interpret the data but as it was shown the clustering and data-mining tools are very promising approaches in resolving the substructure of galaxies. Un-supervised methods like the clustering algorithms can be used to get a first overview. Detailed studies of the structures found with this method should characterize the type of the structure. These findings can then be applied to refine the search techniques. In case of the clustering algorithms one could try to change the distance function to a more appropriate one. In this work a very simple approach using an euclidian metric was used in order to recover structures with a (circular) spatial central core of similar objects. As it was also shown this worked properly.

If detailed studies or simulations reveal a better description, e.g. for the spatial extension of stellar streams, then a new distance function can be calculated and used. Surely the clustering then will be blind to any non-stream detections but the number of streams per galaxy can be quantified that way. Further distance functions for the clustering algorithms may also be suggested/calculated to find other types of substructure like globular clusters, galactic bars and so on. Several different runs may finally help quantifying the occurrence and the frequency of substructures that galactic formation and evolution theories have to deal with.

Appendix A

List of Images Used for Co-added Frames

This appendix gives a list of all raw image frames used in the final co-added frame that were reduced by myself. These names are consistent with the ESO-Archive naming-scheme. Only raw science observations are given. Each of these images contain all 8 CCD frames that are separated from each other in the first step carried out by the reduction pipeline.

A.1 M83 V-band images

| | |
|----------------------------------|----------------------------------|
| WFI.2001-02-11T08:17:38.285.fits | WFI.2002-06-15T02:39:32.962.fits |
| WFI.2001-02-11T08:22:31.526.fits | WFI.2002-06-15T02:46:22.738.fits |
| WFI.2001-02-11T08:27:24.250.fits | WFI.2002-06-15T02:53:12.336.fits |
| WFI.2001-05-29T23:56:04.733.fits | WFI.2002-06-15T02:59:54.266.fits |
| WFI.2001-05-29T23:58:51.744.fits | WFI.2002-06-15T03:06:38.943.fits |
| WFI.2001-05-30T00:03:01.958.fits | WFI.2003-03-29T07:37:04.691.fits |
| WFI.2001-05-30T00:07:11.395.fits | WFI.2003-03-29T08:04:54.713.fits |
| WFI.2001-05-30T00:11:16.080.fits | WFI.2003-03-29T08:22:19.668.fits |
| WFI.2001-05-30T00:15:18.518.fits | |

A.2 M83 R-band images

| | |
|----------------------------------|----------------------------------|
| WFI.2001-02-11T08:38:55.968.fits | WFI.2001-05-30T01:38:44.275.fits |
| WFI.2001-02-11T08:43:46.963.fits | WFI.2001-05-30T01:42:51.898.fits |
| WFI.2001-02-11T08:48:40.291.fits | WFI.2001-05-30T01:47:03.581.fits |

WFI.2001-05-30T01:51:07.920.fits WFI.2002-06-17T03:29:42.309.fits
WFI.2001-05-30T01:55:10.963.fits WFI.2002-06-17T03:36:28.985.fits
WFI.2002-06-17T03:16:06.971.fits WFI.2002-06-17T03:43:10.676.fits
WFI.2002-06-17T03:22:53.832.fits

A.3 NGC 7793 B(new)-band images

WFI.2002-10-10T00:13:08.550.fits WFI.2003-07-30T07:00:21.067.fits
WFI.2002-10-10T00:27:22.506.fits WFI.2003-07-30T07:14:10.415.fits
WFI.2002-10-10T00:41:38.075.fits WFI.2003-09-26T03:43:52.535.fits
WFI.2002-10-10T00:55:57.304.fits WFI.2003-09-26T03:58:19.329.fits
WFI.2002-10-10T01:09:53.101.fits WFI.2003-09-26T04:12:38.927.fits
WFI.2002-10-11T02:51:40.870.fits WFI.2003-09-26T04:26:32.795.fits
WFI.2002-10-11T03:05:32.139.fits WFI.2003-09-26T04:40:27.835.fits
WFI.2002-10-11T03:19:28.799.fits WFI.2003-09-27T03:24:46.407.fits
WFI.2002-10-11T03:33:19.431.fits WFI.2003-09-27T03:38:44.287.fits
WFI.2002-10-11T03:47:06.028.fits WFI.2003-09-27T03:52:42.528.fits
WFI.2002-10-13T03:35:42.209.fits WFI.2003-09-27T04:07:10.702.fits
WFI.2002-10-13T03:49:31.806.fits WFI.2003-09-27T04:21:05.122.fits
WFI.2002-10-13T04:03:41.551.fits WFI.2003-09-29T02:29:30.629.fits
WFI.2002-10-13T04:17:30.851.fits WFI.2003-09-29T02:43:30.612.fits
WFI.2002-10-13T04:31:36.655.fits WFI.2003-09-29T02:57:36.399.fits
WFI.2002-10-27T02:47:46.582.fits WFI.2003-09-29T03:12:03.940.fits
WFI.2002-10-27T03:01:47.317.fits WFI.2003-09-29T03:25:53.636.fits
WFI.2002-10-27T03:15:36.145.fits WFI.2003-09-30T01:21:00.079.fits
WFI.2002-10-27T03:29:46.659.fits WFI.2003-09-30T01:34:49.557.fits
WFI.2002-10-27T03:43:32.629.fits WFI.2003-09-30T01:48:43.537.fits
WFI.2003-07-30T06:18:22.471.fits WFI.2003-09-30T02:02:35.079.fits
WFI.2003-07-30T06:32:17.177.fits WFI.2003-09-30T02:16:46.742.fits
WFI.2003-07-30T06:46:08.151.fits

A.4 NGC 7993 B-band images

WFI.2002-07-06T09:06:42.508.fits WFI.2002-07-12T07:31:40.918.fits
WFI.2002-07-10T07:44:17.288.fits WFI.2002-07-15T07:53:44.025.fits
WFI.2002-07-10T07:58:04.360.fits WFI.2002-07-15T08:21:54.784.fits
WFI.2002-07-10T08:11:53.500.fits WFI.2002-07-15T08:35:41.265.fits
WFI.2002-07-10T08:25:35.908.fits WFI.2002-07-15T08:49:29.585.fits
WFI.2002-07-10T08:39:43.963.fits WFI.2002-07-15T09:03:12.931.fits

| | |
|----------------------------------|----------------------------------|
| WFI.2002-07-15T09:16:57.031.fits | WFI.2002-08-12T09:13:48.817.fits |
| WFI.2002-08-10T08:50:25.119.fits | WFI.2002-08-12T09:27:35.630.fits |
| WFI.2002-08-10T09:04:09.106.fits | WFI.2002-08-12T09:41:19.410.fits |
| WFI.2002-08-10T09:17:53.591.fits | WFI.2002-08-13T08:37:18.256.fits |
| WFI.2002-08-10T09:31:38.209.fits | WFI.2002-08-13T08:51:02.690.fits |
| WFI.2002-08-10T09:45:19.228.fits | WFI.2002-08-13T09:04:48.593.fits |
| WFI.2002-08-11T06:17:50.140.fits | WFI.2002-08-13T09:18:29.400.fits |
| WFI.2002-08-11T06:31:41.515.fits | WFI.2002-08-13T09:32:08.779.fits |
| WFI.2002-08-11T06:45:27.051.fits | WFI.2002-09-28T03:50:39.678.fits |
| WFI.2002-08-11T06:59:05.286.fits | WFI.2002-09-28T04:05:07.479.fits |
| WFI.2002-08-11T07:12:44.810.fits | WFI.2002-09-28T04:19:37.547.fits |
| WFI.2002-08-12T08:46:14.666.fits | WFI.2002-09-28T04:34:00.233.fits |
| WFI.2002-08-12T09:00:03.068.fits | WFI.2002-09-28T04:48:20.857.fits |

A.5 NGC 7993 V-band images

| | |
|----------------------------------|----------------------------------|
| WFI.2002-09-29T00:57:27.825.fits | WFI.2002-10-27T02:17:47.719.fits |
| WFI.2002-09-29T01:11:29.524.fits | WFI.2002-10-27T02:31:31.949.fits |
| WFI.2002-09-29T01:25:52.958.fits | WFI.2002-11-03T01:00:46.153.fits |
| WFI.2002-09-29T01:39:49.803.fits | WFI.2002-11-03T01:14:59.549.fits |
| WFI.2002-09-29T01:53:46.579.fits | WFI.2002-11-03T01:28:59.820.fits |
| WFI.2002-10-10T01:26:12.288.fits | WFI.2002-11-03T01:43:09.855.fits |
| WFI.2002-10-10T01:40:22.950.fits | WFI.2002-11-03T01:57:00.623.fits |
| WFI.2002-10-10T01:54:28.160.fits | WFI.2002-12-11T02:19:17.812.fits |
| WFI.2002-10-10T02:08:24.454.fits | WFI.2002-12-11T02:33:19.934.fits |
| WFI.2002-10-10T02:22:29.664.fits | WFI.2002-12-11T02:47:27.223.fits |
| WFI.2002-10-11T01:39:52.414.fits | WFI.2002-12-11T03:01:39.158.fits |
| WFI.2002-10-11T01:53:47.379.fits | WFI.2002-12-11T03:15:35.836.fits |
| WFI.2002-10-11T02:07:39.709.fits | WFI.2003-07-24T04:25:51.514.fits |
| WFI.2002-10-11T02:21:58.409.fits | WFI.2003-07-24T04:39:45.916.fits |
| WFI.2002-10-11T02:35:50.866.fits | WFI.2003-07-25T03:34:11.672.fits |
| WFI.2002-10-13T01:38:57.804.fits | WFI.2003-07-25T03:47:57.476.fits |
| WFI.2002-10-13T02:02:49.084.fits | WFI.2003-07-25T04:12:17.106.fits |
| WFI.2002-10-13T02:15:30.121.fits | WFI.2003-07-25T04:26:01.481.fits |
| WFI.2002-10-13T02:28:14.794.fits | WFI.2003-07-25T04:39:41.774.fits |
| WFI.2002-10-13T02:40:50.364.fits | WFI.2003-07-30T05:01:51.571.fits |
| WFI.2002-10-13T02:53:24.294.fits | WFI.2003-07-30T05:15:41.622.fits |
| WFI.2002-10-27T00:52:10.500.fits | WFI.2003-07-30T05:29:37.243.fits |
| WFI.2002-10-27T01:06:20.316.fits | WFI.2003-07-30T05:43:23.477.fits |
| WFI.2002-10-27T02:04:02.063.fits | WFI.2003-07-30T05:57:06.822.fits |

| | |
|----------------------------------|----------------------------------|
| WFI.2003-07-31T08:12:33.930.fits | WFI.2003-09-29T01:59:27.948.fits |
| WFI.2003-07-31T08:25:39.396.fits | WFI.2003-09-29T02:13:26.083.fits |
| WFI.2003-07-31T08:38:23.208.fits | WFI.2003-09-30T00:09:11.878.fits |
| WFI.2003-07-31T08:51:03.399.fits | WFI.2003-09-30T00:23:04.564.fits |
| WFI.2003-07-31T09:04:05.265.fits | WFI.2003-09-30T00:37:16.334.fits |
| WFI.2003-08-02T05:58:52.389.fits | WFI.2003-09-30T00:51:16.587.fits |
| WFI.2003-08-02T06:13:08.317.fits | WFI.2003-09-30T01:05:03.368.fits |
| WFI.2003-08-02T06:27:16.303.fits | WFI.2003-10-19T03:18:09.736.fits |
| WFI.2003-08-02T06:40:56.349.fits | WFI.2003-10-19T03:32:01.372.fits |
| WFI.2003-08-02T06:54:29.235.fits | WFI.2003-10-19T03:45:54.888.fits |
| WFI.2003-09-27T01:51:12.972.fits | WFI.2003-10-19T03:59:59.954.fits |
| WFI.2003-09-27T02:05:17.399.fits | WFI.2003-10-19T04:13:43.237.fits |
| WFI.2003-09-27T02:19:16.805.fits | WFI.2003-11-02T00:56:37.499.fits |
| WFI.2003-09-27T02:54:24.422.fits | WFI.2003-11-02T01:10:45.386.fits |
| WFI.2003-09-27T03:08:20.544.fits | WFI.2003-11-02T01:24:54.836.fits |
| WFI.2003-09-29T01:17:26.164.fits | WFI.2003-11-02T01:38:56.427.fits |
| WFI.2003-09-29T01:31:29.071.fits | WFI.2003-11-02T01:53:00.863.fits |
| WFI.2003-09-29T01:45:29.219.fits | |

Bibliography

2MASS TEAM. 2003, vol.p.

Adelman-McCarthy, J. K. f. 2007, ArXiv e-prints, 707

Alcala, J. M., Radovich, M., Silvotti, R., Pannella, M., Arnaboldi, M., Capaccioli, M., Puddu, E., Rifatto, A., De Lucia, G., Mercurio, A., Napolitano, N., Grado, A., Longo, G., Dall’Ora, M., Ripepi, V., Musella, I., & Scaramella, R. 2002, in Presented at the Society of Photo-Optical Instrumentation Engineers (SPIE) Conference, Vol. 4836, Survey and Other Telescope Technologies and Discoveries. Edited by Tyson, J. Anthony; Wolff, Sidney. Proceedings of the SPIE, Volume 4836, pp. 406-417 (2002)., ed. J. A. Tyson & S. Wolff, 406–417

Arsenault, R., & Roy, J.-R. 1986, AJ, 92, 567

Barker, M. K., Sarajedini, A., Geisler, D., Harding, P., & Schommer, R. 2007a, AJ, 133, 1125

—. 2007b, AJ, 133, 1138

Bastian, N., Hempel, M., Kissler-Patig, M., Homeier, N. L., & Trancho, G. 2005, A&A, 435, 65

Belokurov, V., Evans, N. W., Irwin, M. J., Lynden-Bell, D., Yanny, B., Vidrih, S., Gilmore, G., Seabroke, G., Zucker, D. B., Wilkinson, M. I., Hewett, P. C., Bramich, D. M., Fellhauer, M., Newberg, H. J., Wyse, R. F. G., Beers, T. C., Bell, E. F., Barentine, J. C., Brinkmann, J., Cole, N., Pan, K., & York, D. G. 2007a, ApJ, 658, 337

Belokurov, V., Zucker, D. B., Evans, N. W., Gilmore, G., Vidrih, S., Bramich, D. M., Newberg, H. J., Wyse, R. F. G., Irwin, M. J., Fellhauer, M., Hewett, P. C., Walton, N. A., Wilkinson, M. I., Cole, N., Yanny, B., Rockosi, C. M.,

- Beers, T. C., Bell, E. F., Brinkmann, J., Ivezić, Ž., & Lupton, R. 2006a, *ApJ*, 642, L137
- Belokurov, V., Zucker, D. B., Evans, N. W., Kleyna, J. T., Koposov, S., Hodgkin, S. T., Irwin, M. J., Gilmore, G., Wilkinson, M. I., Fellhauer, M., Bramich, D. M., Hewett, P. C., Vidrih, S., De Jong, J. T. A., Smith, J. A., Rix, H.-W., Bell, E. F., Wyse, R. F. G., Newberg, H. J., Mayeur, P. A., Yanny, B., Rockosi, C. M., Gnedin, O. Y., Schneider, D. P., Beers, T. C., Barentine, J. C., Brewington, H., Brinkmann, J., Harvanek, M., Kleinman, S. J., Krzesinski, J., Long, D., Nitta, A., & Snedden, S. A. 2007b, *ApJ*, 654, 897
- Belokurov, V., Zucker, D. B., Evans, N. W., Wilkinson, M. I., Irwin, M. J., Hodgkin, S., Bramich, D. M., Irwin, J. M., Gilmore, G., Willman, B., Vidrih, S., Newberg, H. J., Wyse, R. F. G., Fellhauer, M., Hewett, P. C., Cole, N., Bell, E. F., Beers, T. C., Rockosi, C. M., Yanny, B., Grebel, E. K., Schneider, D. P., Lupton, R., Barentine, J. C., Brewington, H., Brinkmann, J., Harvanek, M., Kleinman, S. J., Krzesinski, J., Long, D., Nitta, A., Smith, J. A., & Snedden, S. A. 2006b, *ApJ*, 647, L111
- Bernstein, R. A., Freedman, W. L., & Madore, B. F. 2002, *ApJ*, 571, 56
- Bertin, E. 2002
- Binney, J. 1992, *ARA&A*, 30, 51
- Blair, W. P., & Long, K. S. 1997, *ApJS*, 108, 261
- Bland-Hawthorn, J., Vlajić, M., Freeman, K. C., & Draine, B. T. 2005, *ApJ*, 629, 239
- Blitz, L., Spergel, D. N., Teuben, P. J., Hartmann, D., & Burton, W. B. 1999, *ApJ*, 514, 818
- Block, D. L., Bournaud, F., Combes, F., Puerari, I., & Buta, R. 2002, *A&A*, 394, L35
- Block, D. L., Freeman, K. C., Jarrett, T. H., Puerari, I., Worthey, G., Combes, F., & Gross, R. 2004, *A&A*, 425, L37
- Bosma, A. 1981, *AJ*, 86, 1791
- Bournaud, F., Jog, C. J., & Combes, F. 2007, *A&A*, 476, 1179
- Bruzual A., G., & Kron, R. G. 1980, *ApJ*, 241, 25

- Bullock, J. S., & Johnston, K. V. 2005, *ApJ*, 635, 931
- Bullock, J. S., Kravtsov, A. V., & Weinberg, D. H. 2000, *ApJ*, 539, 517
- Burggraf, B., Weis, K., & Bomans, D. J. 2005, in *American Institute of Physics Conference Series*, Vol. 783, *The Evolution of Starbursts*, ed. S. Hüttmeister, E. Manthey, D. Bomans, & K. Weis, 33–36
- Carignan, C. 1985, *ApJS*, 58, 107
- Carignan, C., & Puche, D. 1990, *AJ*, 100, 394
- Carlberg, R. G., & Couchman, H. M. P. 1989, *ApJ*, 340, 47
- Carlberg, R. G., Yee, H. K. C., Ellingson, E., Morris, S. L., Abraham, R., Gravel, P., Pritchett, C. J., Smecker-Hane, T., Hartwick, F. D. A., Hesser, J. E., Hutchings, J. B., & Oke, J. B. 1997, *ApJ*, 485, L13+
- Casertano, S., Sackett, P. D., & Briggs, F. H., eds. 1991, *Warped Disks and Inclined Rings around Galaxies*
- Choi, J.-H., Weinberg, M. D., & Katz, N. 2007, *MNRAS*, 381, 987
- Chun, M.-S. 1983, *Journal of Korean Astronomical Society*, 16, 1
- Cimatti, A., Pozzetti, L., Mignoli, M., Daddi, E., Menci, N., Poli, F., Fontana, A., Renzini, A., Zamorani, G., Broadhurst, T., Cristiani, S., D’Odorico, S., Giallongo, E., & Gilmozzi, R. 2002, *A&A*, 391, L1
- Cioni, M. . L., Irwin, M., Ferguson, A. M. N., McConnachie, A., Conn, B. C., Huxor, A., Ibata, R., Lewis, G., & Tanvir, N. 2007, *ArXiv e-prints*, 709
- Dave, R. 1991, *Pattern Recognition Letters*, 12, 657
- de Jong, R. S., Radburn-Smith, D. J., & Sick, J. N. 2007a, *ArXiv e-prints*, 710
- de Jong, R. S., Seth, A. C., Bell, E. F., Brown, T. M., Bullock, J. S., Courteau, S., Dalcanton, J. J., Ferguson, H. C., Goudfrooij, P., Holfeltz, S., Purcell, C., Radburn-Smith, D., & Zucker, D. 2007b, in *IAU Symposium*, Vol. 241, *IAU Symposium*, 503–504
- de Vaucouleurs, G., & Capaccioli, M. 1979, *ApJS*, 40, 699
- de Vaucouleurs, G., de Vaucouleurs, A., Corwin, Jr., H. G., Buta, R. J., Paturel, G., & Fouque, P. 1991, *S&T*, 82, 621

- Debattista, V. P., Mayer, L., Carollo, C. M., Moore, B., Wadsley, J., & Quinn, T. 2006, *ApJ*, 645, 209
- Dekel, A., & Silk, J. 1986, *ApJ*, 303, 39
- Devillard, N. 2001, in *Astronomical Society of the Pacific Conference Series*, Vol. 238, *Astronomical Data Analysis Software and Systems X*, ed. F. R. Harnden, Jr., F. A. Primini, & H. E. Payne, 525–+
- Díaz, R. J., Dottori, H., Aguero, M. P., Mediavilla, E., Rodrigues, I., & Mast, D. 2006, *ApJ*, 652, 1122
- Dicaire, I., Carignan, C., Amram, P., Marcelin, M., Hlavacek-Larrondo, J., de Denus-Baillargeon, M. ., Daigle, O., & Hernandez, O. 2008, *ArXiv e-prints*, 802
- Dunn, J. 1973, *Journal of Cybernetics*, 3, 32
- Efstathiou, G., & Rees, M. J. 1988, *MNRAS*, 230, 5P
- Ellis, S., & Bland-Hawthorn, J. 2006, *Anglo-Australian Observatory Epping Newsletter*, 110, 16
- Elmegreen, B. G., & Hunter, D. A. 2006, *ApJ*, 636, 712
- Elmegreen, D. M. 1981, *ApJS*, 47, 229
- Elmegreen, D. M., Chromey, F. R., & Warren, A. R. 1998, *AJ*, 116, 2834
- Erben, T., Schirmer, M., Dietrich, J. P., Cordes, O., Haberzettl, L., Hetterscheidt, M., Hildebrandt, H., Schmithuesen, O., Schneider, P., Simon, P., Deul, E., Hook, R. N., Kaiser, N., Radovich, M., Benoist, C., Nonino, M., Olsen, L. F., Prandoni, I., Wichmann, R., Zaggia, S., Bomans, D., Dettmar, R. J., & Miralles, J. M. 2005, *Astronomische Nachrichten*, 326, 432
- Erwin, P., Pohlen, M., & Beckman, J. E. 2008, *AJ*, 135, 20
- Fardal, M. A., Guhathakurta, P., Babul, A., & McConnachie, A. W. 2007, *MNRAS*, 380, 15
- Feldmann, R., Mayer, L., & Carollo, C. M. 2008, *ArXiv e-prints*, 801
- Ferguson, A., Irwin, M., Chapman, S., Ibata, R., Lewis, G., & Tanvir, N. 2007, *Resolving the Stellar Outskirts of M31 and M33 (Island Universes - Structure and Evolution of Disk Galaxies)*, 239–+

- Ferguson, A. M. N., & Johnson, R. A. 2001, *ApJ*, 559, L13
- Font, A. S., Johnston, K. V., Bullock, J. S., & Robertson, B. E. 2006a, *ApJ*, 646, 886
- Font, A. S., Johnston, K. V., Guhathakurta, P., Majewski, S. R., & Rich, R. M. 2006b, *AJ*, 131, 1436
- Freedman, W. L., Madore, B. F., Hawley, S. L., Horowitz, I. K., Mould, J., Navarrete, M., & Sallmen, S. 1992, *ApJ*, 396, 80
- Gallais, P., Rouan, D., Lacombe, F., Tiphene, D., & Vauglin, I. 1991, *A&A*, 243, 309
- Galleti, S., Bellazzini, M., & Ferraro, F. R. 2004, *A&A*, 423, 925
- Gieren, W., Pietrzyński, G., Walker, A., Bresolin, F., Minniti, D., Kudritzki, R.-P., Udalski, A., Soszyński, I., Fouqué, P., Storm, J., & Bono, G. 2004, *AJ*, 128, 1167
- Gil de Paz, A., Madore, B. F., Boissier, S., Thilker, D., Bianchi, L., Sánchez Contreras, C., Barlow, T. A., Conrow, T., Forster, K., Friedman, P. G., Martin, D. C., Morrissey, P., Neff, S. G., Rich, R. M., Schiminovich, D., Seibert, M., Small, T., Donas, J., Heckman, T. M., Lee, Y.-W., Milliard, B., Szalay, A. S., Wyder, T. K., & Yi, S. 2007, *ApJ*, 661, 115
- Gilbert, K. M., Fardal, M., Kalirai, J. S., Guhathakurta, P., Geha, M. C., Isler, J., Majewski, S. R., Ostheimer, J. C., Patterson, R. J., Reitzel, D. B., Kirby, E., & Cooper, M. C. 2007, *ApJ*, 668, 245
- Girardi, L., Bertelli, G., Bressan, A., Chiosi, C., Groenewegen, M. A. T., Marigo, P., Salasnich, B., & Weiss, A. 2002, *A&A*, 391, 195
- Gondolo, P. 2004, *ArXiv Astrophysics e-prints*
- Graham, J. A. 1981, *PASP*, 93, 29
- Harris, J., Calzetti, D., Gallagher, III, J. S., Conselice, C. J., & Smith, D. A. 2001, *AJ*, 122, 3046
- Hess, R. 1924, *Astronomische Nachrichten*, 220, 65
- Hildebrandt, H., Erben, T., Dietrich, J. P., Cordes, O., Haberzettl, L., Hetterscheidt, M., Schirmer, M., Schmithuesen, O., Schneider, P., Simon, P., & Trachternach, C. 2006, *A&A*, 452, 1121

- Hunter, C., & Toomre, A. 1969, *ApJ*, 155, 747
- Ibata, R., Irwin, M., Lewis, G., Ferguson, A. M. N., & Tanvir, N. 2001, *Nature*, 412, 49
- Ibata, R., Martin, N. F., Irwin, M., Chapman, S., Ferguson, A. M. N., Lewis, G. F., & McConnachie, A. W. 2007, *ApJ*, 671, 1591
- Ibata, R. A., Gilmore, G., & Irwin, M. J. 1995, *MNRAS*, 277, 781
- Ivanov, G. R., & Kunchev, P. Z. 1985, *Ap&SS*, 116, 341
- Karachentsev, I. D., Grebel, E. K., Sharina, M. E., Dolphin, A. E., Geisler, D., Guhathakurta, P., Hodge, P. W., Karachentseva, V. E., Sarajedini, A., & Seitzer, P. 2003, *A&A*, 404, 93
- Katz, N., & Rix, H.-W. 1992, *ApJ*, 389, L55
- Kennicutt, Jr., R. C. 1989, *ApJ*, 344, 685
- Kim, S. C., Sung, H., Park, H. S., & Sung, E.-C. 2004, *Chinese Journal of Astronomy and Astrophysics*, 4, 299
- Klypin, A., Kravtsov, A. V., Valenzuela, O., & Prada, F. 1999, *ApJ*, 522, 82
- Koch, A., Odenkirchen, M., Grebel, E. K., & Caldwell, J. A. R. 2004, *Astronomische Nachrichten*, 325, 299
- Koribalski, B. S., Staveley-Smith, L., Kilborn, V. A., Ryder, S. D., Kraan-Korteweg, R. C., Ryan-Weber, E. V., Ekers, R. D., Jerjen, H., Henning, P. A., Putman, M. E., Zwaan, M. A., de Blok, W. J. G., Calabretta, M. R., Disney, M. J., Minchin, R. F., Bhathal, R., Boyce, P. J., Drinkwater, M. J., Freeman, K. C., Gibson, B. K., Green, A. J., Haynes, R. F., Juraszek, S., Kesteven, M. J., Knezek, P. M., Mader, S., Marquarding, M., Meyer, M., Mould, J. R., Oosterloo, T., O'Brien, J., Price, R. M., Sadler, E. M., Schröder, A., Stewart, I. M., Stootman, F., Waugh, M., Warren, B. E., Webster, R. L., & Wright, A. E. 2004, *AJ*, 128, 16
- Kormendy, J., & Kennicutt, Jr., R. C. 2004, *ARA&A*, 42, 603
- Landolt, A. U. 1992, *AJ*, 104, 340
- Lauberts, A., & Valentijn, E. A. 1989, *The surface photometry catalogue of the ESO-Uppsala galaxies (Garching: European Southern Observatory, —c1989)*

- Mackey, A. D., Huxor, A., Ferguson, A. M. N., Tanvir, N. R., Irwin, M., Ibata, R., Bridges, T., Johnson, R. A., & Lewis, G. 2007, *ApJ*, 655, L85
- MacQueen, J. B. 1967, in *Proceedings of 5-th Berkeley Symposium on Mathematical Statistics and Probability*, Berkeley, Vol. 1, *Proceedings of 5-th Berkeley Symposium on Mathematical Statistics and Probability*, Berkeley, 281–297
- Malin, D., & Hadley, B. 1997, *Publications of the Astronomical Society of Australia*, 14, 52
- Manfroid, J., & Selman, F. 2001, *The Messenger*, 104, 16
- Massey, P., Olsen, K. A. G., Hodge, P. W., Strong, S. B., Jacoby, G. H., Schlingman, W., & Smith, R. C. 2006, *AJ*, 131, 2478
- Mast, D., Díaz, R. J., & Agüero, M. P. 2006, *AJ*, 131, 1394
- Mateo, M. L. 1998, *ARA&A*, 36, 435
- McConnachie, A. W., Chapman, S. C., Ibata, R. A., Ferguson, A. M. N., Irwin, M. J., Lewis, G. F., Tanvir, N. R., & Martin, N. 2006, *ApJ*, 647, L25
- McConnachie, A. W., Irwin, M. J., Ferguson, A. M. N., Ibata, R. A., Lewis, G. F., & Tanvir, N. 2004, *MNRAS*, 350, 243
- Moore, B., Ghigna, S., Governato, F., Lake, G., Quinn, T., Stadel, J., & Tozzi, P. 1999, *ApJ*, 524, L19
- Natarajan, P., Kneib, J.-P., Smail, I., & Ellis, R. S. 1998, *ApJ*, 499, 600
- Neto, A. F., Gao, L., Bett, P., Cole, S., Navarro, J. F., Frenk, C. S., White, S. D. M., Springel, V., & Jenkins, A. 2007, *MNRAS*, 381, 1450
- New, K. C. B., Tohline, J. E., Frank, J., & Vaeth, H. M. 1998, *ApJ*, 503, 632
- Newberg, H. J., Yanny, B., Cole, N., & Beers, T. 2006, in *Bulletin of the American Astronomical Society*, Vol. 38, *Bulletin of the American Astronomical Society*, 1148–+
- Peacock, J. A., & Heavens, A. F. 1990, *MNRAS*, 243, 133
- Petitpas, G. R., & Wilson, C. D. 1998, *ApJ*, 503, 219
- Pietrzyński, G., Gieren, W., & Udalski, A. 2002, *PASP*, 114, 298
- Pietrzyński, G., & Gieren, W. 2006, *Memorie della Societa Astronomica Italiana*, 77, 239

- Pietrzyński, G., Ulaczyk, K., Gieren, W., Bresolin, F., & Kudritzki, R. P. 2005, *A&A*, 440, 783
- Pohlen, M., Dettmar, R.-J., Lütticke, R., & Aronica, G. 2002, *A&A*, 392, 807
- Pohlen, M., & Trujillo, I. 2006, *A&A*, 454, 759
- Pozzetti, L., Bruzual A., G., & Zamorani, G. 1996, *MNRAS*, 281, 953
- Press, W. H., & Schechter, P. 1974, *ApJ*, 187, 425
- Pritchett, C. J., & van den Bergh, S. 1994, *AJ*, 107, 1730
- Pryor, C., & Kormendy, J. 1990, *AJ*, 100, 127
- Puche, D., & Carignan, C. 1991, *ApJ*, 378, 487
- Puche, D., Carignan, C., & Bosma, A. 1990, *AJ*, 100, 1468
- . 1995, *Astronomy Data Image Library*, 4
- Radovich, M. 2002a
- . 2002b
- Rees, M. J. 1986, *MNRAS*, 218, 25P
- Robin, A. C., Reylé, C., Derrière, S., & Picaud, S. 2003, *A&A*, 409, 523
- Roškar, R., Debattista, V. P., Stinson, G. S., Quinn, T. R., Kaufmann, T., & Wadsley, J. 2008, *ApJ*, 675, L65
- Rubin, V. C., Thonnard, N., & Ford, Jr., W. K. 1980, *ApJ*, 238, 471
- Sakamoto, K., Matsushita, S., Peck, A. B., Wiedner, M. C., & Iono, D. 2004, *ApJ*, 616, L59
- Sarajedini, A., Barker, M. K., Geisler, D., Harding, P., & Schommer, R. 2006, *AJ*, 132, 1361
- Schirmer, M., Erben, T., Schneider, P., Pietrzynski, G., Gieren, W., Carpano, S., Micol, A., & Pierfederici, F. 2003, *A&A*, 407, 869
- Schlegel, D. J., Finkbeiner, D. P., & Davis, M. 1998, *ApJ*, 500, 525

- Shang, Z., Brinks, E., Zheng, Z., Chen, J., Burstein, D., Su, H., Byun, Y.-I., Deng, L., Deng, Z., Fan, X., Jiang, Z., Li, Y., Lin, W., Ma, F., Sun, W.-H., Wills, B., Windhorst, R. A., Wu, H., Xia, X., Xu, W., Xue, S., Yan, H., Zhou, X., Zhu, J., & Zou, Z. 1998, *ApJ*, 504, L23+
- Smith, J. A., Tucker, D. L., Kent, S., Richmond, M. W., Fukugita, M., Ichikawa, T., Ichikawa, S.-i., Jorgensen, A. M., Uomoto, A., Gunn, J. E., Hamabe, M., Watanabe, M., Tolea, A., Henden, A., Annis, J., Pier, J. R., McKay, T. A., Brinkmann, J., Chen, B., Holtzman, J., Shimasaku, K., & York, D. G. 2002, *AJ*, 123, 2121
- Sparke, L. S., & Casertano, S. 1988, *MNRAS*, 234, 873
- Springel, V. 2005, *MNRAS*, 364, 1105
- Springel, V., White, S. D. M., Jenkins, A., Frenk, C. S., Yoshida, N., Gao, L., Navarro, J., Thacker, R., Croton, D., Helly, J., Peacock, J. A., Cole, S., Thomas, P., Couchman, H., Evrard, A., Colberg, J., & Pearce, F. 2005, *Nature*, 435, 629
- Stetson, P. B. 1987, *PASP*, 99, 191
- Stoughton, C. 2002, *AJ*, 123, 3487
- Talbot, Jr., R. J., Jensen, E. B., & Dufour, R. J. 1979, *ApJ*, 229, 91
- Thilker, D. A., Bianchi, L., Boissier, S., Gil de Paz, A., Madore, B. F., Martin, D. C., Meurer, G. R., Neff, S. G., Rich, R. M., Schiminovich, D., Seibert, M., Wyder, T. K., Barlow, T. A., Byun, Y.-I., Donas, J., Forster, K., Friedman, P. G., Heckman, T. M., Jelinsky, P. N., Lee, Y.-W., Malina, R. F., Milliard, B., Morrissey, P., Siegmund, O. H. W., Small, T., Szalay, A. S., & Welsh, B. Y. 2005, *ApJ*, 619, L79
- Thim, F., Tammann, G. A., Saha, A., Dolphin, A., Sandage, A., Tolstoy, E., & Labhardt, L. 2003, *ApJ*, 590, 256
- Tikhonov, N. A., Galazutdinova, O. A., & Drozdovsky, I. O. . 2005, *A&A*, 431, 127
- Tissera, P. B., Smith Castelli, A. V., & Scannapieco, C. 2006, *A&A*, 455, 135
- Toomre, A. 1983, in *IAU Symposium, Vol. 100, Internal Kinematics and Dynamics of Galaxies*, ed. E. Athanassoula, 177–185
- Toth, G., & Ostriker, J. P. 1992, *ApJ*, 389, 5

- Tully, R. B. 1988, *Nearby galaxies catalog* (Cambridge and New York, Cambridge University Press, 1988, 221 p.)
- van den Bosch, F. C. 2001, *MNRAS*, 327, 1334
- van der Kruit, P. C. 1987, *A&A*, 173, 59
- Wakker, B. P., & van Woerden, H. 1991, *A&A*, 250, 509
- Wehner, E. H., & Gallagher, III, J. S. 2005, *ApJ*, 618, L21
- Whitaker, K. E., & van Dokkum, P. G. 2008, *ApJ*, 676, L105
- White, S. D. M. 1978, *MNRAS*, 184, 185
- . 1979, *MNRAS*, 189, 831
- Yanny, B., Newberg, H. J., Grebel, E. K., Kent, S., Odenkirchen, M., Rockosi, C. M., Schlegel, D., Subbarao, M., Brinkmann, J., Fukugita, M., Ivezić, Ž., Lamb, D. Q., Schneider, D. P., & York, D. G. 2003, *ApJ*, 588, 824
- Zickgraf, F.-J., Humphreys, R. M., Graham, J. A., & Phillips, A. 1990, *PASP*, 102, 920
- Zucker, D. B., Belokurov, V., Evans, N. W., Kleyna, J. T., Irwin, M. J., Wilkinson, M. I., Fellhauer, M., Bramich, D. M., Gilmore, G., Newberg, H. J., Yanny, B., Smith, J. A., Hewett, P. C., Bell, E. F., Rix, H.-W., Gnedin, O. Y., Vidrih, S., Wyse, R. F. G., Willman, B., Grebel, E. K., Schneider, D. P., Beers, T. C., Kniazev, A. Y., Barentine, J. C., Brewington, H., Brinkmann, J., Harvanek, M., Kleinman, S. J., Krzesinski, J., Long, D., Nitta, A., & Snedden, S. A. 2006, *ApJ*, 650, L41

List of Tables

| | | |
|-----|--|----|
| 2.1 | NGC 300 parameters as derived from different studies | 15 |
| 2.2 | M 83 parameters as derived from different studies | 16 |
| 2.3 | M 33 parameters as derived from different studies | 16 |
| 2.4 | NGC 7793 parameters as derived from different studies | 17 |
| 3.1 | Important parameters of the NGC 300 data | 21 |
| 3.2 | Important parameters of the M 83 data | 22 |
| 3.3 | Important parameters of the NGC 7793 data | 22 |
| 3.4 | Important parameters of the M 33 data | 23 |
| 4.1 | Important photometry parameters as used by IRAF/DAOPHOT for NGC 300 | 42 |
| 4.2 | Standard deviation of the global solution applied to each chip . . . | 44 |
| 4.3 | Important photometry parameters for the M 83 data as used by IRAF/DAOPHOT | 45 |
| 4.4 | Results of the M 83 transformation to the Standard | 46 |
| 4.5 | Important photometry parameters for the NGC 7793 data as used by IRAF/DAOPHOT | 46 |
| 4.6 | Calibration results for each night in the B-band (B123) of the NGC 7993 data | 48 |
| 4.7 | Calibration results for each night in the B-band of the NGC 7993 data | 48 |
| 4.8 | Calibration results for each night in the V-band of the NGC 7993 data | 48 |
| 5.1 | Randomly generated positions of the artificial clusters in the test data. | 66 |
| 5.2 | Clusters recovered after 2 fuzzy c-mean runs | 67 |

| | | |
|-----|--|-----|
| 6.1 | Fitting results of the stellar count surface-density plots | 75 |
| 6.2 | Cluster properties in the M 33 dataset | 94 |
| 6.3 | Cluster properties in the NGC 7793 dataset | 108 |
| 7.1 | Summary of substructures found | 120 |

List of Figures

| | | |
|-----|---|----|
| 2.1 | Overview of substructure found in M 31 | 9 |
| 3.1 | V-band image of NGC 300 reduced by Mischa Schirmer | 20 |
| 3.2 | Outline of the reduction | 25 |
| 3.3 | Fringing correction example | 27 |
| 3.4 | Bad astrometry Image of M 83 | 29 |
| 3.5 | Sky subtracted image of M 83 | 30 |
| 3.6 | Example of a final co-added image of M 83 in the V-band. The maximum variation in the sky-background value outside the galaxy is of the order of 0.05 % | 32 |
| 3.7 | Example of a final co-added image of NGC 7793 in the V-band. The maximum variation in the sky-background value outside the galaxy is of the order of 0.06 % | 33 |
| 4.1 | Illumination of the ESO/MPG WFI | 40 |
| 4.2 | Residuals of the standard stars | 43 |
| 5.1 | Example of isochrones | 50 |
| 5.2 | Example of starcount maps | 54 |
| 5.3 | Example of a <i>KNIME</i> workflow | 64 |
| 5.4 | Example of a clustering run | 65 |
| 5.5 | Example of two fuzzy c-means clustering runs | 65 |
| 6.1 | Hess Diagram of stars in the NGC 300 Field | 71 |
| 6.2 | Color magnitude diagram of stars in the NGC 300 Field | 71 |
| 6.3 | A star count map of objects brighter than 20 mag and having $0.2 < B - V < 1.2$ | 72 |
| 6.4 | Star count distribution maps for the RGB stars of NGC 300 | 74 |
| 6.5 | Star count distribution maps for the RGB stars of NGC 300 | 75 |

| | | |
|------|---|-----|
| 6.6 | Star count surface number densities and best fitting exponential profile. | 76 |
| 6.7 | Star count distribution maps for the MS stars of NGC 300 using different binning parameters | 79 |
| 6.8 | Star count distribution maps for the MS stars of NGC 300 using different binning parameters | 80 |
| 6.9 | Replot of the data published by Carignan (1985) | 81 |
| 6.10 | Example results of the fuzzy c-means clustering for NGC 300. . . | 81 |
| 6.11 | Example results of the fuzzy c-means clustering for NGC 300. . . | 82 |
| 6.12 | Color magnitude diagrams of M 83 | 85 |
| 6.13 | Star count map of M 83 for the blue part of the CMD | 86 |
| 6.14 | Star count map of M 83 for the red part of the CMD | 87 |
| 6.15 | Example results of the fuzzy c-means clustering. All clusters outside the central part have only 8 members or less. | 88 |
| 6.16 | Color magnitude diagrams of M 33 | 96 |
| 6.17 | Color magnitude diagrams of M 33 North and South Field | 97 |
| 6.18 | Star count maps of old populations in M 33 | 98 |
| 6.19 | Star count maps for younger populations in M 33 | 99 |
| 6.20 | Star count maps for the North of M 33 | 100 |
| 6.21 | Star count maps for the South of M 33 | 101 |
| 6.22 | A cluster analysis done to search for the most prominent features . | 102 |
| 6.23 | Two example clustering runs with 59 clusters for M 33 | 102 |
| 6.24 | Another example of two clustering runs with 59 clusters for M 33 . | 103 |
| 6.25 | Color magnitude diagram for NGC 7793 | 105 |
| 6.26 | Star count maps for the blue stars in NGC 7793 | 110 |
| 6.27 | Star count maps for the blue stars in NGC 7793 | 111 |
| 6.28 | Star count maps for red stars in NGC 7793 | 112 |
| 6.29 | Star count maps for red stars in NGC 7793 | 113 |
| 6.30 | Examples of two maps from the fuzzy c-means clustering runs of the NGC 7793 | 114 |
| 6.31 | Other examples of two maps from the fuzzy c-means clustering runs of the NGC 7793 | 114 |

Acknowledgments

Finally, I want to thank the people who have made this thesis possible. Such a work cannot be done without the support of others because nobody can know every single aspect that arises during such work.

First of all I like to thank my supervisors Prof. Dr. Ralf-Jürgen Dettmar and Priv. Doz. Dr. Dominik Bomans for supporting the thesis and for discussing it. I also thank Prof. Dr. P. Schneider for giving me the opportunity to work in the *THELI*-team. From this team I learned how to reduce wide field mosaic data and how to use *THELI* to do this. From the team members I especially want to express my gratitude to Dr. Thomas Erben and Dr. Mischa Schirmer who helped me understanding how the pipeline works and suggested what to do in case of some severe problems. I also thank Mischa Schirmer for allowing me to use his reduced data of NGC 300 which was the first data set I used in my thesis. Speaking of the data I also like to thank Birgitta Burggraf who allowed me to use her photometric data of M 33, answering my questions about this galaxy and for being my friendly office-mate. For discussing the wide field illumination problem and some topics of radio astronomy I want to express my gratitude to Dr. Clemens Trachternach. I also like to thank Dr. Giuseppe Aronica and Dr. Ralf Kissmann for proof-reading this thesis.

In addition to these people I also want to express my gratitude to all other colleagues at the “Astronomisches Institut der Ruhr-Universität Bochum” who made my work there very enjoyable. In particular I want to name Tim Falkenbach and Ingo Tertel who were my colleagues in administrating and running the computer network of our institute.

Curriculum vitae

| | | |
|--------------------------------------|---------------------|--|
| PERSÖNLICHE INFORMATIONEN | Name | Olaf Schmithüsen |
| | Geburtsdatum | 18.10.1976 |
| | Geburtsort | Oberhausen-Osterfeld |
| | Familienstand | ledig |
| | Staatsangehörigkeit | Deutsch |
| | Wohnort | Teutoburger Str. 248 46119 Oberhausen |
| SCHULISCHE LAUFBAHN | 1983 - 1987 | Jacobischule (Oberhausen) |
| | 1987 - 1996 | Josef-Albers-Gymnasium (Bottrop) |
| | 1996 - 1997 | Rheinische Friedrich-Wilhelms- Universität (Bonn) |
| | 1997 - 2008 | Ruhr-Universität Bochum |
| ABSCHLÜSSE | 1996 | allgemeine Hochschulreife |
| | 2003 | Physik-Diplom Diplomarbeitstitel: Sternentstehungs- geschichte von Zwerggalaxien mit HST (Hubble Space Telescope) Photometrie |